# ABSTRACT

BARLETTA, PHILIP. Study of GaN-based Materials for Light-emitting Applications. (Under the direction of Dr. S.M. Bedair and Dr. N.A. El-Masry).

The purpose of this study was to explore the possibility of fabricating phosphor-free white-emitting LED's based in the gallium nitride material system. The structures were to be grown using metal-organic chemical vapor deposition (MOCVD). Toward this end, a Thomas Swan Scientific close-coupled showerhead reactor was installed.

The first experimental step in this project was the optimization of nominally undoped GaN. This was achieved successfully, as smooth, non-compensated, optically-active films were demonstrated. Additionally, a full on- and off-axis x-ray diffraction study showed that the crystal quality of this material compared favorably to that of published standards.

Successful n- and p-type doping of GaN were also demonstrated. Device-worthy mobility and carrier concentration values were demonstrated. Atomic force microscopy of n-type material verified that the films was sufficiently smooth as to serve as a layer upon which active-layer quantum wells could be grown. Photoluminescence of both n- and p-type material was examined as well.

An extensive indium gallium nitride growth study was carried out. The effects of several growth parameters on emission characteristics were presented. PL emission wavelengths as high as 561 nm were demonstrated. The issues of uniformity and indium platelet formation were also addressed.

This InGaN experimental work was complemented with a series of calculations which gave the expected emission wavelength of an InGaN/GaN quantum well structure based on In content and well width. Strain, the quantum size effect, and the quantum-confined Stark effect were all factored into these calculations in order to study their individual contributions to emission wavelength values.

This work concluded with an examination of white device structure and fabrication. Both two- and three-color devices were considered. Monochromtic devices emitting in the green and yellow were fabricated. The yellow device, emitting at 575nm, yielded the longest reported wavelengths for Al-free InGaN/GaN multiple quantum-well LED's grown by MOCVD. Finally, white emission was demonstrated from a two-color MQW structure emitting blue and yellow light.

The research presented herein demonstrates the first step toward achieving phosphor-free solid-state white lighting. Continuation of this study will hopefully lead to future commercial, industrial, and residential applications of this technology.

# STUDY OF GaN-BASED MATERIALS FOR LIGHT-EMITTING APPLICATIONS

by
**PHILIP BARLETTA**

A dissertation submitted to the Graduate Faculty of
North Carolina State University
in partial fulfillment of the
requirements for the Degree of
Doctor of Philosophy

**MATERIALS SCIENCE AND ENGINEERING**

Raleigh

2006

**APPROVED BY:**

| __________________________ | __________________________ |
| --- | --- |
| Jerome J. Cuomo | Carl C. Koch |
| __________________________ | __________________________ |
| Salah M. Bedair<br>Co-chair of Advisory Committee | Nadia A. El-Masry<br>Co-chair of Advisory Committee |

## BIOGRAPHY

Philip Barletta was born on August 5, 1974 in Scranton, PA. In 1992 he began studying materials science at Wilkes University in Wilkes-Barre, PA. In May of 1996 he graduated Magna cum Laude from Wilkes, receiving a Bachelor of Science degree in materials engineering.

Later that year Philip moved to Raleigh, NC, and began his studies at North Carolina State University. He performed research at the Center for Advanced Manufacturing Processes and Materials (CAMP-M) under the direction of Dr. Jerome J. Cuomo. In December of 1999 he received his Master of Science degree in materials science and engineering at N.C. State.

After a brief stint as a process engineer at Litespec Optical Fiber, Philip returned to North Carolina State in the fall of 2000 to pursue his Ph.D. He was awarded a research assistantship to work under Dr. Salah Bedair studying the MOCVD growth of compound semiconductors.

On June 9, 2001, Philip married his long-time sweetheart, Kristin Thoney, at Holy Trinity Lutheran Church in Raleigh, NC. Five years and one day later, Kristin gave birth to their first child, John Philip “Jack” Barletta.

In November 2005, while still completing his studies, Philip accepted a job at Dot Metrics Technologies, a start-up company in Charlotte, NC. In the summer of 2006, he earned his Ph.D. degree in materials science and engineering at N.C. State. On July 31 of that year, he began working for the Center for Thermoelectrics Research at RTI International in Research Triangle Park, NC.

## ACKNOWLEDGEMENTS

Any time one undertakes a work of this magnitude, he (or she) cannot do it alone. I'm no exception. I am indebted to a great number of individuals who have helped me along the way, and I will now do my best to express my gratitude

I would like to start by thanking my advisor, Dr. Salah Bedair. Dr. Bedair's extensive knowledge, as well as his love of science, make him a truly exceptional mentor. My experiences with him will certainly guide me as I continue along in my career. I share the same sentiments for my co-advisor, Dr. Nadia El-Masry. She has played a huge role in my graduate studies as well, and I owe her a tremendous debt of gratitude.

I would also like to thank the rest of my committee: Dr. Jerry Cuomo and Dr. Carl Koch. I am especially indebted to Dr. Cuomo, as he was my M.S. advisor and helped shape me into the scientist I am today. Dr. Koch has looked at my work from the point of view of a metallurgist, and thus has provided some unique insights.

Thanks are also due to Dr. Steven LeBoeuf and Dr. Michael Aumer, two old friends of mine who introduced me to Dr. Bedair and helped bring me into his laboratory. They were also instrumental in teaching me the basics of both MOCVD and the gallium nitride material system.

Throughout the bulk of my Ph.D. studies, I have worked side-by-side with Baxter Moody. Baxter and I spent many long hours in the lab together, and his contributions to my work are far too numerous to mention. As of late, however, my main sidekicks have been Ahmed Emara and Acar Berkman. They both have been invaluable in the past year, and they're very well-suited to take over my research as I move on into "the real world".

I wish them both all the best in the lab, and I wish Acar's Galtasaray soccer club all the best on the pitch. (Except, of course, if they come across my Bolton Wanderers in European competition.)

Speaking of Europeans, I would like to extend my gratitude to Trevor Grantham and Matt Benham of Thomas Swan Scientific for assisting in the installation of my MOCVD equipment. Dr. Ken Hess, Thomas Swan's stateside contact, has also been a great resource. Dr. Maarten Leys of IMEC has gone out of his way to assist me on several occasions. My co-workers at Dot Metrics Technologies, Dr. Ed Stokes and Dr. Jennifer Pagan, deserve a round of applause as well. And this acknowledgments section would be sorely incomplete without a mention of Dr. Andy "The Face" Oberhofer.

The list of co-workers, both past and present, who've helped me along is extensive. To Dr. Mason Reed, Erdem Arkun, Oliver Luen, Dr. Meredith Reed, Dr. John Roberts, Hong "You Can Call Me Al" Yin, Joey Luther, Maria Ritums, and Dr. Chris Parker: Thank you. You've all helped me down this path and I truly appreciate all that each of you has done.

The next individual I need to acknowledge is the man working tirelessly across the hall in Dr. Davis's lab: Seann Bishop. Late nights, early mornings, holiday weekends …I always knew you were only a lab away, cursing as loudly at your equipment as I was at mine. By the way, Seann, did you return my Lewis Black CD yet?

Of course, it wasn't only fellow workers that deserve my gratitude. More importantly, I'd like to thank all the friends and family who have supported me during this venture. Foremost among them are my parents—Kathleen and Philip Barletta.

Though they're 600 miles away, I've always felt they were right beside me throughout all my struggles and accomplishments.

However, if I could name one individual to thank above all others, it would be my wife, the lovely and talented Kristin Barletta. Kristin, you've shown more toughness, patience, and resolve (not to mention love) than I thought was humanly possible. You've been tender and caring when I've been down, but always ready to deliver a kick in the pants if I got lazy. In short, you've been nothing less than a perfect companion. There's no way I could have done this without you.

I'd also like to thank my newborn son, Jack. Of course, he wasn't around for most of my graduate school misadventures—but on June 10, 2006, at 10:14 AM, he arrived with a bang and made me the happiest man on the planet. Little man, I'll always be here for you. Anytime, anywhere—my eyes, ears, and heart will always be open.

And finally, I'd like to thank Sam, Daisy, and Reggie for reminding me that, no matter how bad things seem, sometimes a nap and some tuna is all you need to brighten your day.

**TABLE OF CONTENTS**

List of Tables……………………………………………………….………………ix

List of Figures…………………………………………………………………………x

**1.0 General Introduction……………………………………………………………...1**

1.1 A Brief History of Electric Light……………………………………………...1

1.2 The Measurement of Light……………………………………………………2

1.3 Advantages of LED’s…………………………………………………………4

1.4 White Light Using LED’s?..............................................................................7

1.5 Potential of the Gallium Nitride Material System for Solid-State Lighting…10

1.6 References……………………………………………………………………14

**2.0 Metal-Organic Chemical Vapor Deposition……………………………………16**

2.1 Introduction to MOCVD……………………………………………………..16

2.2 Thomas Swan Scientific MOCVD System…………………………………..17

2.3 MOCVD Reactors……………………………………………………………21

*2.3.1 Early reactor design*…………………….……………………21

*2.3.2 Thomas Swan Scientific close-coupled showerhead reactor*…….23

2.4 References…………………………………………………………...….29

**3.0 Fundamentals of Gallium Nitride………………………………………………31**

3.1 Crystallography of Gallium Nitride…………………………………………31

3.2 Growth of Gallium Nitride…………………………………………………..33

*3.2.1 Growth techniques*………………………………………………33

*3.2.2 Substrate issues*…………………………..…………………34

*3.2.3 Pre-growth procedure*…………………………………………35

3.3 Defects and Structure of Epitaxial Gallium Nitride…………………………37

3.4 Polarity in Gallium Nitride…………………………………………………..40

3.5 Preliminary Growth of GaN – Experimental……………………………...42
*3.5.1 Optimized growth conditions for nominally undoped GaN*……...44
*3.5.2 Optical microscopy of nominally undoped GaN*…………………45
*3.5.3 X-ray diffraction of nominally undoped GaN*……………...…..47
*3.5.4 Photoluminescence of nominally undoped GaN*…………………57
*3.5.5 Hall measurement of nominally undoped GaN*…………..………58
3.6 Doping of Gallium Nitride……………………………………………...59
*3.6.1 N-type doping of GaN*……………………………………………59
*3.6.2 P-type doping of GaN – Background*……………………...…..65
*3.6.3 P-type doping of GaN – Experimental*……………………...…67
3.7 References……………………………………………………………73

**4.0 Indium Gallium Nitride………………………………………………….80**
4.1 Structure of Active Layers……………………………………………...80
4.2 Indium Nitride…………………………………………………………..81
4.3 Growth of the Ternary Alloy InGaN…………………………………...83
*4.3.1 Introduction to InGaN*…………………………………………..83
*4.3.2 InGaN growth model*……………………………………………84
4.4 Lattice Mismatch in InGaN……………………………………………87
*4.4.1 Strain in InGaN*…………………………………………………..87
*4.4.2 Composition modulation in InGaN*……………………...….89
4.5 Growth of InGaN – Experimental……………………………………91
*4.5.1 Growth conditions*……………………….………………91
*4.5.2 Dependence of TMI flow and growth temperature*…………...…93
*4.5.3 Capping of InGaN structures* ……………………………………95
*4.5.4 Growth rate of capped InGaN/GaN layers*...………………....…97
*4.5.5 Emission properties of capped InGaN/GaN MQW structures*.…103
*4.5.6 Spectrum achieved through capped InGaN structures*……..…..108
*4.5.7 Uniformity of InGaN/GaN samples*..……………………...…110
*4.5.8 Indium platelet formation in capped InGaN/GaN structures*.….116

4.6 References……………………………………………………………..120

**5.0 Mathematical Calculation of InGaN Emission……..…………………………..124**

5.1 Preliminary Considerations………………………………………….....124

5.2 Bandgap Calculation of Bulk InGaN………………………………………126

5.3 Calculation of the Quantum Size Effect in InGaN/GaN Quantum Wells…128

5.4 Calculation of the Polarization Fields in InGaN/GaN Quantum Wells…....133

5.5 Effect of Polarization Fields on the Bandgap of InGaN/GaN Quantum Wells……………………………………………………………………..136

5.6 Difficulties in the Use of Wide Quantum Wells in InGaN/GaN structures...138

5.7 Application to Experimental Data…………………………………….…142

5.8 References……………………………………………………………..144

**6.0 Fabrication of InGaN-based Devices…………………………………………146**

6.1 LED Structures…………………………………………………………….. 146

*6.1.1 RGB structure*……………………………………………………146

*6.1.2 Complementary wavelength structure*……………………….…..153

6.2 Monochromatic LED Fabrication……………..…………………………...155

*6.2.1 Fabrication overview*……………………………………..……155

*6.2.2 Fabrication of p-n junction*……………………………...……..157

*6.2.3 Fabrication of long-wavelength LED's*…...……………………..160

*6.2.4 Tip region—green devices*……………………………………..160

*6.2.5 Center region—yellow/amber devices*……………………………163

*6.2.6 Photoluminescence of yellow devices*……………………...…..165

*6.2.7 Electrical properties of green and yellow devices*…………..…...169

6.3 Demonstration of White Emission……………………………………….…173

6.4 References……………………………………………………………..179

**7.0 Suggestions for Future Research……………………………..……………..181**

# List of Tables


Table 1.1 Top efficacies of single-color LED's currently in production……………6

Table 3.1 Typical values of mosaic parameters in GaN……………………………38

Table 3.2 Electronegativity values of selected elements…………………………...39

Table 3.3 Run conditions for the growth of high-quality undoped GaN…………...44

Table 3.4 Microstructural parameters of undoped GaN……………….…..………….55

Table 3.5 Electrical measurements of n-type GaN ………………………………..61

Table 3.6 RMS roughness values for n-type GaN…………………………………63

Table 3.5 Electrical measurements of p-type GaN ………………………………..68

Table 4.1 Growth rate and temperature of a series of InGaN/GaN
MQW structures………………………………………………….…………99

Table 4.2 Growth conditions used to achieve the spectra shown in Figure 4.16….110

Table 4.3 Growth conditions used to achieve the spectra shown in Figure 4.20….115

Table 5.1 Material constants for GaN, InN, and InGaN…………………………..125

Table 5.2 Quantized energy levels within a 16% InGaN/GaN QW
structure, as calculated by the Szmulowicz formulation
of the Kronig-Penney model…………………………………………....132

Table 5.3 Estimated In content for the structures shown in Figure 4.16……….....142

Table 6.1 Calculation of relative power necessary to obtain white light
from an RGB mixture……………………………………………………..150

Table 6.2 Complementary wavelengths and corresponding power ratios………...154

Table 6.3 Growth conditions of long-wavelength LED structure (S069-06)……..160

Table 6.4 Electrical properties of fabricated devices……………………………...171

Table 6.5 PL results from white-emitting structures………………………………176

## List of Figures


Figure 1.1 Evolution of LED technology……………………………………………..2

Figure 1.2 Relative sensitivity of the human eye to visible wavelength…………...…3

Figure 1.3 CIE chromaticity diagram (1976)………………………………………8

Figure 1.4 E-k diagram of gallium nitride…………………………………………...10

Figure 1.5 Bandgap vs. lattice constant for the nitride material system…………..…11

Figure 2.1 Diagram of Thomas Swan MOCVD gas delivery circuit………………..18

Figure 2.2 Original GaN reactor design………..……………………………………21

Figure 2.3 Thomas Swan Scientific close-coupled showerhead (TSS-CCS) reactor..23

Figure 2.4 Photo of showerhead……………………………………..…………25

Figure 2.5 TSS-CCS temperature calibration for (a) 300 sccm $N_2$ purge; and (b) 600 sccm $H_2$ purge…..…………………………………………………27

Figure 3.1 Zinc blende structure…………………..……………………………….31

Figure 3.2 Wurtzite structure…………………………………………………...33

Figure 3.3 Columnar model of III-nitrides…………………………….………….37

Figure 3.4 (a) Ga-face gallium nitride; and (b) N-face gallium nitride……………...41

Figure 3.5 Sketch of (a) 14x14mm substrate position in the middle of the susceptor; and (b) 1 in. wedge placed radially across the susceptor….....43

Figure 3.6 Graphical representation of GaN growth process………………………..45

Figure 3.6 Surface of GaN sample grown under (a) non-optimized conditions; (b) optimized conditions……………………………………………...…46

Figure 3.8 Transmission spectra of a GaN film grown for xx minutes……………...47

Figure 3.9 X-ray diffraction scan of undoped GaN: (002) reflection, (b) (004) reflection, and (c) (006) reflection……………………………..…49

Figure 3.10 X-ray diffraction scan of undoped GaN: (004) reflection ……………....50

Figure 3.11 X-ray diffraction scan of undoped GaN: (006) reflection……………….50

Figure 3.12 Williamson-Hall plot of undoped GaN…………………………………..51

Figure 3.13 X-ray diffraction scan of undoped GaN: (103) reflection……..…………52

Figure 3.14 X-ray diffraction scan of undoped GaN: (302) reflection………..……..53

Figure 3.15 Plot of crystal quality characteristics of a series of GaN films……..……56

Figure 3.16 Photoluminescence of optimized undoped GaN……………………....58

Figure 3.17 Silane dilution manifold………………………………………………....60

Figure 3.18 Mobility and carrier concentration vs. silane flow for n-type GaN…..…61

Figure 3.19 Photoluminescence of n-type GaN………………..…………………..62

Figure 3.20 AFM image of n-type GaN surface……………………………..…64

Figure 3.21 PL spectra of annealed and unannealed p-type GaN with $p = 2.22x10^{17}$ $cm^{-3}$…………………………………………………….…70

Figure 3.22 PL spectra of annealed and unannealed p-type GaN with $p = 6.73x10^{17}$ $cm^{-3}$……………………………………………….....…71

Figure 3.23 Simplified band diagram of Mg-doped GaN, showing optical transitions at 387 nm and 428 nm……………………………………..…72

Figure 4.1 InGaN/GaN double heterostructure……………………..……………80

Figure 4.2 Equilibrium vapor pressures of common compound semiconductors…...82

Figure 4.3 Reaction pathways for the deposition of In-based nitride compounds…..85

Figure 4.4 Band-bending in a double heterostructure……………………………..…88

Figure 4.5 Binodal (solid) and spinodal (dashed) curves for the InGaN system……90

Figure 4.6 Emission wavelength vs. In/Ga ratio for samples grown at 875ºC…..…..89

Figure 4.7 Emission wavelength vs. growth temperature for a series of InGaN/GaN quantum wells……………………………………..……..95

Figure 4.8 Simplified diagram of a typical InGaN-based LED structure…………...96

Figure 4.9 ω-2θ x-ray scan of a series of capped 4-well InGaN/GaN structures, measured at the (a) center; and (b) tip ….....................98

Figure 4.10 Growth rate vs. growth temperature for capped InGaN/GaN structures, measured at the center……………………...………………100

Figure 4.11 Growth rate vs. growth temperature for capped InGaN/GaN structures, measured at the tip……………………………….………101

Figure 4.12 TEM images of a capped 4-well MQW structure at (a)160kX magnification; and (b) 200kX magnification…………………………...102

Figure 4.13 Emission wavelength vs.growth temperature for InGaN/GaN quantum well structures capped at 975ºC …….………………………..103

Figure 4.14 FWHM of emission peak vs. growth temperature for InGaN/GaN quantum well structures capped at 975ºC ……………………………...104

Figure 4.15 Emission wavelength vs. quantum well growth time for InGaN/GaN quantum well structures capped at 975ºC…………………………....105

Figure 4.16 Emission wavelength vs. TMG flux for InGaN/GaN quantum well structures capped at 975ºC…………………………....107

Figure 4.17 PL emission spectra obtained by capped InGaN/GaN structures grown using the TSS-CCS……………………………………………………..108

Figure 4.18 Example of non-uniform emission in an InGaN/GaN QW structure…..111

Figure 4.19 (a) Top and (b) side views of reactor's PBN-coated graphite heater...…112

Figure 4.20 Example of improved emission uniformity in an InGaN/GaN structure due to reduced temperature ramp rate……………….………113

Figure 4.21 PL emission spectra obtained by capped InGaN/GaN structures on wedge-shaped substrates…………………………………………115

Figure 4.22 Photos of capped InGaN/GaN QW samples with metallic appearances…………………………………………………………..116

Figure 4.23 Degraded emission characteristics from metallic InGaN/GaN structure……………………………………………………………117

Figure 4.24 XRD of clear and metallic-looking capped InGaN/GaN samples……...118

Figure 5.1 Emission wavelength vs. indium content for relaxed and strained InGaN ....................128

Figure 5.2 Calculation of the Szmulowicz formulation of the Kronig-Penney model for a 16% InGaN/GaN QW structure for (a) the conduction band and (b) the valence band....................131

Figure 5.3 Bandgap shift due to quantum size effect vs. In content for various length quantum wells....................132

Figure 5.4 Electric field [from both spontaneous and piezoelectric polarization] vs. In content....................135

Figure 5.5 Emission wavelength vs. In content for various length quantum wells...138

Figure 5.6 Electron and hole envelope functions for (a) an unstrained quantum well, and (b) a compressively strained quantum well...........140

Figure 5.7 Comparison of emission spectra of 35Å and 44Å quantum-well structures....................141

Figure 6.1 CIE Chromaticity diagram showing Illuminant $D_{65}$....................147

Figure 6.2 CIE Color-matching functions from 1931 and 1978....................148

Figure 6.3 White LED structure using red, green, and blue active regions...........151

Figure 6.4 Change in color coordinates vs. fractional flux variation..................152

Figure 6.5 White LED structure using violet and yellow active regions.............153

Figure 6.6 CIE chromaticity diagram showing two complementary wavelengths combining to make white light at Illuminant $D_{65}$....................154

Figure 6.7 I-V characteristic of p-n junction....................157

Figure 6.8 Ideality factor plot for p-n junction....................159

Figure 6.9 Electroluminescence spectra of green LED under high injection current ....................161

Figure 6.10 Electroluminescence spectra of green LED under low injection current....................162

Figure 6.11 Electroluminescence spectra of yellow/amber LED under high injection current …………………………..…………………………163

Figure 6.12 Electroluminescence spectra of yellow/amber LED under low injection current………………….……………..…………………164

Figure 6.13 Photographs of LED #S069-06 operating at (a)10 mA and (b) 2mA…..165

Figure 6.14 PL spectra of yellow-emitting device structure………………………...166

Figure 6.15 Calculated values of electron-hole pair concentration for a series of ND-filtered laser beams……………………………………..168

Figure 6.16 Calculated values of electron-hole pair concentration for a series of injection currents……………………………………………169

Figure 6.17 I-V Characteristics of yellow and green devices………………………170

Figure 6.18 Ideality factor plots for yellow and green devices……………………...171

Figure 6.19 PL emission spectra of white-emitting devices composed of 2x2 QW's………………………………………………………….174

Figure 6.20 PL emission spectra of white-emitting devices composed of 3x3 QW's……………….…………………………………………174

Figure 6.21 PL emission spectra of white-emitting devices composed of 4x4 QW's………………………………………………………….175

Figure 6.22 Chromaticity diagram showing the complementary white structures grown with the TSS-CCS……………………………………………177

# 1.0 General Background

## 1.1 A Brief History of Electric Light

On October 21, 1879, the world was witness to one of the most significant events in the history of invention. A man named Thomas Alva Edison, also known as "The Wizard of Menlo Park," demonstrated the world's first incandescent light bulb [1]. Composed of a carbon filament sealed under vacuum in a glass housing, this rudimentary photon source had a lifetime of forty hours and demonstrated to the world that electric-powered lighting was now a reality.

To this day, Edison's incandescent bulb (now generally containing an iodized tungsten filament) remains in widespread use. The fluorescent light, conceived by Nikolai Tesla and introduced by the Westinghouse Electric Company in 1939 [2], is also a common electrical lighting source. However, a promising new technology is quickly emerging which may soon make both incandescent and fluorescent lights obsolete. This technology, referred to as solid-state lighting, uses semiconductor-based devices to transform electrical power into emitted photons.

The fundamental principles of solid-state lighting are fairly straightforward. In a semiconductor with bandgap $E_g$, recombination of an electron-hole pair (EHP) leads to the release of an amount of energy equal to $E_g$. One way this energy can be released is through emission of a photon. The wavelength, $\lambda$, of this emitted photon is governed by the bandgap of the semiconductor material according to $\lambda = hc/E_g$. Thus, a light source of a desired wavelength can be engineered by using a semiconductor with the proper bandgap.

The first serious research regarding solid-state lighting occurred in the early 1960's. It was known at this time that a forward-biased GaAs p-n junction would emit infrared radiation. GE's Nick Holonyak took this technology a step further by alloying GaAs with GaP, thus creating a material that emitted red light when a current was passed through it [3]. Devices were fabricated from this material, and thus the world's first light emitting diode (LED) was introduced.

Since the arrival of Holonyak's first LED, the advances in this area have been tremendous. Not only has Holonyak's red been improved, but the entire visible spectrum is now available. Figure 1.1 shows the rapid improvement in luminous efficiency as time has passed and more dollars and man-hours have been spent studying the phenomenon of solid-state lighting. An approximate ten-fold improvement per decade can be seen.

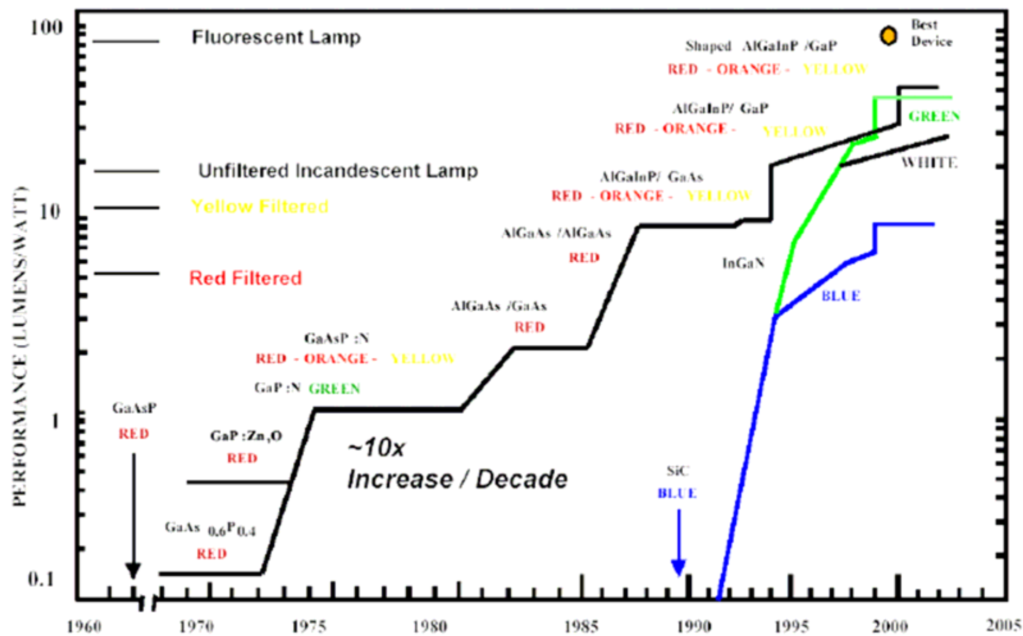


Figure 1.1 Evolution of LED technology [4]

## 1.2 The Measurement of Light

In order to fully understand solid-state lighting, one must first become familiar with the way in which the physical properties of light are measured. Generally, electromagnetic radiation is characterized by *radiometric* quantities, such as number of photons, photon energy, and radiant flux [5].

The use of radiometric units, however, can be somewhat misleading when trying to measure visible lighting. This is because the human eye does not sense all wavelengths of light equally. Sensitivity is maximized near the center of the visible spectrum (555 nm) and tails off in either direction. This is demonstrated in Figure 1.2, which shows eye sensitivity as a function of wavelength.

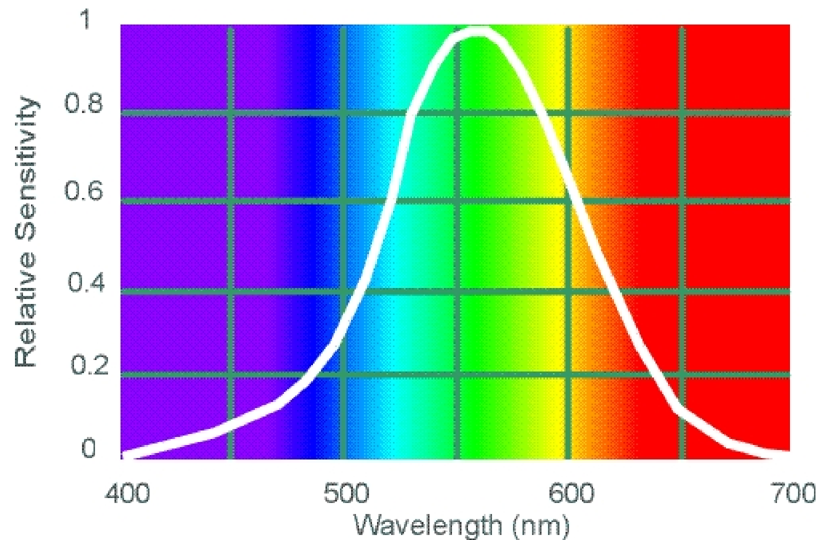


Figure 1.2 Relative sensitivity of human eye to visible wavelength [6]

Radiometric units do not take this sensitivity dependence into account. In fact, radiometric units do not even differentiate between visible and invisible (infrared,

ultraviolet, etc.) radiation. Thus, the use of radiometric quantities for visible light sources is far from ideal.

For this reason, *photometric* quantities have been introduced. Photometric quantities are used to characterize light according to the sensitivity of the human eye [5]. An example is the *luminous flux*, which represents the light power of a source as perceived by the human eye. Luminous flux is measured in units of lumen (lm).

Another important photometric quantity is *luminous efficacy*—the luminous flux per unit power measured in units of lumens/watt. It is related to quantum efficiency, but there is an important distinction between the two. Whereas quantum efficiency simply measures the electron-to-photon conversion capability of the light source, the luminous efficacy weights the light output as per the photopic response of the human eye [7].

For example, typical blue LED's have a much higher quantum efficiency (60%) than do green LED's (20%) [8]. However, because of each color's location on the eye sensitivity chart (Figure 1.2), the typical luminous efficacy of green LED's is three times higher than that of blue LED's (~ 30 to 10 lumens/watt) [9].

## 1.3 Advantages of LED's

The next issue is to examine what advantages LED's have over standard (i.e., incandescent and fluorescent) lighting sources. As with any new technology, a solid argument must be made as to why, and in what ways, the new product is superior to the existing product.

The first major advantage of solid-state lighting is lifetime. By some estimates, LED's offer a hundred-fold increase relative to their incandescent counterparts. This

advantage is particularly attractive for applications where bulb replacement is especially difficult or impossible.

The ruggedness of LED's is also an asset. An incandescent or fluorescent light can be shattered or crushed, and if an incandescent bulb is dropped, even if the glass remains intact, one may find the filament has broken. LED's, on the other hand, can handle such shock and still operate properly. LED's are also much more resistant to vibration than their incandescent counterparts.

Perhaps the greatest advantage of LED's, however, is their superior efficacy. Incandescent bulbs are inherently inefficient, due to the fact that 72% of their emitted radiation is in the infrared range [10]. This leads to typical efficacy values of 15-20 lumens/watt [8], numbers which, given the maturity of the technology, will not be increasing much, if at all. Using a filter on an incandescent bulb to create a monochromatic (single-color) light reduces the efficacy even more (12 lm/W for yellow, 5 lm/W for red).

Monochromatic LED's, on the other hand, are currently being manufactured with efficacies several times higher (see Table 1.1). Also bear in mind that solid-state lighting technology is still in its early stages. As more research is needed into the growth and processing of LED's, efficacy values will continue to improve.

Table 1.1 Top efficacies of single-color LED's currently in production [8]

| Color | Efficacy (lumens/watt) | Manufacturer | Material system |
|---|---|---|---|
| Red | 42 | Lumileds | Phosphide |
| Red-orange | 53 | Lumileds | Phosphide |
| Orange | 18-22 | Toshiba | Phosphide |
| Yellow | 34-35 | Lumileds | Phosphide |
| Yellow-green | 8 | P. Tec Opto | Phosphide |
| Green | 25-32 | Nichia | Nitride |
| Blue-Green | 25-28 | Nichia | Nitride |
| Blue | 9-12 | Cree | Nitride |

Of course, these improvements in efficacy will lead to a decrease in energy consumption as LED's gradually replace incandescent sources for many, if not all, applications. The U.S. Department of Energy predicts that, by the year 2020, the use of SSL will lead to a savings of *at least* 18 terrawatt-hours (TWh). Note that this value was obtained using their most conservative (base-case) estimates; more ambitious models call for a potential savings of up to 246 TWh [11].

This decrease in energy consumption will lead to a subsequent decrease in carbon emission from power plants, which has obvious environmental benefits. The base-case calculations estimate a decrease of $3.16 \times 10^6$ metric tons of carbon by 2020, while the more optimistic models claim the reduction could be an order of magnitude higher ($4.21 \times 10^7$ metric tons).

The advantages discussed in this section are why LED's are rapidly replacing their peers in lighting applications all around the industrialized world. It seems everything from advertising displays to traffic signals, we are seeing the emergence of solid-state lighting. This fact hit home just recently when my eight-year old neighbor, Ethan, proudly showed me his new sneakers. His favorite feature was – to my amusement – a series of red LED's than lit up every time he took a step.

### 1.3 White Light using LED's?

As ubiquitous as single-color LED's have become, we have really only just seen the beginning of how solid-state lighting can enhance our lives. The real revolution in lighting technology will occur if (when?) we are able to replace our conventional white light source with LED's.

The most straightforward way to generate white light is to simply combine monochromatic light of the three primary colors: red, green, and blue (RGB). This will produce a white source matching the RGB sensors of the human eye [12]. This is often demonstrated by the 1979 CIE (Commission International de l'Eclairage) chromaticity diagram shown in Figure 4.

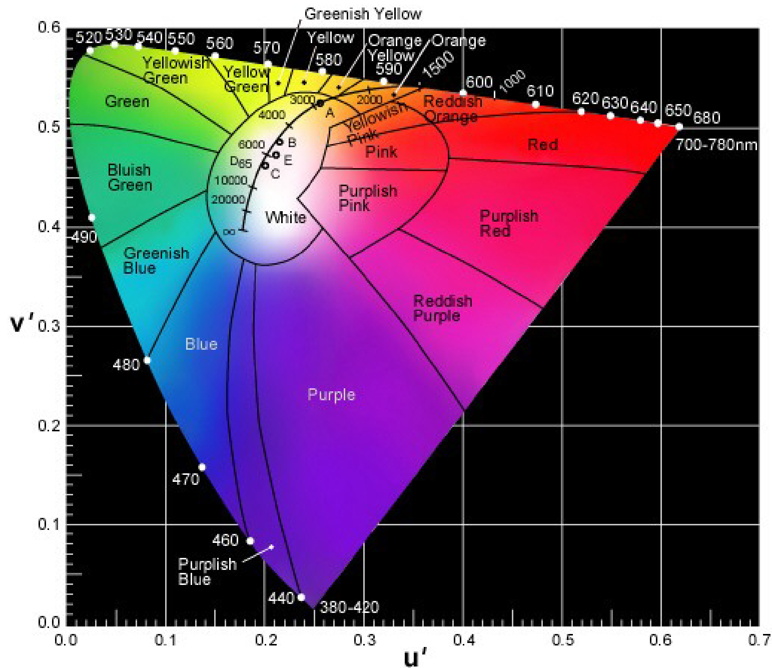


Figure 1.3 CIE Chromaticity Diagram (1976) [13]

The axes of the chromaticity diagram (u', v') are referred to as the uniform chromaticity coordinates, and are a representation of the relative stimulation of the human eye to the three primary colors. The points of the perimeter of the diagram represent *saturated* colors, meaning those which consist of a single wavelength [5]. (Note the white dots labeled in 10 nm increments.) Such a color would appear as a single vertical line on an intensity vs. wavelength plot (i.e., a photoluminescence measurement). A broadening of this line would correspond to the point on the edge chromaticity diagram moving inward toward the center. Continued broadening will lead a wide spectrum which is composed of all colors (i.e. white light), which is found in the center of the diagram.

When examining the white region of the chromaticity diagram, one may notice a solid line traveling through it. This line is referred to as the blackbody locus, or

Planckian locus, because it indicates the coordinates of the light given off by a blackbody emitter as its temperature is increased. If LED-generated white light is to be sufficient quality, it must fall upon this line [14].

The position along the locus is quantified by the parameter known as correlated color temperature (CCT). Its physical definition is the temperature at which a black body must be heated in order to emit the given color of light [15]. Candlelight, for example, has a relatively low CCT of 1500K, and thus appears reddish-orange in color. Incandescent and fluorescent lights operate at a CCT of around 2500-3500K; this is a reasonable target for white LED's.

Another important parameter for measuring the quality of electric light is the color-rendering index, $R_a$. It is defined as the ability of an illumination source to render true colors [15]. Its values are given on a scale of 0-100. The mid-day sun has $R_a \approx 100$, as do most incandescent bulbs. White LED's should posses an $R_a$ of at least 75 for use in indoor lighting. However for some applications, such as outdoor streetlights, a lower color-rendering index ($R_a \approx 40$) is acceptable.

The question now becomes: is it possible to create white light of sufficient quality through solid-state technology? The answer, at first glance, appears to be affirmative. Currently, the technology exists to manufacture LED's whose colors span the entire visible spectrum. It should then simply be a matter of putting the three primary colors (red, green, and blue) in one device and thus have a white LED.

Of course, this task is not as simple as it sounds. Currently, long wavelength (red-yellow) LED's are manufactured with the gallium phosphide family of materials ($Al_xIn_yGa_{1-x-y}P$) [16], whereas shorter wavelength devices are nitride-based [17]. Due to

lattice incompatibilities, it is not possible to incorporate both materials into the same device. Our study must therefore begin with the choice of the appropriate material.

### 1.4 Potential of the Gallium Nitride Material System for Solid-State Lighting

When one looks to the materials that can potentially be used in the fabrication of white LED's, the compound semiconductor gallium nitride (GaN) emerges as a candidate. First of all, GaN is a direct bandgap material (see Figure 1.4), which means that electron-hole pairs will combine radiatively, i.e. through photon emission. This is in contrast to indirect bandgap materials, in which recombination tends to be non-radiative.

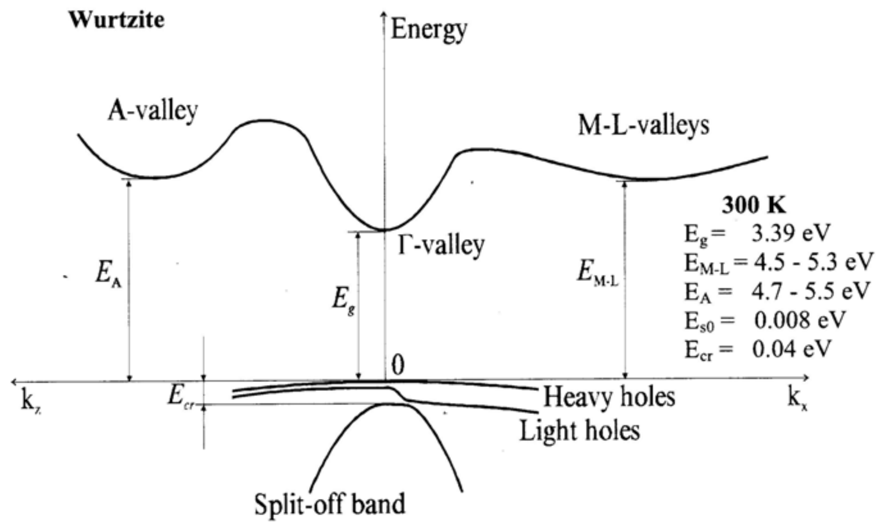


Figure 1.4 E-k diagram of gallium nitride [18]

Another positive aspect of GaN is that it can be alloyed with related compounds aluminum nitride and/or indium nitride to form ternary compounds AlGaN and InGaN, or the quaternary compound AlInGaN. Starting with the binary GaN ($E_g$ = 3.4 eV), one can theoretically alloy InN (or AlN) into GaN, and decrease (or increase) the bandgap in a

controlled fashion.  As shown in Figure 1.5, the GaN material system can thus be used to cover a very broad range of bandgap values (0.7 - 6.1 eV), and thus a wide span of emission wavelengths (200 – 1378 nm) that covers nearly of the visible spectrum. Use of the quaternary material, AlInGaN, has the added advantage of giving one the ability to independently control both bandgap and lattice parameter [19].

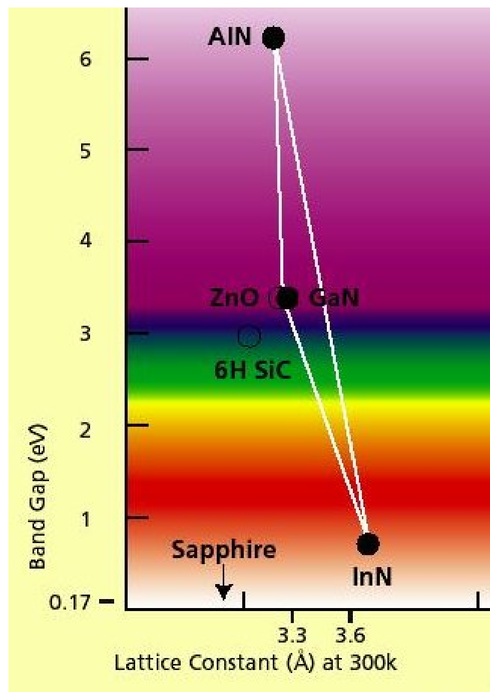


Figure 1.5  Bandgap vs. lattice constant for nitride material system [20]

The ability of the ternary compound InGaN to push the emission wavelength of GaN into the visible range is a very advantageous property of this material system. Through use of a series of InGaN alloys, each with an increasing value of In content, it appears feasible to fabricate blue, green, and red emission on the same chip (i.e., a white LED).  Thus, this study will focus on the use of InGaN as its active layer in all device structures.

It is also important to note that all of the GaN-based alloys that have been discussed (InGaN, AlGaN, and AlInGaN) have direct bandgaps over their entire composition range. This is in contrast to the aforementioned $Al_xIn_yGa_{1-x-y}P$ system (see Section 1.2), which converts to an indirect bandgap for $E_g > 2.33$ eV (which corresponds to $\lambda$=532 nm, i.e. green emission) [21]. For this reason the phosphide system is not a viable candidate for monolithic white LED's.

Thus far the discussion of solid-state white lighting has focused on the placement of three active regions, one for each primary color, on a single chip. There is, however, another way in which LED's can be used as a white light source. It involves the use of a single short-wavelength (UV or blue) device coated with an epoxy containing one or more phosphors [22]. The purpose of the phosphor(s) is to absorb the high-energy photons from the LED and convert them to longer wavelengths. This method has proven very successful through use of nitride-based LED's and rare-earth ion ($Ce^+$ [23] or $Eu^+$ [24]) based phosphors.

This technique, however, suffers from a few major drawbacks. First, there is an inherent inefficiency present in these sources due to the conversion of high-energy blue or UV photons to low-energy yellow or red. Also, the lifetimes of these LED's are shortened by the yellowing of the epoxy with holds the phosphors, which is attributed to both photodegradation and ohmic heating at the p-n junction [25]. Therefore, it is certainly beneficial to explore the possibility of the three-color InGaN device described previously, as such device would circumvent both of the major problems seen in phosphor-converted LED's.

The following chapters in this dissertation are broken down as follows: Chapter 2 explains the fundamentals of metal-organic vapor deposition (MOCVD), which is the film growth technique used in this study. Chapter 3 provides the necessary background information behind the study of GaN, and presents the preliminary GaN growth data. N- and p-type doping are also discussed. Chapter 4 explains the fundamental challenges related to InGaN growth, then provides the experimental results of our InGaN growth study. Chapter 5 focuses the calculation of emission wavelength from InGaN-based structures, while Chapter 6 presents long-wavelength device results as well as a demonstration of white emission. The dissertation concludes with Chapter 7, which summarizes the project and suggests ideas for future research in this field.

## 1.7 References


1. T. A. Edison. U.S. Patent No. 223,898 (1880).

2. Twenty First Century Books, an online Tesla information resource: http://www.tfcbooks.com/teslafaq/q&a_028.htm

3. N. Holonyak, Jr. and S.F. Bevacqua. "Coherent (visible) light emission from $Ga(As_{1-x}P_x)$ junctions." *Appl. Phys. Lett.* **1**, 82 (1962).

4. M. Krames. "Progress and future direction of LED technology." SSL Conference Presentation. Arlington, VA. (2003).

5. E.F. Schubert. *Light-Emitting Diodes,* Chapter 11.2. Cambridge University Press, Cambridge (2003).

6. P.K. Kaiser. *The Joy of Visual Perception: A Web Book*. Found online at http://www.yorku.ca/eye/photopik.htm

7. D.A. Kirkpatrick. "Is solid-state the future of lighting?" *Proc. of the SPIE Vol. 5187: Third Internat'l. Conf. on Solid-State Lighting.* I.T. Ferguson, N. Narendran, S.P. Denbaars, J.C. Carrano, eds. (2003).

8. M.G. Craford. "Visible light emitting diodes: past, present and a very bright future." *MRS Bull.* **25** (10), 27 (2000).

9. D.L. Kleipstein. The Brightest and Most Efficient LED's and Where to Get Them. Found online at http://members.misty.com/don/led.html

10. S.H. Lydecker, K.F. Leadford, C.A. Ooyen. "Lighting industry acceptance of solid state lighting." *Proc. of the SPIE Vol. 5187: Third Internat'l. Conf. on Solid-State Lighting.* I.T. Ferguson, N. Narendran, S.P. Denbaars, J.C. Carrano, eds. (2003).

11. M. Kendall and M. Scholand. "Energy savings potential of solid state lighting in general lighting applications." Final report prepared by Arthur D. Little, Inc. for the U.S. Department of Energy (2001).

12. D.A. Steigerwald, J.C. Bhat, D. Collins, R.M. Fletcher, M.O. Holcomb and M.J. Ludowise. "Illumination with solid state lighting technology." *IEEE J. on Sel. Top. in Quant. Elec.* **8**, 310 (2002).

13. Ledtronics, Inc. homepage. Found online at http://www.ledtronics.com/datasheets/Pages/chromaticity/097.htm

14. S. Muthu. "Red, green, and blue LEDs for white light illumination." *IEEE J. on Sel. Top. in Quant. Elec.* **8**, 333 (2002).

15. Lighting Design Glossary. Found online at http://www.schorsh.com/kbase/glossary/

16. F.A. Kish and R.M. Fletcher. "AlInGaP Light-Emitting Diodes." *Semiconductors and Semimetals, Vol. 48: High Brightness Light-Emitting Diodes.* G.B. Stringfellow and M.G. Craford, eds. Academic Press, San Diego (1997).

17. S. Nakamura, S. Pearton and G. Fasol. *The Blue Laser Diode: The Complete Story,* Chapters 9 and 10. Springer, Berlin (2000).

18. Ioffe Physico-Technical Institute electronic archive: Physical properties of semiconductors. Found online at http://www.ioffe.rssi.ru/SVA/NSM/Semicond/index.html. Diagram is adapted from M. Suzuki, T. Uenoyama and A. Yanase. "First principles calculations of effective-mass parameters of AlN and GaN." Phys. Rev. B. **52**, 8132 (1995).

19. M.E. Aumer, S.F. LeBoeuf, F.G. McIntosh, and S.M. Bedair. "High optical quality AlInGaN by metalorganic chemical vapor deposition." *Appl. Phys. Lett.* **75**, 3315 (1999).

20. EMF Limited homepage. Found online at http://www.emf.co.uk/

21. C.H. Chen, S.A. Stockman, M.J. Peanasky and C.P.Cuo. "OMVPE of AlGaInP for high-efficiency visible light-emitting Diodes." *Semiconductors and Semimetals, Vol. 48: High Brightness Light-Emitting Diodes.* G.B. Stringfellow and M.G. Craford, eds. Academic Press, San Diego (1997).

22. R. Mueller-Mach, G.O Mueller, M.R. Krames, and T. Trottier. "High-power phosphor-converted light-emitting diodes based on III-nitrides." *IEEE J. on Selected Topics in Quant. Elec*. **8**, 339 (2002).

23. J.L. Wu, S.P. Denbaars, V. Srdanov, H. Weinberg. "Cerium doped garnet phosphors for application in white GaN-based LEDs." *Materials Research Society Proceedings Vol. 667: Luminescence and Luminescent Materials Symposium*, p G5.1.1 (1999).

24. J.K. Park, M.A. Lim, J.T. Park, S.Y. Choi. "White light-emitting diodes of GaN-based $Sr_2SiO_4$:Eu and the luminescent properties." *Appl. Phys. Lett.* **82**, 683 (2003).

25. N. Narendran, Y. Gu, J.P. Freyssinier, H. Yu, L. Deng. "Solid-state lighting: failure analysis of white LED's." *J. Crys. Gr.* **268**, 449 (2004).

# 2.0 Metal-Organic Chemical Vapor Deposition

## 2.1 Introduction to MOCVD

As discussed in the previous chapter, the GaN material system has been shown to be excellent candidate for solid-state lighting. The next step, therefore, is to determine the technique through which the GaN-based devices can be manufactured. For this particularly study, metal-organic chemical vapor deposition (MOCVD) has been chosen.

Metal-organic chemical vapor deposition (MOCVD) is a thin-film growth technique which involves the flow of gaseous precursors (usually, as the name implies, metal-organics) into a reaction chamber, which will contain a heated substrate. When the precursors reach this substrate, they are “cracked” (i.e., decomposed), which leads to a series of chemical reactions between the reactive species created by the cracking process. The result of these reactions is the deposition of a thin film on the substrate.

The flow of metal-organic is achieved by passing a carrier gas (usually hydrogen, nitrogen, or some mixture of the two) through a bubbler containing the metal-organic in either liquid or solid form. The molar quantity of metal-organic compound entering the chamber is governed by the bubbler temperature, bubbler pressure, and the flow rate of carrier gas through the bubbler.

The basic building blocks for MOCVD-growth of gallium nitride are well-defined. The most common gallium source (and the one used in this dissertation) is trimethylgallium (TMG), which is readily available from several vendors. There is also some interest in the use of triethylgallium (TEG), which has a much lower vapor pressure than TMG. Some studies have shown that GaN films grown with TEG tend to contain less background carbon [1, 2].

The vast majority of GaN studies, including this one, favor the use of ammonia ($NH_3$) as a nitrogen source. Its cracking efficiency is low at typical GaN growth temperatures (~1000˚C), so relatively large amounts of $NH_3$ must be used for sufficient quality GaN growth (typical molar $NH_3$/TMG ratios ≈ 1000-3000). Dimethylhydrazine (DMHz), a nitrogen-containing organometallic, has also been experimented with as a nitrogen source [3], as has hydrazoic acid ($HN_3$) [4].

The carrier gas used in this study was nitrogen. This is in contrast to most current MOCVD systems, in which hydrogen is used as a carrier. Hydrogen was introduced independently into the reactor in most cases, due to its beneficial thermal conductivity and carbon-radical scouring properties. However, there are certain instances (InGaN growth, for example) in which the presence of hydrogen is detrimental to the growth (see Chapter 4). Our growth system affords us the opportunity to completely eliminate the flow of hydrogen into the reactor when desired, which can be a major advantage when growing InGaN-based structures.

## 2.2 Thomas Swan Scientific MOCVD System

All samples studied in this body of work were grown by an Epitor MOCVD system manufactured by Thomas Swan Scientific Equipment Ltd (Swavesey, Cambridge, UK). A diagram of the gas-delivery portion of the system is given in Figure 2.1.

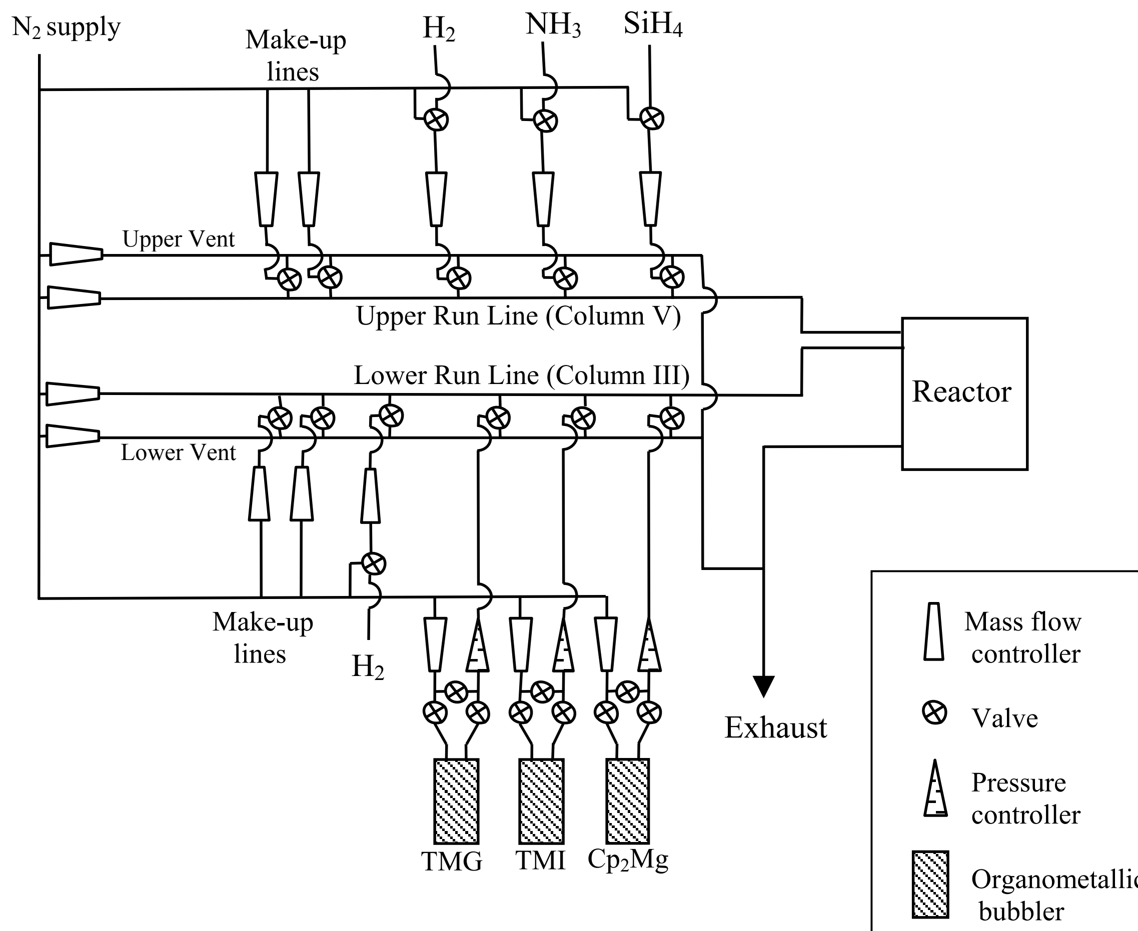


Figure 2.1 Diagram of Thomas Swan MOCVD gas delivery circuit

The main components of the gas delivery manifold are the carrier gas supply, upper/lower vent lines, upper/lower run lines, make-up lines, organometallic (OM) bubblers, and gaseous reactant sources. The appropriate materials will flow from this circuit into a reactor, where the film growth will take place. Reactor designs will be discussed in detail in Section 2.3.

The description of system operation starts with the carrier gas. As can be seen in Fig. 2.1, the carrier gas is introduced into the manifold upstream of all the other components, and thus is used as the base flow for all processes. The Swan system is

designed in such a way that either hydrogen or nitrogen can be used as a carrier gas; in the present work it is nitrogen.

Since the carrier gas is used ubiquitously in system processes, its purity is of obvious importance. For this reason, a Nanochem 1400 resin purifier was used to reduce contaminants in the carrier $N_2$. Monitoring the purity of the carrier $N_2$ was carried out by a Panametrics hygrometer. Throughout all processes described herein, the dewpoint reading remained below the detectable range of the hygrometer (-110°C), which corresponds to an $H_2O$ concentration less than 2 ppm.

The carrier gas flows through the upper (column III) and lower (column V) run lines, carrying all reactants present in these run lines into the reactor. The use of two separate run lines is essential because the OM sources used as column III precursors are Lewis acids; whereas ammonia, the primary column V source, is basic [5]. Therefore any pre-mixing between the two will lead to gas-phase reactions which are detrimental to the film growth process. Also, it is important, when performing growth, to ensure that the total flow through each run line is properly balanced; otherwise backstreaming into the lower-flow line may occur.

Coupled with each run line is a corresponding vent line. These vent lines are simply paths through which a reactant flow can be diverted if it is not, at that particular time, desired in the reactor. Further downstream, the two vent lines combine and then pass through a pyrolysis furnace, which decomposes any potentially hazardous OM's before they are released to the exhaust.

The precursors themselves are either from a gaseous source (as in the case of $H_2$, $NH_3$, and $SiH_4$) or an organometallic (such as TMI, TMG, and $Cp_2Mg$). The gaseous

sources are simply fed into the delivery manifold from a remote high-pressure tank. The OM precursors are held in temperature- and pressure-controlled bubblers, through which the carrier gas travels when an OM flow is needed. The molar quantity of OM "picked up" and sent into the run lines (and subsequently the reactor) is governed by the bubbler temperature, bubbler pressure, and carrier gas flow rate.

One of the novel aspects of the Thomas Swan deposition system is its utilization of make-up lines. The purpose of these lines is to eliminate any variation in flow through the run lines which may result from the switching of reactant flows from the run line to the vent (and vice-versa). Such perturbations can lead to rough interfaces between epitaxial layers, which are unacceptable when dealing with the nanometer-range features of modern semiconductor device structures.

The flow rate and pneumatic switching of these make-up lines are controlled by the TSS system software, which anticipates run-line fluctuations (due to run/vent switching) and eliminates them by flowing the appropriate amount of $N_2$ (or $H_2$) through the make-up lines. The flow from the make-up line compensates for the sudden loss (or gain) of flow that results from switching a reactant stream from the run line to the vent line (or vice-versa). Thus, the reactor experiences a uniform, unperturbed flow despite the switching of reactants and the corresponding epitaxial interface will be appropriately sharp.

### 2.3 MOCVD reactors

Of course, in addition to the gas manifold, another important set of design criteria in an MOCVD system is that of the reactor. It must contain components which are able

to heat the substrate to temperatures greater than 1000°C, rotate the substrate (to reduce boundary layer thickness), and be non-reactive.

*2.3.1 Early reactor design*

The first reactor used for the growth of gallium nitride was a “home-made” chamber designed and constructed in our lab.  A drawing of this reactor is given in Figure 2.2.

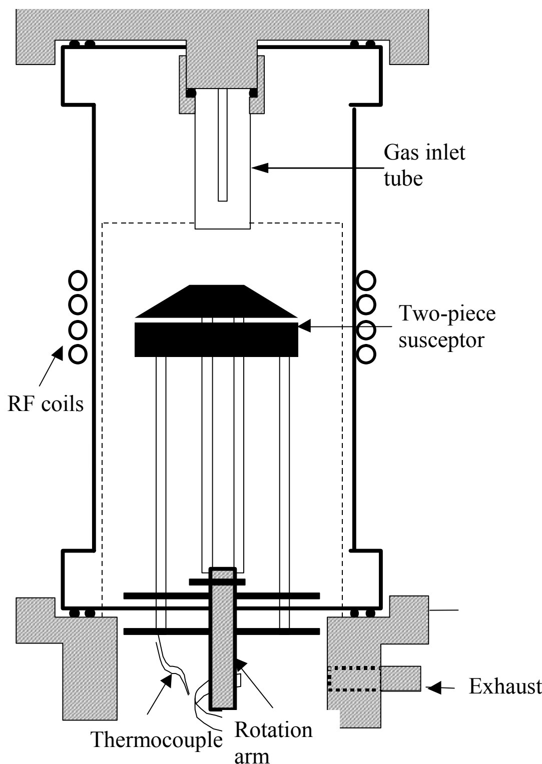


Figure 2.2  Original GaN reactor design [6]

Work with this reactor, however, never yielded any material of sufficient quality. There were several recurrent problems, such as poor film surfaces, low (<80 $cm^2$/V-sec) mobilities, and emission dominated by deep levels.  A series of minor modifications were made to this reactor in an attempt to address these problems, but none of the changes led to an improvement in the grown films.

There are a litany of problems inherent in this particular system design which led to the repeated poor-quality films. These issues are discussed as follows:

- *Gas phase reactions* – Due to the relatively large distance (>100 mm) between the inlet and susceptor, the ammonia and metalorganics would meet well above the growth surface. As mentioned previously, this leads to an acid-base pre-reaction which is detrimental to film growth.
- *Recirculation pockets* – Another design flaw with this reactor was the dead volume above the susceptor to the right and left of the sample. At high process temperatures, thermal buoyancy likely lead to recirculating air pockets in these areas. These disturbances can disrupt the laminar flow of the reactant gas stream over the substrate surface, leading to poor film quality.
- *Jetting* – As can seen in the figure, the reactor featured a small inlet tube injecting gases into much larger volume. This leads to the phenomenon of jetting, wherein the inlet gases rapidly expand to fill the open volume. This phenomenon also leads to perturbations in the laminar flow, and negatively affects film growth.
- *Exposure of chamber to atmosphere* – Since there was no load-locked glovebox in this setup, the interior of the reactor was exposed to atmosphere every time a sample was loaded or unloaded. This may have lead to the presence of residual water vapor in the reactor during growth, even after the pre-growth cycle purge. Also, post-growth exposure of the reactor to atmosphere could have potentially led to reactions (i.e., oxide formation) with the metals deposited on the on the wall after growth. This is particularly troublesome when working with Al- or Mg-containing films.

*2.3.2 Thomas Swan Scientific close-coupled showerhead reactor [7]*

Due to the problems with the above reactor, it became necessary to take a new approach. It was decide the best course of action was to purchase the close-coupled showerhead (CCS) reactor designed and manufactured by Thomas Swan Scientific. This reactor was then fully installed by the author. A diagram is shown in Figure 2.3.

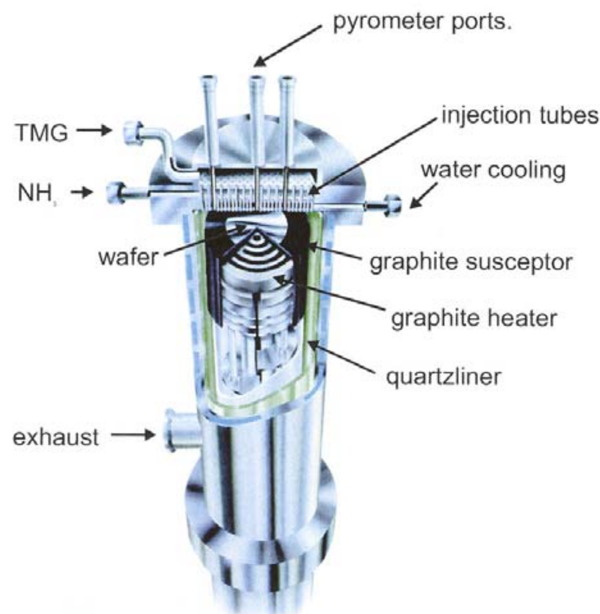


Figure 2.3 Thomas Swan Scientific close-coupled showerhead (TSS-CCS) reactor [8]

The TSS-CCS is a vertical, axially symmetric rotating disc reactor [9] based on the stagnation-point concept [10]. The chamber itself is stainless steel, with a removable quartz inner-liner to prevent deposition on the interior walls. The input gases are introduced laterally into the chamber and delivered to the substrate via TSS's patented showerhead. The substrate sits on a silicon carbide-coated graphite susceptor, which is heated resistively, and rotated via a Ferrofluidic™ [11] double magnetic fluid/bearing assembly.

Perhaps the most significant benefit of this reactor is the close proximity of the susceptor to the gas inlet (~2 cm). This leads to a reduced residence time of the reactants over the substrate, which (a) helps to prevent gas-phase reactions between column III metalorganics and ammonia; and (b) leads to enhanced interface abruptness. Another advantage of this design is that it results in a very small volume above the susceptor, which minimizes the formation of re-circulating gas pockets. It is also important to note that, despite this short length, the reactants are believed to be fully mixed when they reach the susceptor. This assessment has been verified by mathematical analysis [12].

The showerhead itself (shown in Figure 2.4) is another one of the major benefits of this reactor. It is composed of a very high-density (~100 tubes/in$^2$) set of inlet tubes, with every-other tube being either column III or column V. The size of the showerhead is matched to the size of the susceptor (in this case, 2 in. diameter). Such a design provides a number of advantages over the smaller inlet tube discussed earlier.

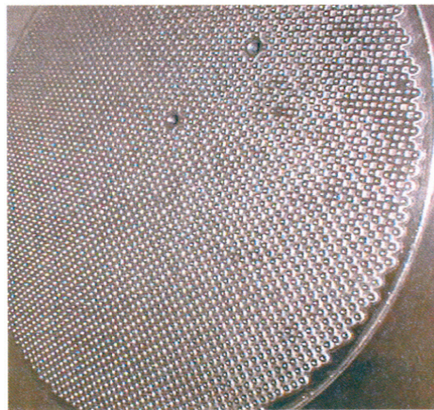

Figure 2.4 Photo of Showerhead [4]

The first such advantage is uniformity. The showerhead introduces a homogeneous mixture of reactant gases over the entire substrate evenly, rather than over

a small area. This eliminates "shadowing" effects, this leading to a uniform thickness profile as well as uniform dopant incorporation and alloy composition, where applicable. This well-controlled inlet technique also helps ensure run-to-run reproducibility.

Another advantage of the showerhead design is the elimination of jetting. As discussed in the previous section, jetting is the phenomenon in which the incoming gases must expand rapidly to fill the reactor volume, thus disrupting the laminar flow. This occurs commonly in reactors where the inlet gases are fed into the chamber by a small tube (see Figure 2.2). The showerhead, on the other hand, provides a diffuse introduction of reactants, therefore jetting is avoided.

The substrate heating in this reactor is achieved through a resistive heater made of pyrolytic boron nitride-coated graphite. In order to eliminate dead volume in the space around the heater, the system is equipped with a heater purge line. Initially, 200 sccm of nitrogen was sent through this line during all growth and baking steps. However, due to heater lifetime issues, the flow rate and gas species of this purge needed to be adapted. As per the recommendation of TSS, the heater purge was increased to 600 sccm of hydrogen. No significant, measurable changes in film properties were noticed due to this alteration.

During all processes, temperature is controlled by a type-C thermocouple placed on the underside of the susceptor, which communicates with a Eurotherm 818 temperature controller. Because of its location, however, the thermocouple does not give a true reading of substrate surface temperature. Thus, an actual temperature vs. thermocouple temperature calibration curve is needed.

Actual surface temperature measurements were obtained in the TSS-CCS reactor through use of its built-in pyrometer ports (see Figure 2.3). Quartz light guides were

fitted into the ports and connected via fiber optic cable to a Mikron M668 optical pyrometer, which provided an actual surface temperature ($T_{act}$) reading. The light guides, cable, and pyrometer were calibrated using an Instron SFL black body furnace. The graphite susceptor was assumed to have an emissivity of 1.0.

Calibration was thus carried out by mimicking the gas-flow parameters for each of the three temperature regimes (buffer layer growth, InGaN growth, and GaN growth/bakeout) and taking a series of actual surface temperature ($T_{act}$) readings using a Mikron M668 optical pyrometer. These values were then plotted vs. the corresponding thermocouple temperature ($T_{TC}$) readings.

Figure 2.5 gives these calibration curves for the two different heater purge conditions used in this study. Note that the values of $T_{TC}$ and $T_{act}$ match much more closely when hydrogen is used as a purge gas, i.e., in the GaN growth regimes of Figure 2(b). This is because the higher thermal conductivity of $H_2$ leads to better heater/substrate coupling.

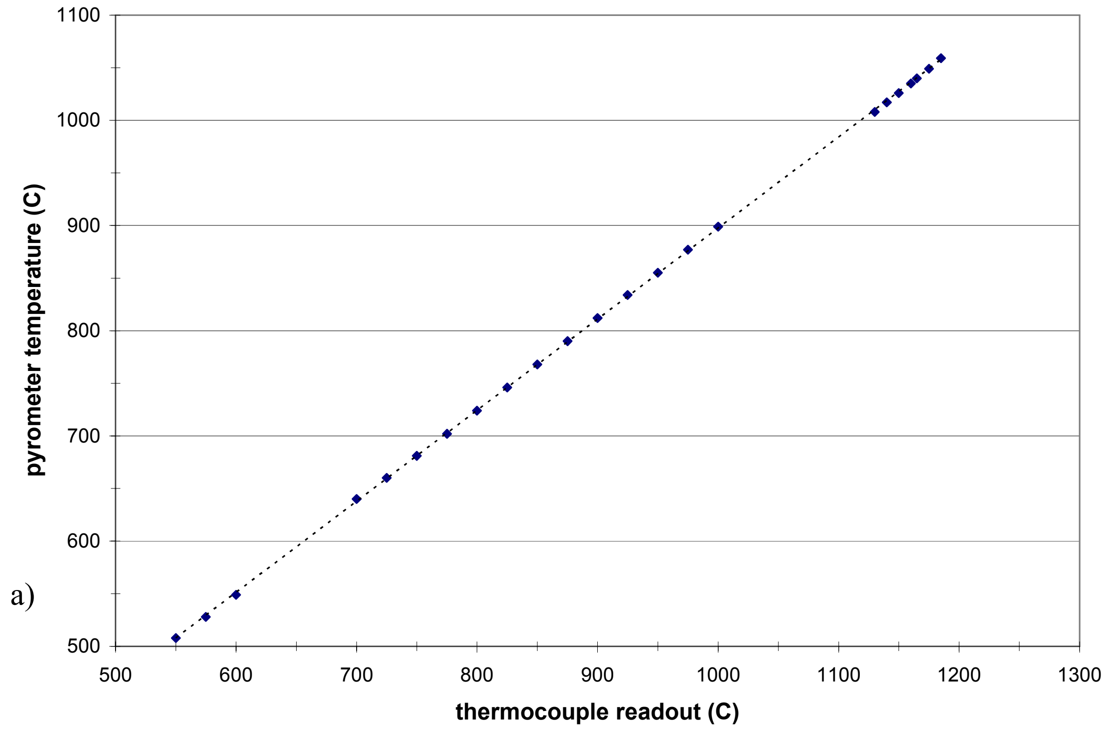


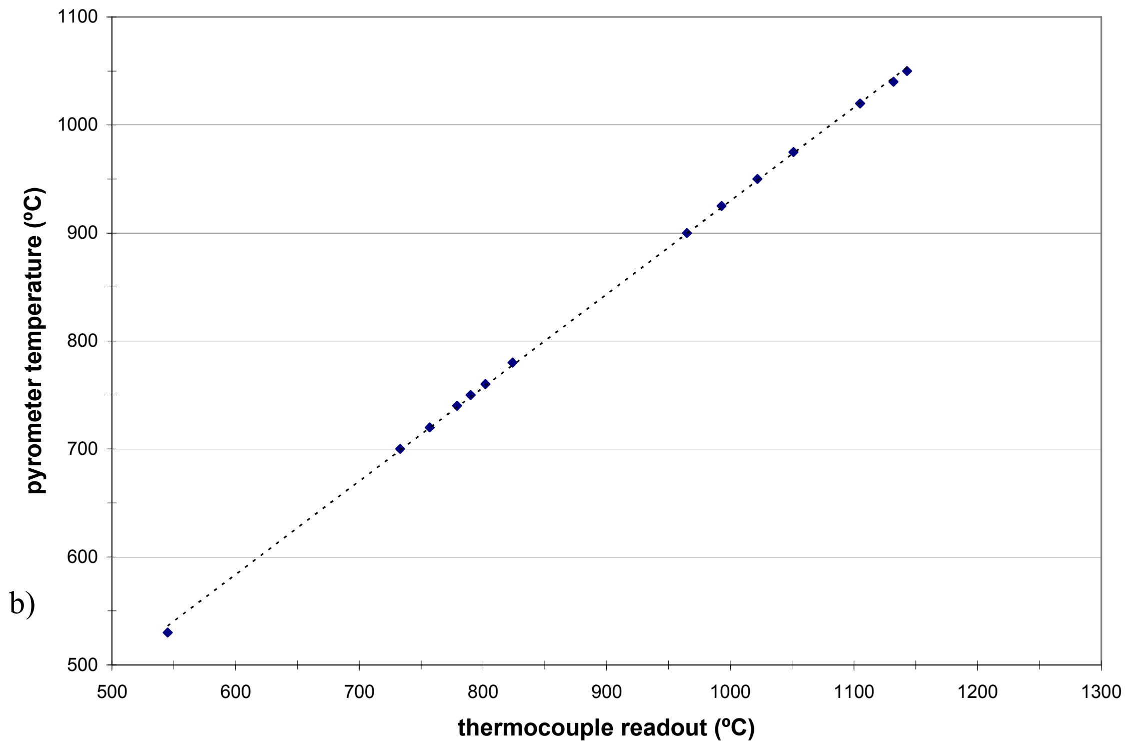


Figure 2.5 TSS-CCS temperature calibration for (a) 300 sccm $N_2$ purge; and (b) 600 sccm $H_2$ purge

It is important to note that all of the growth temperature values reported in this study are actual substrate surface temperatures ($T_{act}$) as per this calibration.

The final major improvement of the TSS-CCS reactor is the presence of a nitrogen-purged glovebox and attached load-lock. These features make it possible to load and unload samples with exposing the interior of the reactor to atmosphere. This will reduce the residual oxygen and water vapor in the chamber during growth and help prevent the formation of oxides which may result from the presence of post-growth metals in the chamber.

## 2.4 References


1. Saxler, D.Walker, P. Kung, X. Zhang, M. Razeghi, J. Solomon, W.C. Mitchel, H.R. Vydyanath. "Comparison of trimethylgallium and triethylgallium for the growth of GaN." *Appl. Phys. Lett.* **71**, 3272 (1995).

2. J.S. Park, Z.J. Reitmeier, R.F. Davis. "Comparison of the microstructure and chemistry of GaN (0001) films grown using trimethylgallium and triethylgallium on AlN/SiC substrates." *Phys. Stat. Sol. (c)* **2**, 2166 (2005)

3. E.D. Bourrett-Courchesne, Kin-Man Yu, S.J.C. Irvine, A. Stafford, S.A. Rushworth, L.M. Smith, R. Kanjolia. "MOCVD of GaN on sapphire using the alternate precursor 1,1-dimethylhydrazine." *J. of Crys. Gr.* **221**, 246 (2000).

4. H. Sato, H. Takahashi, A. Watanabe, and H. Ota. "Preparation of GaN films on sapphire by metalorganic chemical vapor deposition using dimethylhydrazine as nitrogen source." *Appl. Phys. Lett*. **68**, 3617 (1996).

5. R.H. Moss and J.S. Evans. "A new approach to MOCVD of indium phosphide and gallium-indium arsenide." *J. of Cryst. Gr.* **55**, 129 (1981).

6. S.F. LeBoeuf. "Manipulating two-dimensional electron gas properties in III-V nitrides via AlInGaN strain engineering." Ph.D Thesis. North Carolina State University (2001).

7. E.J. Thrush. M. Kappers, L. Considine, J.T. Mullins, V. Saywell, F.C. Bentham, N.Sharma, C.J. Humphreys. "Close coupled showerhead reactors for the growth of group III nitrides." Proc. China-Japan workshop Nitride Semiconductor Materials and devices, p. 119. CJWN, Shanghai (2001).

8. Thomas Swan Scientific Equipment CCS-MOCVD Reactor System Manual – CS62912, Issue 1.1. Technical Author: Trevor Webb (1999).

9. K.F. Jensen. "Transport phenomena in vapor phase epitaxy reactors." in *Handbook of Crystal Growth 3, Thin Films and Epitaxy, Part B: Growth Mechanisms and Dynamics*, p 541. D.T.J. Hurle, ed. North Holland Publishing (1994).

10. N.A.V. Piercy. *Aerodynamics,* Chapter II.32. D. Van Nostrand Company, Inc., New York (1937).

11. "Ferrofluidic" is a registered trademark of Ferrotec (USA) Corporation. A technical description of how such a bearing operates can be found at http://www.ferrotec.com/usa/sealing_overview.htm

12. T.G. Mihopolous, S.G. Hummel, K.F. Jensen. "Simulation of flow and growth phenomena in a close-spaced reactor." *J. of Cryst. Gr.* **195**, 725 (1998).

# 3.0 Fundamentals of Gallium Nitride

## 3.1 Crystallography of Gallium Nitride

There are two allotropes of gallium nitride: cubic and hexagonal. The vast majority of research in the GaN field focuses on the stable hexagonal form, including the work presented herein. However, there has been a significant amount of attention paid to the metastable cubic phase, which will be discussed briefly below.

The atoms in cubic GaN (c-GaN) are arranged into a zinc blende (also known as sphalerite) structure, space group $\bar{4}3m$ [1]. This arrangement is achieved by the juxtaposition of two FCC unit cells (one with Ga atoms and one with N atoms), with a displacement ¼ length along the cubic diagonal, as shown in Figure 3.1.

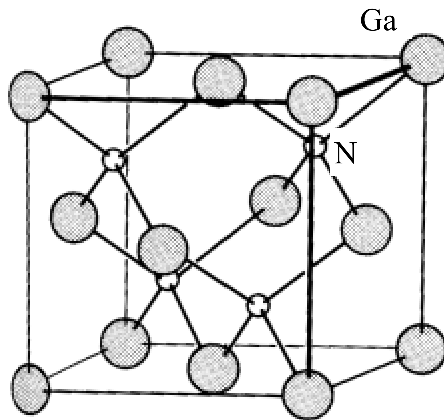


Figure 3.1 Zinc blende structure [2]

The lattice parameter of this allotrope gallium nitride is 4.52Å; its bandgap is 3.28 eV [3]. As is the case with hexagonal gallium nitride (h-GaN), c-GaN is normally grown using MOCVD [4,5] or molecular beam epitaxy (MBE) [6,7]. The most common

substrate in either case is gallium arsenide, despite the large (~20%) lattice mismatch between c-GaN and GaAs [5].

There are several intriguing aspects of cubic GaN that make it a potentially useful material. First of all, due to its inversion symmetry, there is no spontaneous polarization present in the material [8]. (The importance of this fact will become clearer in Section 3.2, when spontaneous polarization in hexagonal GaN is discussed). The higher symmetry of the cubic crystal, as compared to its hexagonal counterpart, should also lead to lower phonon scattering and thus higher mobilities [4,9]. Additionally, it is believed that cubic GaN may be more amenable to p-type doping [10]. Synthesis of ternary alloys does not appear to be prohibitively problematic, as successful growth of cubic AlGaN [11] and InGaN [12] has been reported.

However, there are also many difficulties inherent in the growth of c-GaN. As mentioned earlier, there is a large lattice mismatch between c-GaN and GaAs which makes epitaxy challenging. Also, due to the metastability of c-GaN, it is very difficult to grow material that is purely cubic; appreciable amounts of the stable hexagonal subdomains tend to form during growth [9,13,14].

The hexagonal form of GaN is by far the more commonly-studied allotrope. Its atoms assume the wurtzite structure (space group $P6_3mc$) [1], which is shown in Figure 3.2.

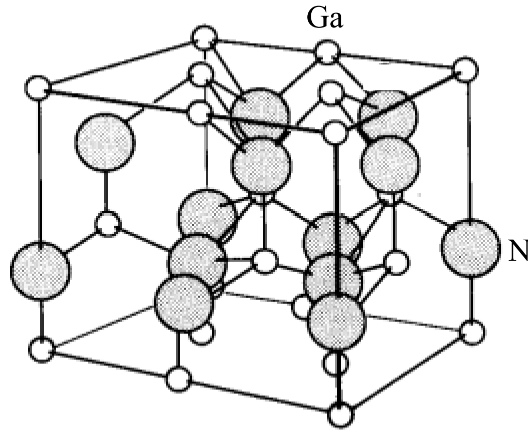


Figure 3.2 Wurtzite structure

All samples in this study were grown under conditions conducive to wurtzite GaN, thus the remainder of the dissertation will focus exclusively on this crystal structure.

## 3.2 Growth of Gallium Nitride

### *3.2.1 Growth techniques*

The first report of the growth of GaN was published in 1969 [15]. Since that time, scientists have done extensive experimentation with many different growth techniques in an attempt to learn which ones are best suited for high-quality material. Thirty-five years of research into this field has led to two preferred techniques: metal-organic chemical vapor deposition (MOCVD), which was discussed in the preceding chapter, and molecular beam epitaxy (MBE).

MBE is, essentially, a very highly-controlled evaporation technique [16]. Growth takes place in an ultrahigh vacuum (UHV) chamber ($P \sim 10^{-10}$ torr), which contains a heated substrate as well as series of effusion cells which contain the desired metal

reactants. These cells are positioned in such a way that, when heated in the UHV environment, they form a beam of evaporated material which then re-deposits onto the substrate. In the case of MBE nitride growth [17], ammonia is introduced as a nitrogen source. Otherwise, pure nitrogen is sent to the chamber and subsequently ionized, creating a plasma which provides the reactive nitrogen species required for growth.

One of the advantages of MBE is that it offers researchers the use of real-time diagnostic tools, such as reflective high-energy electron diffraction (RHEED), which can be used to extract growth information that is impossible to obtain during MOCVD. However, there are several disadvantages to MBE as well. First of all, working with UHV presents an additional level of difficulty not present in MOCVD. Also, due to the slow growth rates inherent in the MBE process, this growth technique is not used in large-manufacturing where process time is a critical parameter.

MBE-grown materials have certainly shown a great deal of promise, however, this dissertation will focus exclusively on MOCVD.

### *3.2.2 Substrate issues*

One of the early problems with the growth of gallium nitride was lack of suitable substrates for homoepitaxy. Due to its high melting temperature and high pressure, GaN crystals cannot be made by typical techniques like Czochralski or Bridgeman. (In fact, even today, high quality, affordable GaN substrates are not available in large quantities.) Instead, GaN was grown heteroepitaxially, most commonly on c-plane (0001) sapphire. However, due to the large lattice parameter and thermal conductivity mismatch ($\Delta a_0$ = 16.1%, $\Delta\alpha_T$ = 25.5%) [18], the resultant films were of poor crystal quality.

A major breakthrough occurred in 1986 when Akasaki and Amano reported that a low-temperature "buffer layer" of AlN, when grown under the right set of conditions, drastically improved the quality of GaN-on-sapphire [19]. A low-temperature buffer layer of GaN was found by Nakamura to have similar beneficial effects [20].

C-plane sapphire is by no means the only substrate upon which high-quality GaN can be grown. Silicon carbide is a very common (albeit costly) alternative [21,22]; and reports of GaN grown successfully on (111) silicon [23], zinc oxide [24], and spinel ($MgAl_2O_4$) [25] have been published. The use of alternate crystallographic orientations of sapphire, such as a-, r-, and m-plane [26,27,28], has been studied as well. In all cases, some form of buffer layer was required to compensate for the lattice parameter and thermal conductivity mismatches between film and substrate. All GaN samples discussed in this dissertation were grown on c-plane sapphire with a GaN buffer layer.

*3.2.3 Pre-growth procedure*

The growth of the buffer layer is one of several pre-growth steps that must be carried out in order to achieve high-quality GaN on sapphire. These steps are as follows:

1) Substrate bake (T~1100˚C) in the presence of hydrogen
2) Nitridation of the sapphire surface
3) Buffer layer growth
4) High-temperature anneal of the buffer layer

The substrate bake is important for two reasons. First, it desorbs any trace impurities (such as water or hydrocarbons) that may have condensed on the substrate surface. Additionally, the process conditions present during the bake (i.e., high temperature and hydrogen overpressure) lead to the formation of highly-reactive atomic

hydrogen species. These species interact with the sapphire substrate, depleting it of oxygen and promoting the formation of an aluminum-rich surface phase [29]. The existence of such phase has been verified experimentally [30,31], and its stability confirmed through first-principles calculations [32].

This restructured substrate surface then undergoes a process which is referred to as nitridation. During this step (which can be performed at high ($T=T_{bake}$) or low ($T=T_{buffer}$) temperature), a flow of $NH_3$ is introduced into the chamber and subsequently cracked. The substrate, whose chemical potential was enhanced by the previous bake step, readily reacts with the volatile nitrogen species. This leads to the formation of a surface layer of AlN [33, 34], upon which the buffer layer can be grown.

Buffer layers are grown at relatively low temperatures (500-600ºC), thus making it possible for a high nucleation density to be achieved. Additionally, this low surface temperature leads to a reduction in adatom mobilities. Under such conditions, the Volmer-Weber growth mode is favored, which means the buffer layer will be composed primarily of 3-D islands. The crystal structure of the material in this layer is predominantly cubic [35].

The final step in the pre-growth process is the high-temperature anneal, in which the substrate/buffer layer is slowly brought up to growth temperature and held for a short time. This causes two important processes to take place: (1) the 3-D islands grown at low temperature coarsen and coalesce into a smooth, continuous layer; and (2) the crystal structure of the layer evolves into a mostly hexagonal morphology. It is upon this smooth hexagonal surface that device-quality GaN can be grown [35].

## 3.3 Defects and Structure of Epitaxial Gallium Nitride

A simplified diagram depicting the structure of epitaxially grown GaN is given in Figure 3.3.

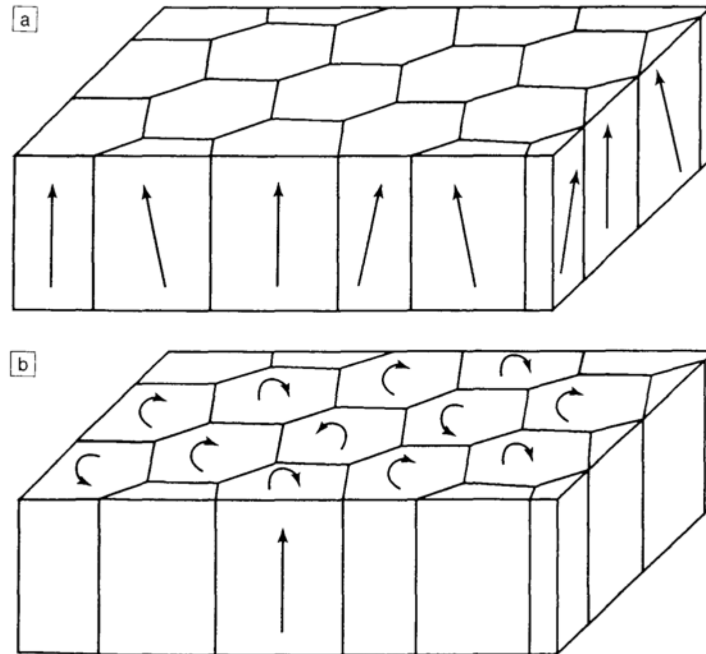


Figure 3.3  Columnar model of III-nitrides [36]

As can be seen in the figure, GaN films are composed of a cellular arrangement of columnar crystallites.  The grains are misoriented towards one another in two ways: there is a *tilt* in the columns with respect to the growth axis (Fig 3.3a), and there is a *twist* of each column's orientation with respect to the growth axis (Fig 3.3b).  This type of structure is commonly referred to as a mosaic structure.

There are four measurable parameters of a mosaic structure.  The first of these is the lateral coherence length, which is the average size of the columns in the lateral (i.e., perpendicular to growth) direction.  Next is the vertical coherence length, which is the

average length of the columns in the growth direction (i.e., film thickness). The remaining two parameters are tilt angle and twist angle. Table 3.1 lists a range of typical values for these parameters for GaN as reported by Chierchia *et. al.* [37] and Metzger *et. al.* [38].

Table 3.1 Typical values of mosaic parameters in GaN

| Mosaic parameter | Typical value [37] | Typical value [38] |
|---|---|---|
| Tilt angle | 0.05-0.08° | 0.1° |
| Twist angle | 0.08-0.25° | 1.3° |
| Lateral coherence length | 1.0-2.0 μm | 0.15-1.0 μm |

When two similarly-structured crystals are misoriented by a small angle, as in mosaic arrangement described above, their boundaries can be considered to be arrays of dislocations [39]. This means that any material which assumes such a structure suffers from the inherent problem of high dislocation density, ρ. Gallium nitride is no exception. Typical reported values of ρ, even for high quality material, are in the range of $10^8 – 10^{10}$ $cm^{-2}$ [37, 40]. At first glance, this appears to be an obstacle toward the use of GaN-based materials for light emission. Most other III-V materials (GaAs or InP, for example) have been shown to be optically inactive when containing that magnitude of dislocations [41,42].

Gallium nitride, however, does not seriously suffer from this drawback. GaN-based materials still emit quite well, despite these large dislocation densities [43]. This can be explained through analysis of the electronegativity values of the relevant elements (see Table 3.2).

Table 3.2. Electronegativity values of selected elements [44]

| | Electronegativity (Pauling scale) |
|---|---|
| Nitrogen | 3.04 |
| Phosphorus | 2.19 |
| Gallium | 1.81 |
| Arsenic | 2.18 |
| Indium | 1.78 |

Electronegativity, $\chi$, is a parameter which describes the tendency of an atom to attract bonding electrons. It is measured on a relative scale, known as the Pauling scale. One of this parameter's primary uses is to quantify the ionicity of the bond between two dissimilar atoms. A large electronegativity difference ($\Delta\chi \geq 0.9$) indicates a strong ionic character to the bond.

As can be seen from the data in Table 3.2, the bonding in GaAs ($\Delta\chi = 0.37$) and InP ($\Delta\chi = 0.43$) is primarily covalent, whereas GaN ($\Delta\chi = 1.23$) has a much more ionic character to its bonding. This is a key distinction because the electronic properties of ionically-bonded materials are fundamentally different than those of covalently-bonded materials [45]. Particularly, the surfaces of ionic materials do not exhibit Fermi level pinning, i.e., the surface-related energy states are either few in number or energetically located outside the bandgap [43,46]. This non-pinning behavior has been verified experimentally by I-V measurements of GaN-metal contacts [47]. For this reason, surfaces of GaN-based are not expected to act as efficient nonradiative recombination sites.

This argument concerning the electronic behavior of GaN surfaces can be extended to cover dislocations as well, because dislocations are simply lattice interruptions and thus can be considered to be internal one-dimensional surfaces and hence electrically benign. Therefore GaN-based alloys remain key candidates for solid-state lighting materials, despite their high dislocation densities. Dislocations are rendered even more inconsequential when dealing with InGaN alloys, due to the formation of self-assembled, In-rich nanoislands (see Chapter 4).

### 3.4 Polarity in Gallium Nitride

Another way in which the highly directional bonds in nitrides manifest themselves is through the presence of polarity in the as-grown films. Epitaxial growth of wurtzite GaN almost always results in films growth with the [0001] or [000$\bar{1}$] direction perpendicular to the substrate. Since this is the polar axis of the material, the resultant films will exhibit strong polarity.

It is important to be able to distinguish between the two different polarities (Ga-face and N-face) possible in gallium nitride. This issue, however, has become somewhat complicated due to inconsistencies in terminology between different research groups. In the interest of clarity, the present author will adhere to the polarity designations set forth in the "standard framework" suggested by Hellman [48]. These designations will be explained henceforth.

Figure 3.4 shows both polar orientations of GaN. In Figure 3.4(a), the gallium atoms (depicted as white spheres) are shown to have a single bond pointing upwards away from the substrate. This is indicative of growth in the [0001] direction, which is

defined as Ga-face. On the other hand, the configuration in Figure 3.4(b) shows the nitrogen atoms (blue spheres) with a single bond pointing away from substrate. This is an example of growth the $[000\bar{1}]$ direction, which is defined as N-face.

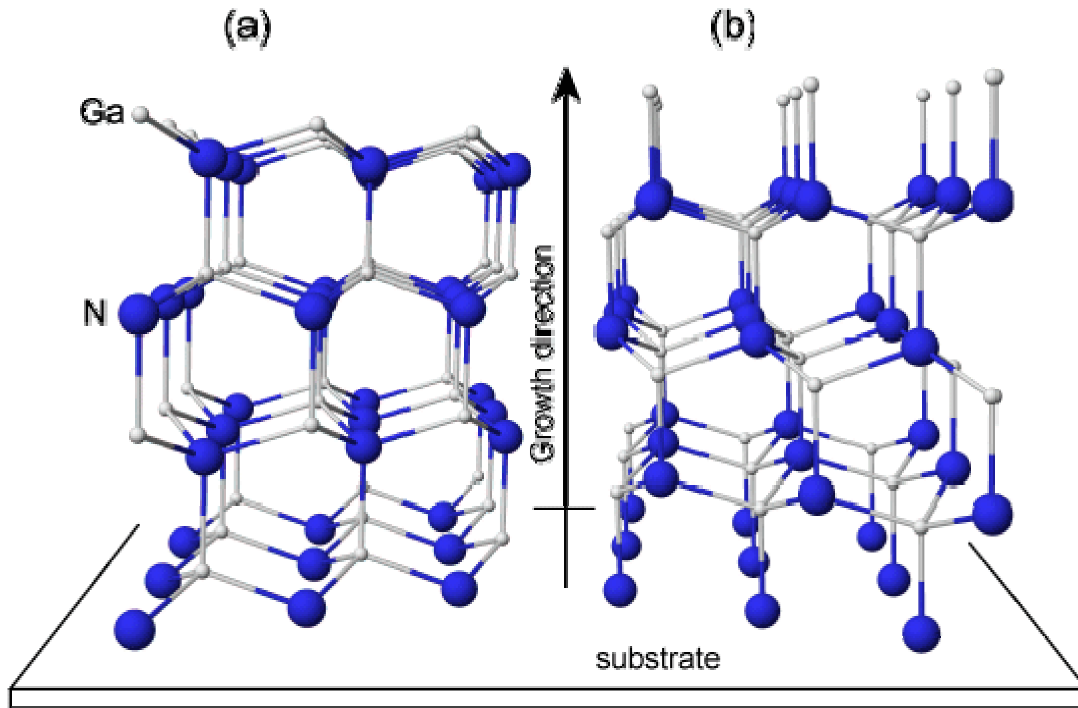


Figure 3.4 (a) Ga-face gallium nitride; and (b) N-face gallium nitride [49]

It is important to bear in mind that polarity is a bulk property, not a surface property. For that reason, the often-used terms “Ga-terminated” and “N-terminated” can be misleading. For example, the structure shown in Figure 3.4(a) can conceptually be capped with a layer of N atoms (ie, be N-terminated). However, the proper polarity designation of the structure remains Ga-face. The terms “Ga-terminated” and “N-terminated”, when used correctly, refer to a surface property only.

There are several ways to measure the polarity of as-grown GaN films, including convergent beam electron diffraction [50], Rutheford backscattering ion channeling [51],

and chemical etching in KOH [52]. Characterization results have consistently shown that high-quality MOCVD-grown films grown with a low temperature buffer layer and having a smooth surface morphology are almost exclusively Ga-face [48]. The GaN samples grown in this study have shown no reason why they should be anomalous, and therefore will be assumed to be Ga-face as well.

One of the consequences of the polarity in GaN is the presence of a spontaneous polarization field, $\mathbf{P}_{sp}$, within the material. The value of this field has been found to be -0.029 $C/m^2$ [53]. The negative sign indicates that the field is pointed towards the substrate (Ga-polar material is assumed). The significance of polarization fields in GaN-based materials will be discussed in greater detail in Chapter 4, when the presence of piezoelectric (i.e., strain-induced) fields are discussed; and in Chapter 5, where calculations describing the effects of polarization fields on emission wavelength will be presented.

### 3.5 Preliminary Growth of GaN – Experimental

The first step in the experimental study of GaN-based devices is, of course, the growth of high-quality nominally-undoped gallium nitride. Once these conditions have been established, this template can be used for further studies into doping, alloying, and finally device growth.

As mentioned previously, the substrate for all growth runs throughout this dissertation was (0001) sapphire. The sapphire was cut and loaded in one of two ways: either (a) a 14x14 mm square positioned in the center of the susceptor, or (b) a 1 in. long

wedge that was placed radially across the susceptor.  Both configurations are shown schematically in Figure 3.5.

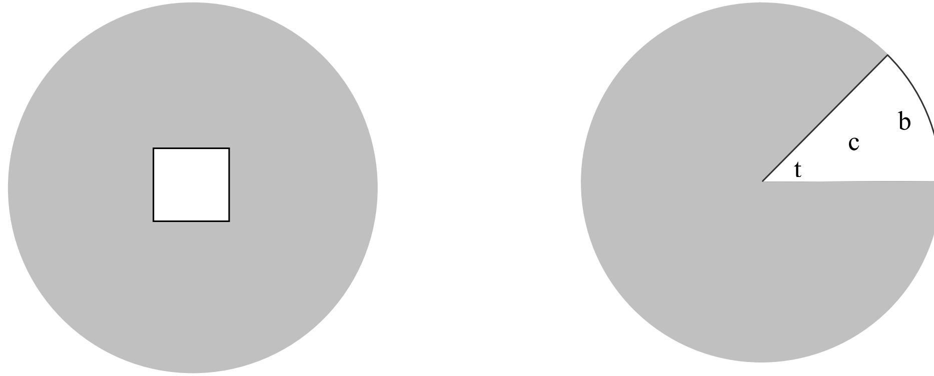


Figure 3.5 Sketch of (a) 14x14mm substrate position in the middle of the susceptor; and (b) 1 in. wedge placed radially across the susceptor.

When using the wedge configuration (b), the wafer was conceptually divided into the following regions (labeled t, c, and b):

(a) the *tip*, which corresponds to the section of the substrate which sits in the middle of the susceptor;

(b) the *center*, which designates the area in the center of the wedge itself; and

(c) the *base*, which corresponds to section of the substrate that sits at the edge of the susceptor.

The advantage of using the wedge configuration is that it allows one to obtain a radial profile of growth across the susceptor.  Such data was critical for this research, as it was found that the 1x2 TSS-CCS reactor showed, in some instances, significant non-

uniformity across the substrate. This nonuniformity became apparent during the study of InGaN growth, and thus will be discussed in Chapter 4.

In all presented data, the shape of the substrate, as well as the measurement location, will be noted. Also, all figures in which data are presented will contain, in the upper right-hand corner, a schematic of the substrate shape and measurement position.

*3.5.1 Optimized Growth conditions for nominally undoped GaN*

Table 3.3 lists the detailed growth recipe that was found experimentally to give the highest quality gallium nitride. This process can also be depicted graphically, as shown in Figure 3.6. Sections 3.5.2 – 3.5.6 will then describe in detail the characterization carried out on the material and, citing the appropriate literature, justify the conclusion that the process outlined in Table 3.3 resulted in the growth of GaN films possessing state-of-the-art quality. This optimization was done using the square-substrate configuration; however, the recipe held true when it was extended over the radius of the susceptor.

Table 3.3 Run conditions for the growth of high-quality undoped GaN

| Step | Temperature (ºC) | Pressure (torr) | TMG flow (µmol/min) | NH3 flow (slm) | H2 flow (slm) | Time (min.) |
|---|---|---|---|---|---|---|
| Bake | 1060 | 200 | -- | -- | 0.6 | 5.0 |
| Nitridation | 530 | 500 | -- | 1.0 | 0.4 | 1.5 |
| Buffer layer | 530 | 500 | 14.2 | 1.0 | 2.5 | 4.5 |
| Buffer anneal | 1040 | 200 | -- | 2.5 | 1.9 | 3.0 |
| Bulk growth | 1040 | 200 | 33.1 | 2.5 | 1.9 | ** |

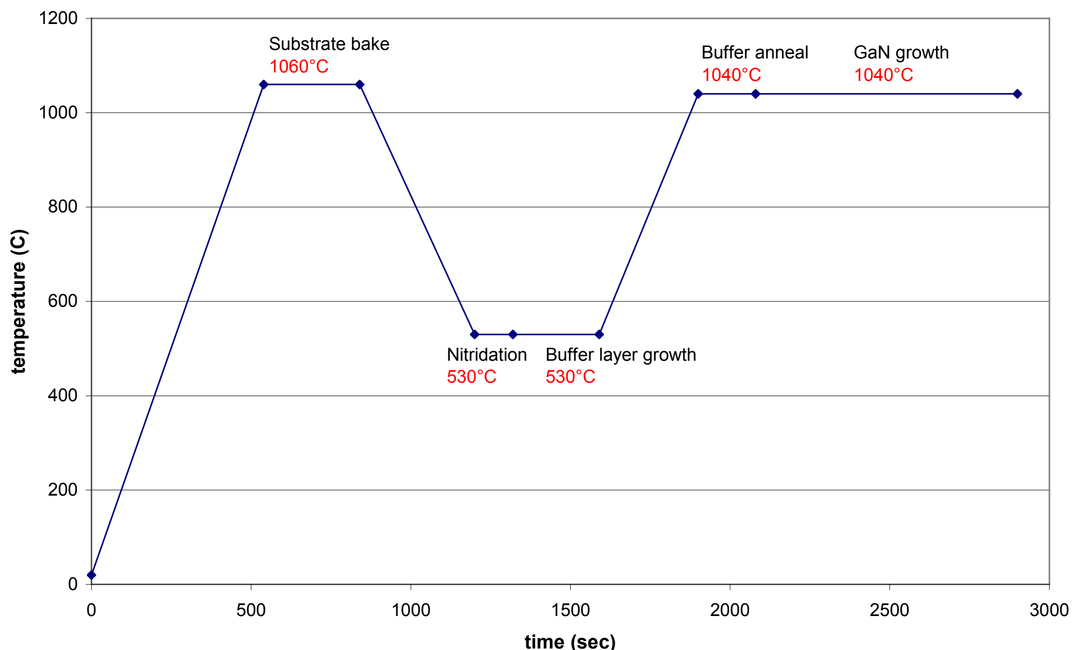


Figure 3.6 Graphical representation of GaN growth process

These process steps, in general, follow the standard accepted recipe for the growth of GaN on sapphire. There is one exception, however: the nitridation is done at buffer layer growth temperature rather than the more common bake temperature. This was as per the recommendation of TSS and was not experimentally altered. Also note that a relatively high chamber pressure is used in this low-temperature nitridation step. This is because, at T~500-600ºC, the cracking efficiency of $NH_3$ is very low. Thus, a higher chamber pressure is necessary in order to provide a sufficient vapor pressure of N to the substrate. The same holds true for the buffer-layer growth step.

*3.5.2 Optical microscopy of nominally undoped GaN*

The first characterization step for all GaN samples was a visual inspection with an

Olympus BX41 optical microscope. The surfaces of high-quality GaN films should be smooth and relatively featureless. Hexagonal hillocks are undesirable, and indicate one or more incorrect parameters in the growth process, particularly the buffer layer.

As mentioned in Section 3.2, proper buffer layers should be grown under conditions conducive to Volmer-Weber (3-D island) growth and consist primarily of cubic-phase material. However, if the growth condition result in the layer being deposited in 2-D Stranski-Krastinov mode and/or in its equilibrium hexagonal form, the buffer layer does no actual "buffering" and a severely mismatched film results. The surface of such a film will covered with hexagonal dendrites, as seen in Figure 3.7 (a). In this particular example, the buffer layer temperature was too high.

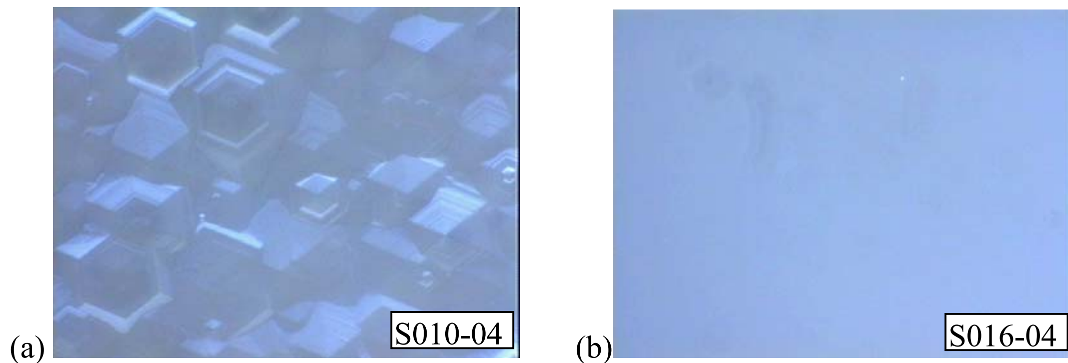


Figure 3.7 Surface of GaN sample grown under (a) non-optimized conditions; (b) optimized conditions

Figure 3.7 (b), on the other hand, shows an optical microscope image from an optimized GaN film grown according to the recipe in Table 3.3. A smooth, featureless surface is noticeable. This is one indication that growth conditions are correct and that the buffer layer has been deposited properly.

*3.5.3 Growth rate measurement of nominally undoped GaN*

Transmission measurements were used to determine the film thickness (and subsequently growth rate) for a nominally undoped sample grown under the optimized conditions given in Table 3.3. Growth time was 180 minutes. The transmission spectrum, which was obtained with a halogen lamp, is given in Figure 3.8.

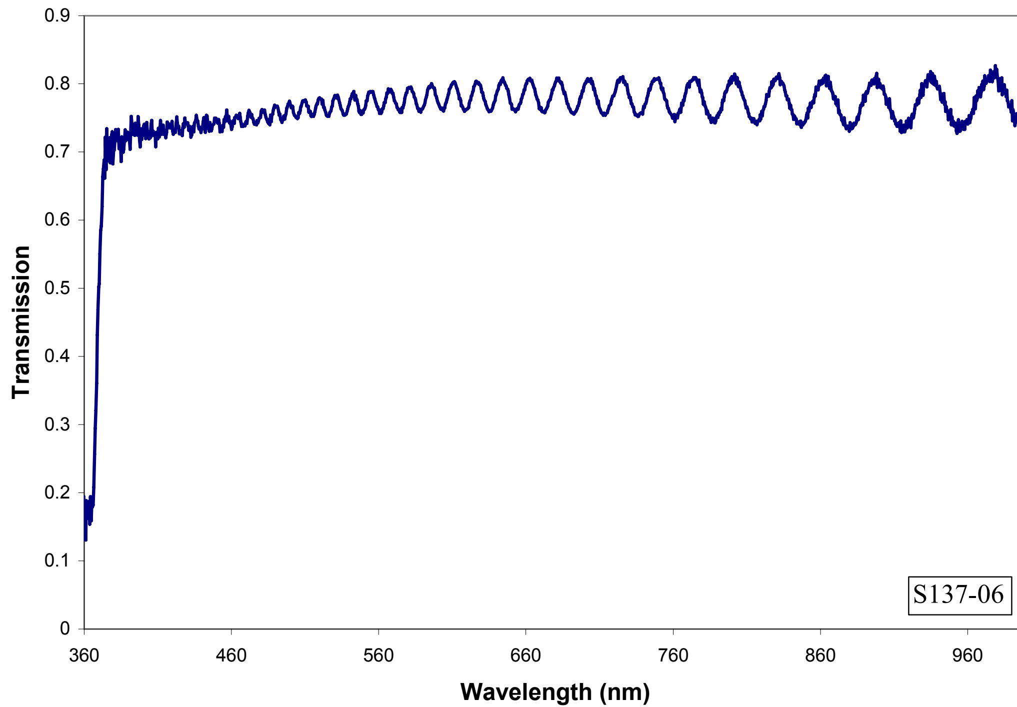


Figure 3.8 Transmission spectra of an optimized GaN film

Measurement of the spacing between the spectrum's interference fringes allows one to calculate the film thickness according to the expression [54]:

$$d = \frac{\lambda_1 \lambda_2}{2(\lambda_1 n_2 - \lambda_2 n_1)} \quad \text{(Eq. 3.1)}$$

where d is film thickness, $\lambda_1$ and $\lambda_2$ are wavelengths of adjacent constructive interference peaks, and $n_1$ and $n_2$ are the corresponding wavelength-dependent index of refraction values (which, for GaN, were found in Ref. 55). Equation 3.1 was carried out for all adjacent pairs of peaks from 499 to 644 nm, resulting in an average thickness value of 4.8 μm. This translates into growth rate of ~1.5 μm/hour. Additionally, by assuming a linear relation between TMG flux and growth rate (which is valid if growth is not $NH_3$-limited), the thickness of the buffer layer can be estimated to be ~ 51 nm. This value is reasonable, but slightly higher than the 10-30 nm range generally reported [56].

### *3.5.4 X-ray diffraction of nominally undoped GaN*

As discussed in Section 3.3, gallium nitride possesses a mosaic microstructure which can be defined by the following four parameters: tilt angle, twist angle, lateral coherence length, and vertical coherence length. By obtaining the values of these parameters, a complete picture of the microstructure can be obtained. Of the four, vertical coherence length is the most straightforward, as it can simply be taken to be the film thickness [57]. The other three values can to be calculated from x-ray diffraction data. XRD can also be used to make estimations of dislocation density (both edge and screw type).

This section will discuss the XRD measurements collected from optimized GaN samples grown according the recipe shown in Table 3.3. The data was collected using a Philips X'Pert MRD with a Cu sealed anode and a four-cyrstal monochromator with Ge (220) configuration. A series of calculations were performed using this data in an attempt to quantify the material's microstructural parameters.

The most straightforward way to obtain the values of tilt angle and lateral coherence length is through measurement of a series of (00*l*) rocking curves [37, 38, 58]. Such on-axis measurements will be independent of twist angle, since twist is an in-plane characteristic. The (002), (004), and (006) reflections were collected for a 3.3 μm-thick film (wedge-shaped substrate, center region) and are shown in Figures 3.9 – 3.11.

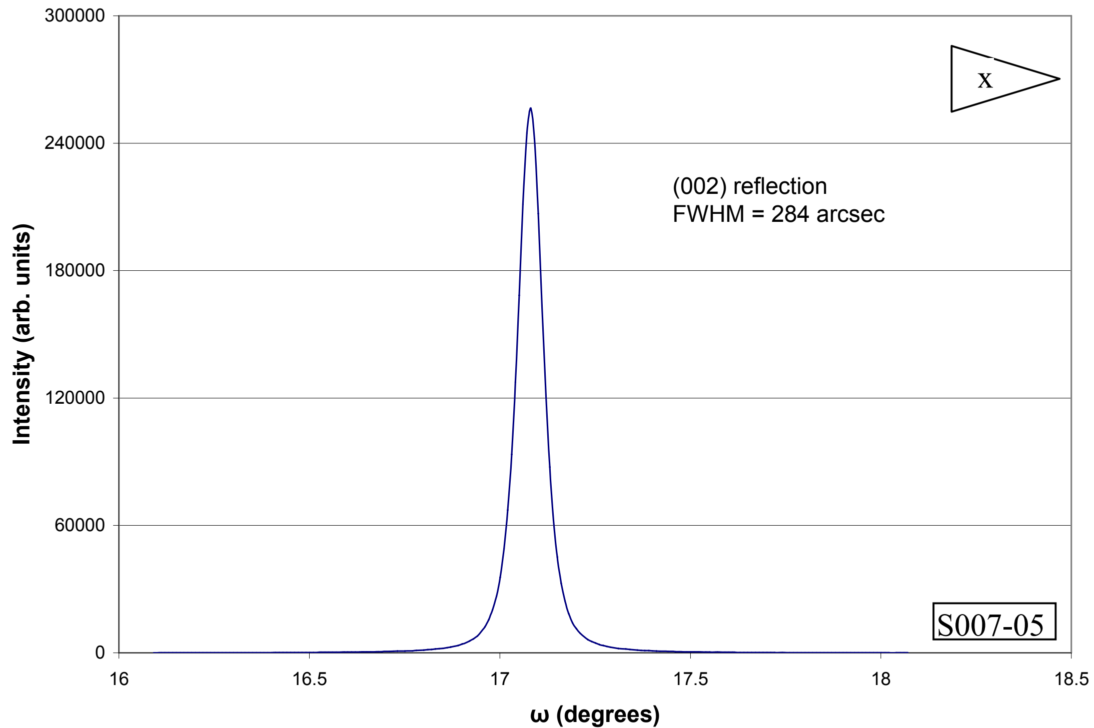


Figure 3.9 X-ray diffraction scan of undoped GaN: (002) reflection

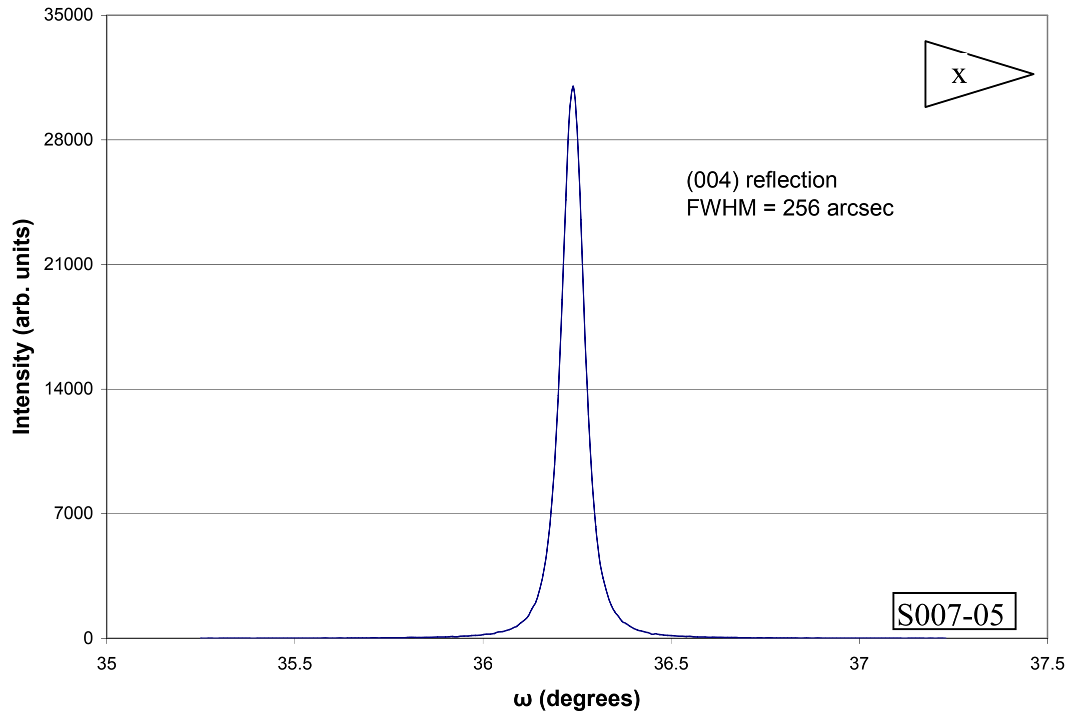


Figure 3.10  X-ray diffraction scan of undoped GaN: (004) reflection

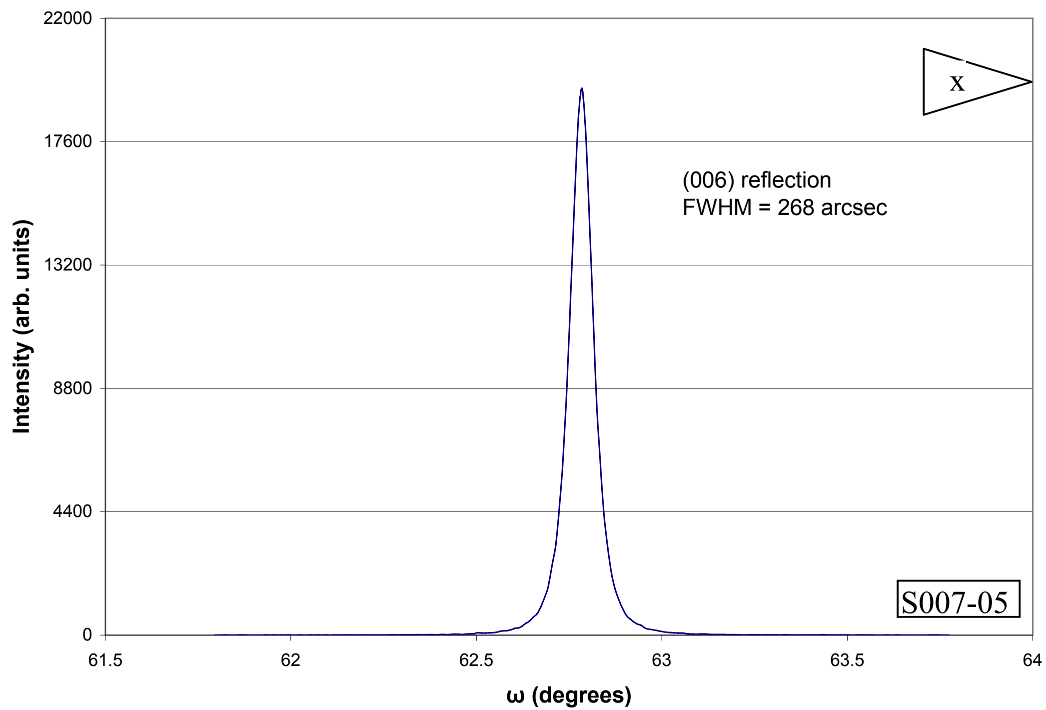


Figure 3.11  X-ray diffraction scan of undoped GaN: (006) reflection

The tilt angle and lateral coherence length can then be determined through a modified Williamson-Hall plot [59], which examines the dependency of linewidth broadening on reflection order. This is carried out by plotting $\beta(\sin\theta)/\lambda$ vs. $(\sin\theta)/\lambda$ for each (00*l*) reflection, where $\beta$ is the full-width at half-maximum, $\theta$ is the scattering angle, and $\lambda$ is the x-ray wavelength (1.54Å in this case). A linear trendline is then fitted to these points; its slope is the tilt angle (in radians) and the inverse of its y-intercept is the lateral coherence length. The Williamson-Hall plot created from the above XRD data is given in Figure 3.12.

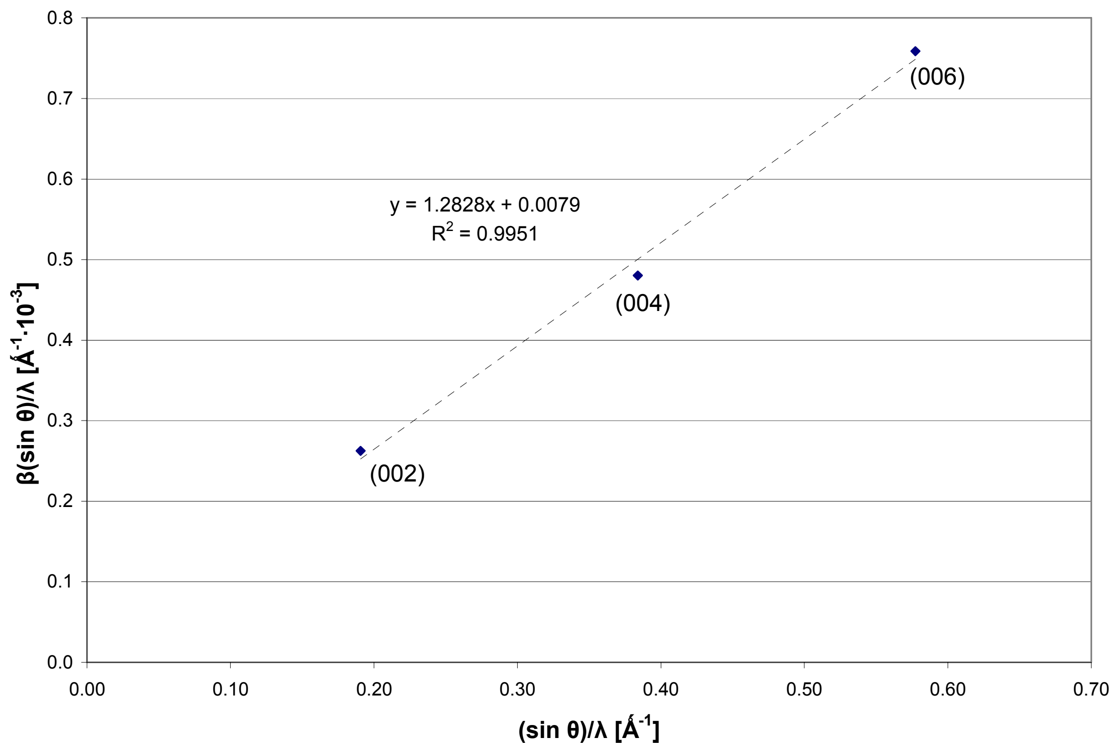


Figure 3.12 Williamson-Hall plot of undoped GaN

From the trendline equation a tilt angle value is obtained: $\alpha_{tilt} = 0.0735^\circ = 264.6$ arcsec. This value fits into the range of what is commonly reported for high-quality GaN

(see Table 3.1). The lateral coherence length (LCL) obtained from this method 12.6 μm. This value is nearly an order of magnitude higher than what should be expected. This apparent discrepancy is probably due to an error in this particular calculation technique. Where Williamson-Hall plots have been shown to be accurate in their calculation of tilt angles, they have been reported by Heinke, *et. al.*, as being less reliable in the calculation of LCL [58].

Additional information can be extracted from off-axis x-ray scans, i.e. (*hkl*) reflections where *h* or $k \neq 0$. These measurements will be sensitive to the mosaic twist in the structure and therefore provide insight into crystal structure that cannot be achieved through (00*l*) rocking curves. The most commonly cited off-axis measurements in the study of GaN are (103) and (302). These scans are given in Figures 3.13 and 3.14.

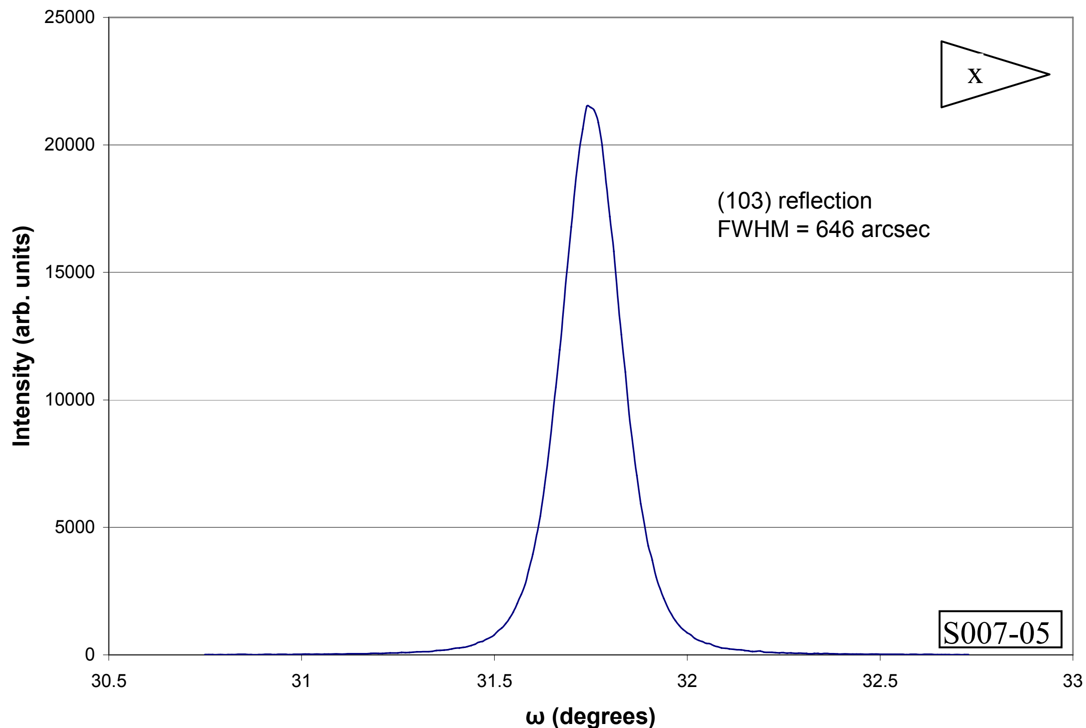


Figure 3.13 X-ray diffraction scan of undoped GaN: (103) reflection

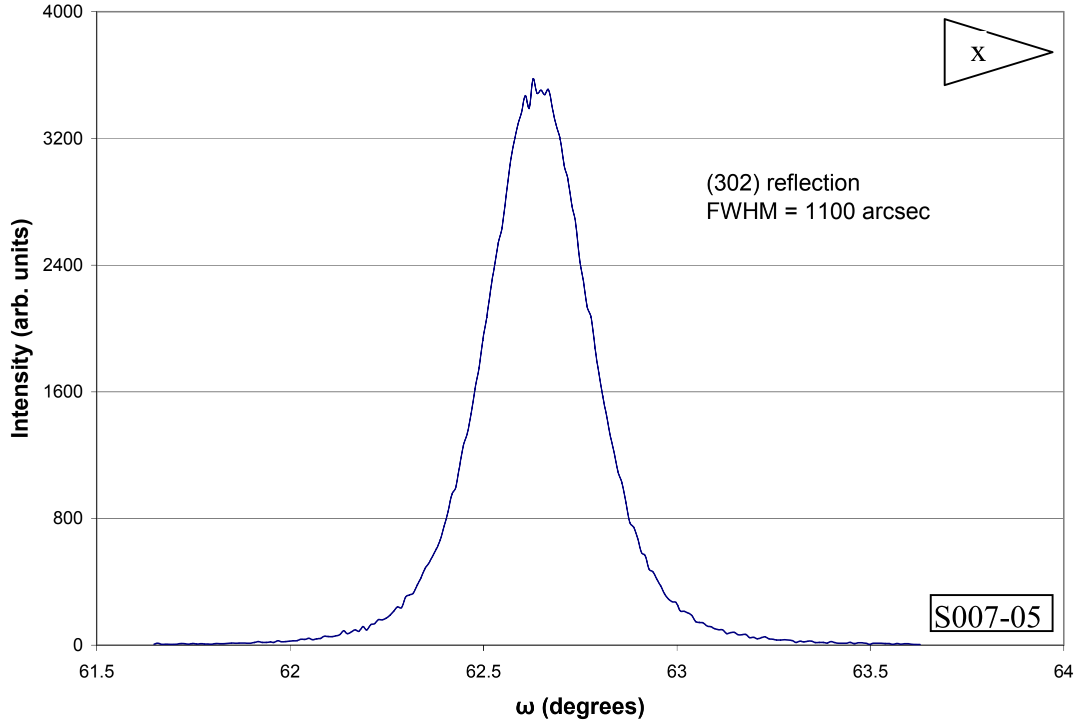


Figure 3.14 X-ray diffraction scan of undoped GaN: (302) reflection

The (302) rocking curve is particularly useful in that it can be used to quickly and easily estimate twist angle using the expression $\alpha_{twist} = 1.14\ \beta_{(302)}$ [60]. This results in $\alpha_{twist} = 0.348^{\circ} = 264.6$ arcsec. This number is within the range of typical reported values for state-of-the-art GaN (see Table 3.1).

Theses tilt angle and twist angle values can be used to calculate dislocation densities in the material as well [61].

$$\rho_{screw} = \frac{\alpha_{tilt}^2}{4.35|b_S|^2} \qquad \text{(Eq. 3.2)}$$

$$\rho_{edge} = \frac{\alpha_{twist}^2}{4.35|b_E|^2} \qquad \text{(Eq. 3.3)}$$

where $|\mathbf{b}_S|$ and $|\mathbf{b}_E|$ are the magnitudes of the Burgers vectors for screw and edge dislocations, respectively.

By definition, edge dislocations are those in which the Burgers vector, **b**, lies perpendicular to the dislocation; whereas in screw dislocations **b** lies parallel to the dislocation [62]. In the case of GaN, the vast majority of dislocations are threading dislocations (which can be edge or screw) that run from the substrate to the surface, i.e. in the c-direction. Thus, the Burgers vector for screw dislocations will also run in the c-direction; $\mathbf{b} = \langle 0001 \rangle$. Edge dislocations, on the other hand, will have **b** in the a-direction; $\mathbf{b} = \frac{1}{3}\langle 11\bar{2}0 \rangle$. The magnitudes of each Burgers vector will then simply be equal to the lattice parameter in the given direction, i.e. $|\mathbf{b}_E| = 0.5185$nm, $|\mathbf{b}_S| = 0.3189$nm.

Calculation of Equations 3.2 and 3.3 yield values of $\rho_{screw} = 1.41\text{x}10^{8}$ cm$^{-3}$ and $\rho_{edge} = 8.36\text{x}10^{9}$ cm$^{-3}$. These values are well in line with what is expected for GaN. Note that the edge dislocation density is over an order of magnitude greater than that of screw dislocations. This difference is also fully expected for this material [see Figure 3.15].

It is important to note that Equation 3.2 and 3.3 assume random distribution of dislocations throughout the material, and therefore the values obtained are accurate only insofar as this assumption is valid. However, as discussed in Section 3.3, materials with the mosaic structure tend to have pile-up of edge dislocations at the boundaries between the columnar subgrains. This calls into question the validity of the “randomness” assumption. A new expression, one which estimates edge dislocation density in the case of complete pileup (complete absence of randomly distributed dislocations), can be introduced [63]:

$$\rho_{edge} = \frac{\alpha_{twist}}{2.1|b_E|L_{\|}} \qquad \text{(Eq. 3.4)}$$

where $L_{\|}$ is the average size of the subgrains, i.e., the lateral coherence length.

Calculation of Equation 3.4 yields an edge dislocation density of $7.17\text{x}10^{7}$ $cm^{-3}$, a value that is much too low to be accurate. The reason for this is the erroneous high value of lateral coherence length obtained from the Williamson-Hall plot. Thus, the edge dislocation density obtained from Eq. 2.2 will be assumed to be the more accurate value.

A summary of the microstructural parameters calculated from the X-ray data is given in Table 3.4.

Table 3.4 Microstructural parameters of undoped GaN

| | |
|---|---|
| $\beta_{(002)}$ (arcsec) | 284 |
| $\beta_{(103)}$ (arcsec) | 646 |
| $\beta_{(302)}$ (arcsec) | 1100 |
| $\alpha_{tilt}$ (°) | 0.0735 |
| $\alpha_{twist}$ (°) | 0.348 |
| LCL (μm) | 12.6 |
| $\rho_{screw}$ ($cm^{-3}$) | $1.41\text{x}10^{8}$ |
| $\rho_{edge}$ ($cm^{-3}$) | $8.36\text{x}10^{9}$ |

A full understanding of the interplay between these parameters can be seen in Figure 3.15, which plots the FWHM of (002) rocking curve vs. FWHM of (302) rocking curve for various GaN samples [60]. Axes showing edge and screw dislocation densities are also included.

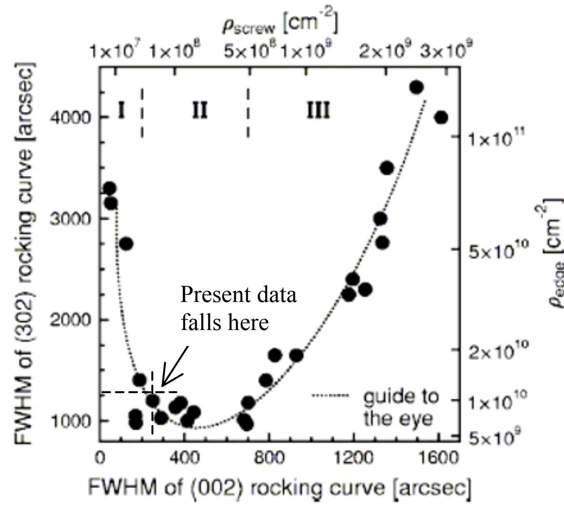


Figure 3.15 Plot of crystal quality characteristics of a series of GaN films [60]

According to this diagram, a given GaN sample should fall within one of 3 regions. Region I is characterized by very low (< 200 arcsec) on-axis linewidths but broad off-axis curves. This indicates a microstructure with a large number of small columns and a correspondingly large edge dislocation density. Such material is crystallographically inferior to that which is found in Region II. Thus, one must be careful not to assume a narrow (002) linewidth value is necessarily indicative of high-quality material.

Region II represents the most ideal crystal structure that can be achieved in heteroepitaxial GaN. It is characterized by an overall minimization of on- and off-axis linewidths and dislocation density. The data and calculations given in Table 3.4 show that the present material falls within this region; therefore our GaN possesses state-of-the-art crystal quality.

Region III corresponds to a regime in which (002) and (302) linewidths increase simultaneously, and thus both $\rho_{edge}$ and $\rho_{screw}$ increase as well. Material within this region is also inferior to that found in Region II.

### *3.5.5 Photoluminescence of nominally undoped GaN*

The optical characteristics of nominally undoped GaN were examined through room-temperature photoluminescence (PL). The excitation source was a Melles Griot Series 74 He-Cd laser rated at a power of 35.0 mW. Band-edge emission for GaN is expected at ~363 nm, and there should be little, if any, deep levels. Thermal broadening of a PL scan is kT/2 [Ref. 64], which for a RT measurement ~ 13 meV.

The PL data from optimized GaN grown on a square substrate is given in Figure 3.16. The peak emission was, as expected, measured at 363 nm. The FWHM of 37 meV is an acceptable value for this material. The absence of any significant deep level emission indicates that there are no optically-active defect-induced states present within the bandgap. The only apparent low energy emission is the shoulder visible at ~371 nm. This is a replica corresponding to logitudinal optical (LO) phonon emission [10], and is commonly seen in photoluminescence measurements of GaN.

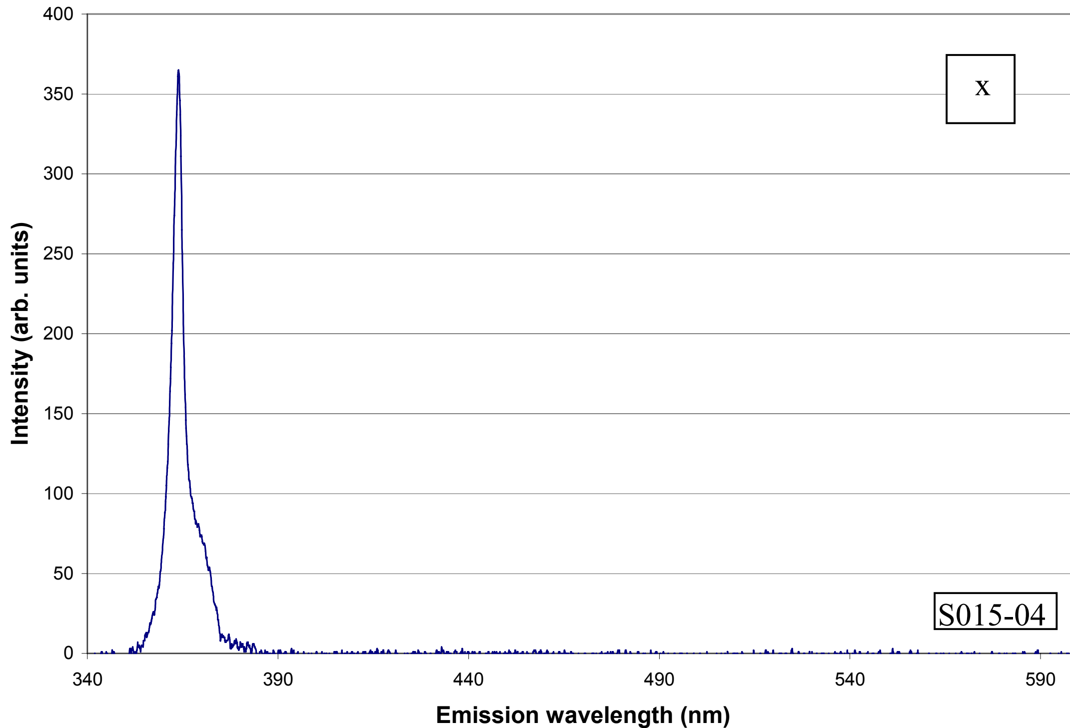


Figure 3.16 Photoluminescence of optimized undoped GaN

*3.5.6 Hall measurement of nominally undoped GaN*

The final characterization test of optimized GaN was the measure of electrical properties by room-temperature Hall measurements using the van der Pauw geometry. Indium dots were used as contacts and the magnetic field was 3.0 kG.

The samples were found to be semi-insulating and thus too resistive to measure. This result was expected, as nominally undoped GaN grown using the TSS-CCS usually demonstrates this behavior [66]. Generally speaking, however, most nominally undoped GaN is measured to have an n-type background carrier concentration. This is often attributed to N vacancies present in the material [15, 66], however, some research groups have questioned the validity of this assumption [67, 68]. Zhang *et. al.* have introduced an

interesting hybrid theory, stating that N vacancies are the dominant source of background carrier only up to threshold value of $n \leq 2x10^{17}$ $cm^{-3}$ [69]. There is currently no clear-cut agreement to the source of the background carrier concentration in GaN; perhaps this question will be answered more definitively as research continues.

## 3.6 Doping of Gallium Nitride

### *3.6.1 N-type doping of GaN*

N-type doping of gallium nitride is fairly straightforward. Silicon is the universally used dopant, as it incorporates easily into the GaN lattice and creates a conveniently shallow donor level within the band (12-20 meV below conduction band) [70]. Generally, no change in growth parameters, aside from the introduction of a silicon source, is necessary for growth of n-type GaN.

A study of the n-type GaN grown by the TSS-CCS reactor was carried out. Silane was used as the silicon source. The concentration of the silane was 10ppm, and it was further diluted before reaching the reactor by the manifold shown in Figure 3.17.

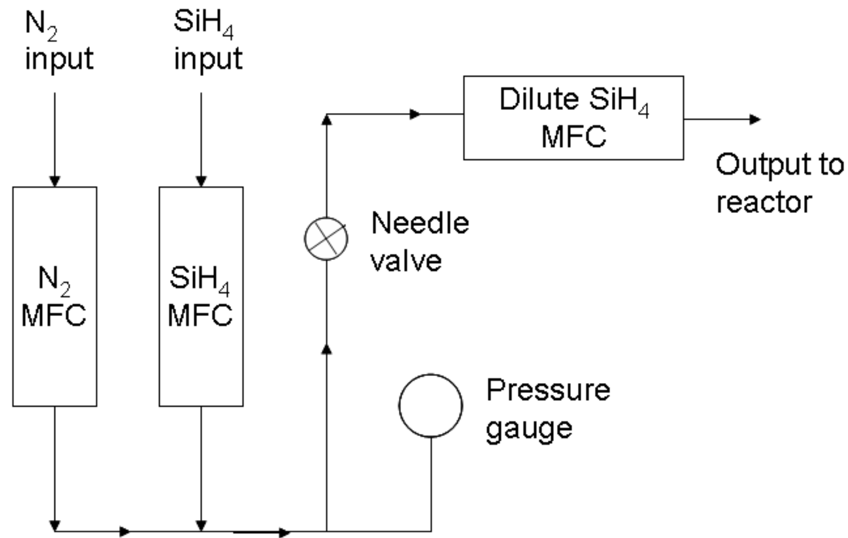


Figure 3.17 Silane dilution manifold

N-type GaN films with a thickness of 1.5 μm were grown using conditions identical to those for nominally undoped GaN (Table 3.3), save for the addition of a given flow of silane into the column V line. Electrical properties of the films were characterized with room-temperature Hall measurements using a square, four-corner geometry. Indium dots were used as contacts and the magnetic field was 3.0 kG. These measurements are summarized in Table 3.5 and plotted in Figure 3.18. Please note that they were taken from the center of square-substrate samples; however, later verification on wedge-substrate samples showed that these properties exhibit no radial dependency.

Table 3.5 Electrical measurements of n-type GaN

| Run number | MFC settings ($N_2/SiH_4$/mix) | $SiH_4$ flow rate (nmol/min) | Resistivity (Ω·cm) | Carrier concentration ($cm^{-3}$) | Mobility ($cm^2$/V·sec) |
|---|---|---|---|---|---|
| S063-04 | 1.0 slm/10sccm/ 10sccm | 0.041 | 0.0418 | $3.56 \times 10^{17}$ | 340 |
| S062-04 | 1.0 slm/10sccm/ 30sccm | 0.123 | 0.0213 | $9.68 \times 10^{17}$ | 241 |
| S064-04 | 1.0 slm/10sccm/ 60sccm | 0.246 | 0.00823 | $2.83 \times 10^{18}$ | 213 |
| S066-04 | 1.0 slm/10sccm/ 100sccm | 0.410 | 0.00559 | $5.00 \times 10^{18}$ | 188 |

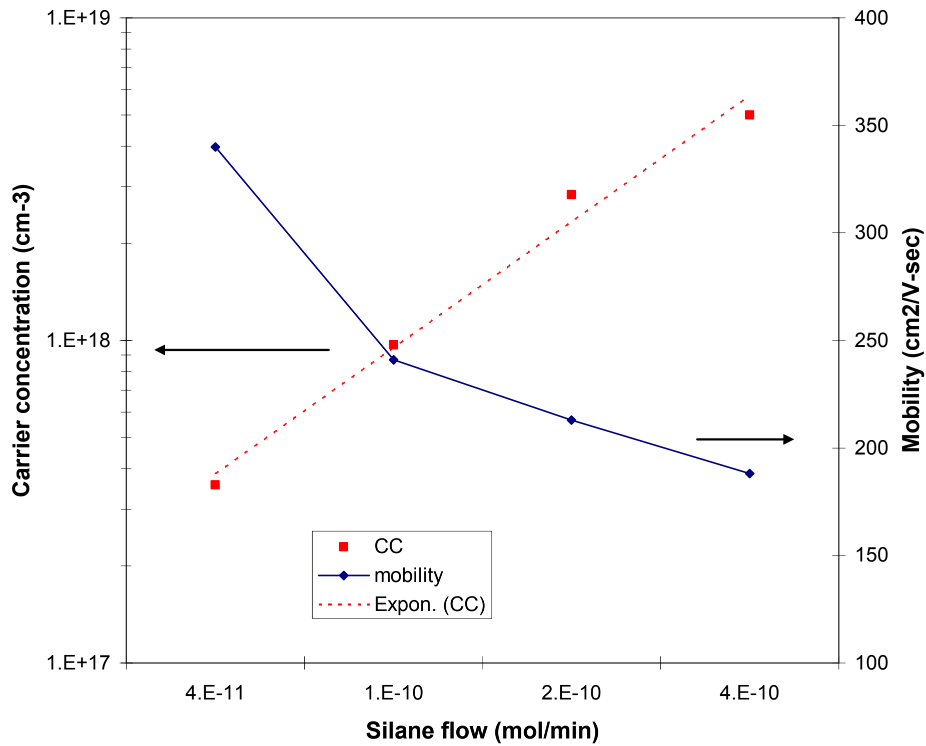


Figure 3.18 Plot of mobility and carrier concentration vs. silane flow for n-type GaN

The carrier concentration relative to the silane flow, as well as the linear relation between the two, is in line with what is expected for this material. The mobility results are also of a reasonable value [71]. The decrease in mobility with increasing carrier concentration is due to an increase in ionized impurity scattering; this phenomenon is common to all semiconductors [72].

Photoluminescence measurements were taken from n-type GaN films. Each of the samples, regardless of carrier concentration, yielded similar results. As an example, the PL spectrum for a film grown on a square substrate with n = $9.68 \times 10^{17}$ $cm^{-3}$ is given in Figure 3.19.

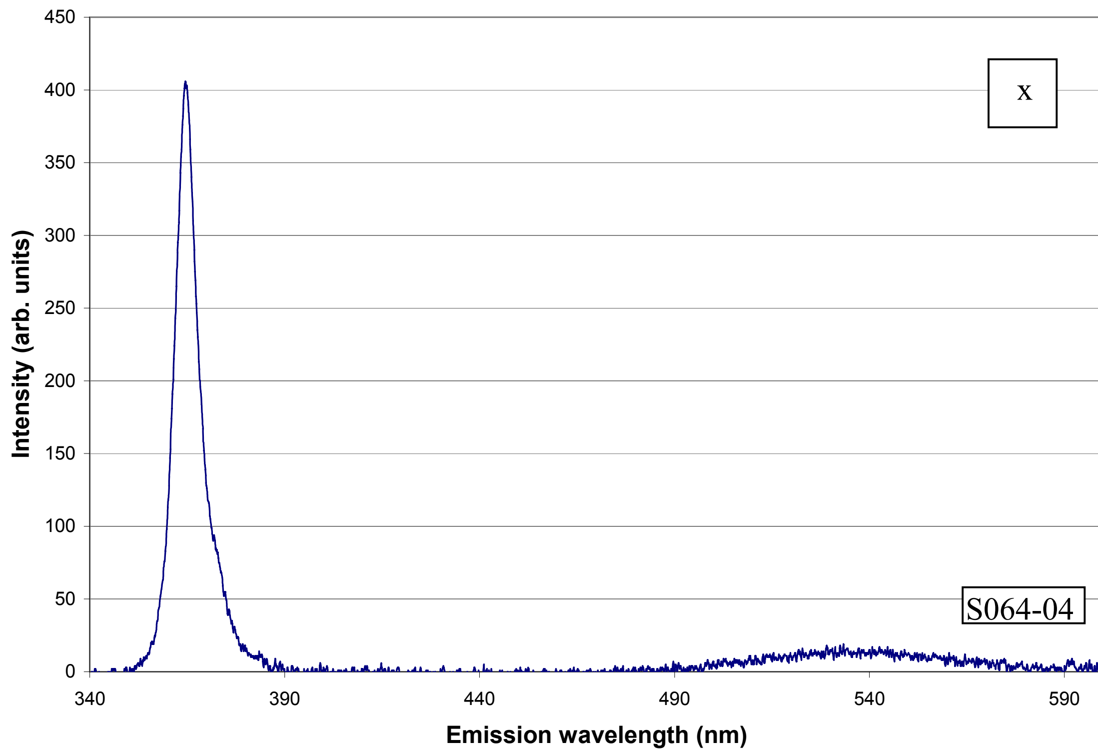


Figure 3.19 Photoluminescence of n-type GaN

The main peak at 363nm is similar to what was seen in the undoped GaN sample. Its FWHM is slightly broader (64 meV) and masks somewhat the phonon replica peak. However, the really interesting bit of this data is the weak, broad emission in the range 500-580 nm. This "yellow luminescence" is a common occurrence in n-type GaN, though its origin is not precisely understood [73]. Some researchers theorize that that some sort of extended defects are involved, such as Ga vacancy/Si-induced defect complexes [74] or N-divacancy complexes [75]. Others suggest it is simply related to the high dislocation density of GaN [76].

The final characterization that was carried out on the n-type samples was atomic force microscopy (AFM). AFM is a technique in which a stylus is dragged across the surface of a sample in order to measure its roughness [77]. This is a critical measurement for the n-type layers because they will serve as the template on which subsequent InGaN-based structures will be grown. The average roughness of the layer should not be greater than the thickness of the quantum wells. This value will vary somewhat, but will tend to be on the order on 30-60 Å.

The data was collected by a Digital Instruments Dimension 3100 microscope operated in tapping mode. The sample was a wedge-shaped piece with a nominal carrier concentration of $5x10^{17}$ $cm^{-3}$ (run S034-06). RMS roughness values were taken at the tip, center, and base over a 5μm x 5μm area. The results are given in Table 3.6.

Table 3.6 RMS roughness values for n-type GaN

| | 5μm x 5μm tip | 5μm x 5μm center | 5μm x 5μm base |
|---|---|---|---|
| RMS roughness (Å) | 2.59 | 2.96 | 3.57 |

The recommended figure-of-merit for roughness of GaN films grown with the TSS-CCS is ~3Å for a 1µm x 1 µm scan [78]. The given AFM measurements show that our optimized samples exhibit reasonable values, and thus can be taken to be acceptably smooth. Also bear in mind that scans done over larger areas (in this case, 5µm x 5µm) will tend to give slightly higher values, so the 3.57Å measurement seen the base is not necessarily out-of-range.

One particular item of interest is the increase in roughness as one moves from tip to base. This 0.98 Å gradient corresponds to an overall increase of 38% across the wafer. The potential significance of this variation will be discussed in Section 4.5.7.

Finally, the AFM measurements yielded some additional data relating to the dislocations in the film. In the 1µm x 1µm image given in Figure 3.20, taken from the center of a square-substrate sample, threading dislocations appear as black dots.

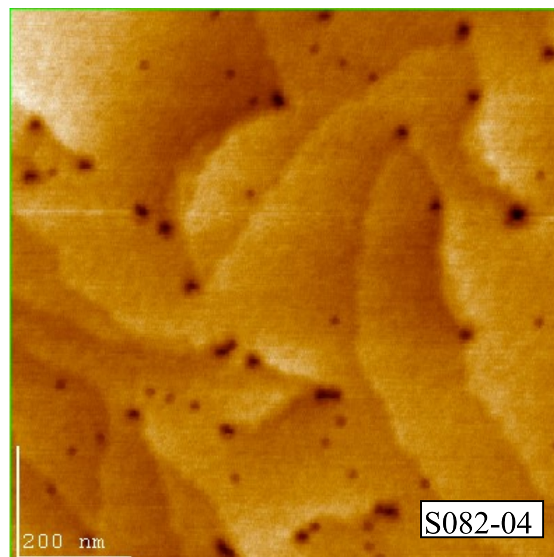

Figure 3.20 1µm x 1µm AFM image of n-type GaN surface

By counting the number of dislocations and extrapolating over a larger area, an estimate of dislocation density can be taken. Fifty-seven dislocations appear in the 1μm x 1μm image, which yields $\rho \approx 5.7 \times 10^9$ $cm^{-3}$. This value is in reasonable agreement with the dislocation density calculated by x-ray diffraction ($\rho \approx 8.5 \times 10^9$ $cm^{-3}$) in Section 3.5.3.

*3.6.2 P-type doping of GaN – Background*

P-type doping of GaN has proven to be significantly more challenging than n-type. In fact, in its early stages, GaN research was very nearly abandoned due to the inability of scientists to achieve reasonable values of p-type conductivity.

There are several reasons for the difficulty of p-type doping in GaN. The first is the lack of dopants which form shallow acceptor levels. Currently, the most popular choice is magnesium, but even its level is fairly deep (160-210 meV from the valence band [70]). This will lead to a low ionization fraction (~ 1%), meaning that a disproportionately large amount of Mg will have to be incorporated into the GaN lattice in order to obtain p-type character.

Also, as discussed in Section 3.5, many GaN films, particularly ones of lower quality, tend to have a high ($n>10^{17}cm^{-3}$) background n-type concentration. In such an instance, these carriers must be fully compensated before p-type character can result. This, combined with the aforementioned low ionization fraction, often leads to instances where only a prohibitively high concentration of Mg can potentially provide p-type doping.

Another complication with p-type doping of GaN is the need for post-growth processing in order to activate the Mg acceptors. This need went unrecognized by early

researchers, who were puzzled by their inability to grow conductive Mg-doped films. This problem, however, began to be resolved in 1989 when Akasaki, *et. al.* came across a vital clue. They discovered that highly resistive ($\rho>10^8\ \Omega\cdot$cm) Mg-doped films exhibited a sudden and severe drop in resistivity ($\rho \sim 35\ \Omega\cdot$cm) after being analyzed in a scanning electron microscope. This allowed for the measurement of $p \approx 2x10^{16}$ cm$^{-3}$ and $\mu \approx 8$ cm$^2$/V·sec. It was concluded that the interaction of the electron beam with the sample is what led to the activation of p-type conduction; thus a low-energy electron beam irradiation (LEEBI) process step was added to the fabrication of p-type GaN [79].

Further progress was made in 1991 when Nakamura, *et. al.* suggested thermal annealing as an alternative to LEEBI [80]. This is an improvement for many reasons. Not only does it circumvent the need for expensive e-beam equipment, but it also activates the entire Mg-doped region simultaneously. LEEBI is limited to activating only those regions within the electron interaction volume.

The mechanism for the passivation of as-grown Mg-doped films was elucidated by studying the activation by thermal annealing of Mg-doped GaN in different ambient atmospheres. It was found that annealing in $N_2$ resulted in the desired conductive material, whereas annealing at identical times and temperatures in $NH_3$ resulted in films with no improvement in conductivity over as-grown films [81]. In fact, it was shown that LEEBI-treated, low-resistivity films actually increased in resistivity (to the as-grown values) upon annealing in $NH_3$ (but not $N_2$). These findings indicated that the presence of atomic hydrogen plays a major role in the passivation of Mg in GaN.

A qualitative explanation is as follows: During the MOCVD growth process, Mg

atoms form a bond with atomic H, thus creating Mg–H complexes which get incorporated into the film. These electrically-inactive complexes do not contribute to p-type doping. During post-growth treatment (either annealing or LEEBI), the Mg–H bond is broken, thus forming an electrically-active Mg center. However, if there is any atomic hydrogen present (such as from the dissociation of $NH_3$), the Mg–H complexes will re-form and the sample will remain highly resistive.

It has been argued that this passivation process during growth is actually beneficial to p-type GaN. Because the incorporated Mg-H complex is not actually acting as an acceptor, the growing crystal does not try to self-compensate through the formation of native defects [82].

### *3.6.3 P-type doping of GaN – Experimental*

P-type gallium nitride was successfully grown using the TSS-CCS. The bake, nitridation and buffer layer conditions were identical to those given in Table 3.3. The bulk growth step differed in three ways:

- TMG flow rate was reduced from 33.1 to 14.2 µmol/min (i.e., growth rate was reduced from 1.5 to 0.3 µm/hr)
- Growth temperature was dropped to either 1020ºC or 975ºC
- Bis(cyclopentadienyl)magnesium ($Cp_2Mg$) was introduced as a magnesium source
- Samples underwent a post-growth anneal (20 min @ 700ºC) in a $N_2$ atmosphere

A slight decrease in TMG flow was employed to correlate with the decrease in growth temperature. This is standard practice in nitride growth, as lower temperature leads to less efficient cracking of $NH_3$ and thus a lower flux of atomic nitrogen [83]. Therefore a lower TMG flux is necessary to keep the V/III ratio fairly constant. Also, the lower TMG flow during this growth step allowed for greater incorporation of Mg, as the Ga and Mg atoms are both competing for the same sites in the GaN structure.

The decrease in temperature was necessary for several reasons. First, it has been shown that lower growth temperature aids in the incorporation of Mg into the lattice [84]. Also, since thise p-type GaN is to be used as a cap layer for InGaN-based devices, lower growth temperatures are better in that they will be less likely to affect the InGaN layers. The temperature sensitivity of InGaN will be discussed in further detail in Chapter 4.

Electrical properties of the films were characterized with room-temperature Hall measurements using the van der Pauw geometry. Indium dots were used as contacts and the magnetic field was 3.0 kG. Film thickness was ~ 1.0 μm. All measurements were taken from the center of square-substrate samples. Results are given in Table 3.7.

Table 3.7 Electrical measurements of p-type GaN

| Run number | Run conditions | Resistivity (Ω·cm) | Mobility ($cm^2$/V·sec) | Carrier concentration ($cm^{-3}$) |
|---|---|---|---|---|
| S067-04 | 514 nmol/min; 1020˚C | 0.640 | 17.3 | $2.22x10^{17}$ |
| S068-06 | 686 nmol/min; 1020˚C | 0.626 | 11.3 | $6.73x10^{17}$ |
| S079-04 | 686 nmol/min; 975˚C | 0.938 | 12.8 | $1.82x10^{17}$ |

These results show that the growth of p-type GaN was successful insofar as a sufficient carrier concentration was achieved. Mobility values are about a factor of 2

lower than normally reported [85]. The best mobility came from the most lightly-doped sample. This is due to decreased ionized-impurity scattering, as discussed in Section 3.6.1. Reduced temperature seems to have a detrimental effect on the carrier concentration, as the sample grown at 975°C had the lowest concentration of holes. This is likely due to the presence of compensating n-type native defects which arose because of the sub-optimal growth temperature. Despite this problem, 975°C will be the p-type growth temperature used for device-structure growth in the following chapters. The slightly lowered hole concentration is far less detrimental to the structure than the loss of InGaN which occurs when trying to cap InGaN quantum wells with high temperature layers.

Photoluminescence measurements were taken from p-type GaN films. In contrast to the PL results for the n-type samples, the measurements taken for p-type material were strongly composition dependent. Figure 3.21 shows the spectrum from a sample with p = $2.22 \times 10^{17}$ $cm^{-3}$, while Figure 3.22 is from a sample with p = $6.73 \times 10^{17}$ $cm^{-3}$. These measurements were taken from the center of square-substrate samples. In each case, plots for both annealed and as-grown material are given.

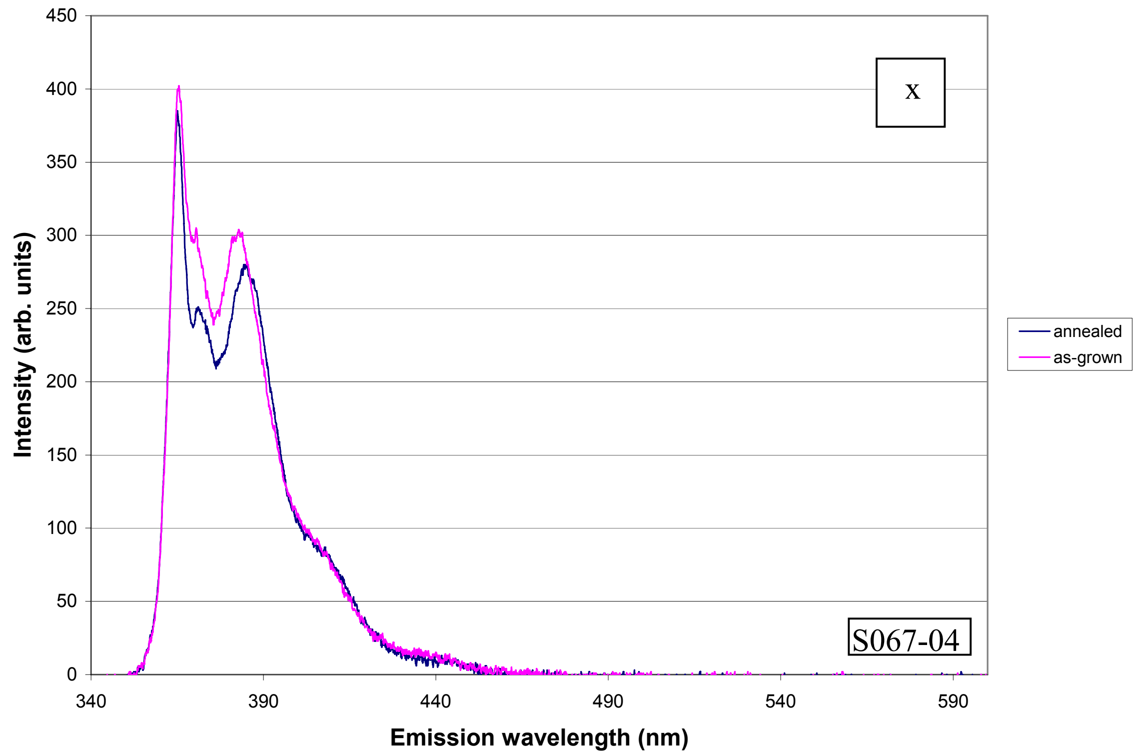


Figure 3.21 PL spectra of annealed and unannealed p-type GaN with p = $2.22 \times 10^{17}$ $cm^{-3}$

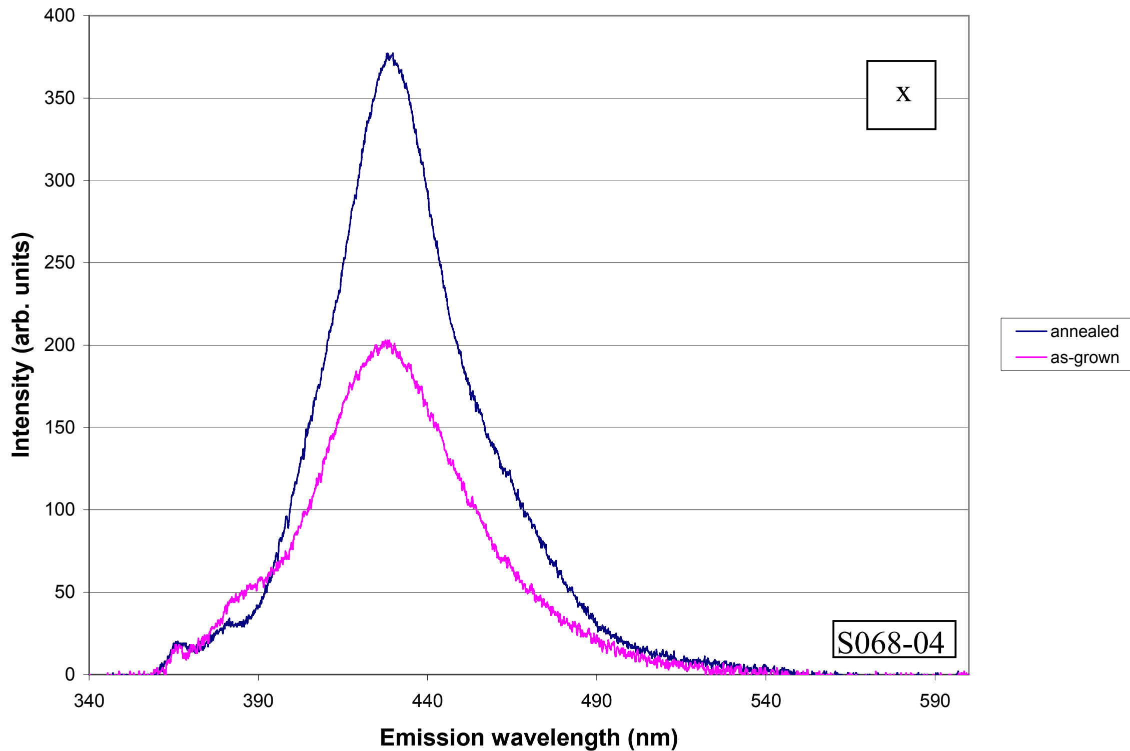


Figure 3.22 PL spectra of annealed and unannealed p-type GaN with p = $6.73 \times 10^{17}$ $cm^{-3}$

The lightly-doped material shows the standard GaN peak at 363 nm as well as an additional peak at ~387 nm. The presence of this additional peak was first discovered by Pankove during a series of ion-implantation studies of GaN [86]. It is simply due to recombination between the conduction band and the intraband Mg level, which, as stated earlier, is located ~200 meV above the valence band (see Figure 3.20). Annealing seems to have little effect on the location and intensity of the peaks; the small variation seen in Figure 3.18 is within the experimental range of error of the PL equipment.

The spectrum for the highly-doped material is altogether different. The undoped GaN peak is no longer present, but there is a broad (FWHM = 343 meV) peak centered at ~420 nm. Annealing has a strong effect on the intensity of the peak, so it can be assumed

that the electrical activity of the acceptors plays a role in their luminescence.

This violet luminescence is commonly seen in p-type GaN [87]. One possible explanation for its presence is recombination between the nitrogen vacancy level (300 meV below the conduction band) and the Mg level. Figure 3.23 gives a simplified diagram of a Mg-doped GaN band structure, depicting the transitions which are thought to be the cause of the luminescence seen in Figures 3.21 and 3.22.

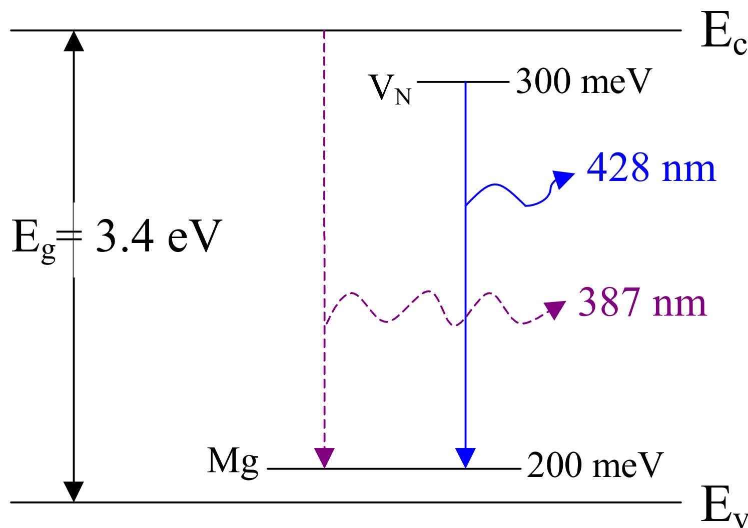


Figure 3.23 Simplified band diagram of Mg-doped GaN, showing optical transitions at 387 nm and 428 nm

The final question, of course, is why the lightly-doped sample emitted at 385 nm while the heavily-doped material emitted at 420 nm. One plausible explanation is that in the lightly-doped sample there was not a high enough concentration of nitrogen vacancies in the material to cause an appreciable number of $V_N$-Mg transitions. However, in the highly-doped sample, the large Mg flux introduced during growth induced the formation of nitrogen vacancies, thus leading to a sample which emits at 428 nm.

### 3.7 References


1. H. Morkoç. *Nitride Semiconductors and Devices.* Chapter 2.1. Springer, Berlin (1999).

2. C.A. Daul. University of Fribourgh. Found online at http://www-chem.unifr.ch/cd/cdaul/CD/cours/geometry/#1.5

3. V. Bougrov, M.E. Levinshtein, S.L. Rumyantsev, and A. Zubrilov. in *Properties of Advanced Semiconductor Materials GaN, AlN, InN, BN, SiC, SiG,* p1. M.E. Levinshtein, S.L. Rumyantsev, and M.S. Shur, eds. John Wiley & Sons, Inc., New York (2001).

4. J. Wu, H. Yaguchi, K. Onabe, Y. Shiraki, and R. Ito. "Metalorganic vapor phase epitaxy Growth of High Quality Cubic GaN on GaAs (100) Substrates." *Jpn. J. Appl. Phys.* **37**, 1440 (1998).

5. Z.H. Feng, H. Yang, Y. Fu, Y.P. Sun, X.M. Shen, and Y.T. Wang. "Optimization of cubic GaN growth by metalorganic chemical vapor deposition based on residual strain relaxation." *Appl. Phys. Lett.* **82**, 206 (2002).

6. K. Amimer, A. Georgakilas, K. Tsagaraki, M Androulidaki, D. Cengher, L. Toth, and B. Pecz. "Single crystal hexagonal and cubic GaN growth directly on vicinal (001) GaAs substrates by molecular-beam epitaxy." *Appl. Phys. Lett.* **76**, 2580 (2000).

7. A. Tabata, A.P. Lima, J.R. Leite, V. Lemos, D. Schikora, B. Schöttker, U. Köhler, D.J. As, and K. Lischka. "Micro-Raman analysis of cubic GaN layers grown by MBE on (001) GaAs substrate." *Semicond. Sci. Technol.* **14**, 318 (1999).

8. E.T. Yu. "Spontaneous and piezoelectric polarization in nitride heterostructures." in *III-V Nitride Semiconductors: Applications and Devices,* Ch. 4. E.T. Yu and O. Manasreh, eds. Taylor & Francis, New York (2003).

9. H. Okumura, K. Ohta, G. Feuillet, K. Balakrishnan, S. Chichibu, H. Hamaguchi, P. Hacke, and S. Yoshida. "Growth and characterization of cubic GaN." *J. Crys. Gr.* **178**, 113 (1997).

10. S. Strite and H. Morkoç. "GaN, AlN, and InN: a review." *J. Vac. Sci. Tech. B* **10**, 1237 (1992).

11. Nakadaira and H. Tanaka. "Metalorganic Vapor-Phase Epitaxial Growth and Characterization of Cubic $Al_xGa_{1-x}N$ Alloy." *Jpn. J. Appl. Phys.* **37**, 1449 (1998).

12. J.R. Müllhäuser, B. Jenichen, M. Wassermeier, O. Brandt, and K.H. Ploog. "Characterization of zinc blende $In_xGa_{1-x}N$ grown by radio frequency plasma assisted molecular beam epitaxy on GaAs (001)." *Appl. Phys. Lett.* **71**, 909 (1997).

13. M. Katsikini, E.C. Paloura, and T.D. Moustakas. "Application of near-edge x-ray absorption fine structure for the identification of hexagonal and cubic polytypes in epitaxial GaN. *Appl. Phys. Lett.* **69**, 4206 (1996).

14. D. Xu, H.Yang, S.M. Zhang, L.X. Zheng, D.G. Zhao, S.F. Li, Y.T. Wang, R.H. Wu. "Investigation into the origin of wurtzite domains in thick cubic GaN using reactive ion etching." *Thin Solid Films* **372**, 25 (1999).

15. H.P. Maruska and J.J. Tietjen. "The Preperation and properties of vapour-deposited single-crystal-line GaN." *Appl. Phys. Lett.* **15**, 327 (1969).

16. M. Ohring. *The Materials Science of Thin Films*, Ch. 7.5.4. Academic Press, Inc., San Diego (1992).

17. T.D. Moustakas. "Growth of wide-bandgap nitride semiconductors by MBE." in *Gallium-Nitride-based Technologies,* p. 1. M. Osiński, ed. SPIE Optical Engineering Press, Bellingham, WA (2002).

18. S. Nakamura, S. Pearton, and G. Fasol. *The Blue Laser Diode: The Complete Story*, Chapter 3.2.2. Springer, Berlin (2000).

19. H. Amano, N. Sawaki, I. Kasaki, and Y. Toyoda. "Metalorganic vapor phase epitaxial growth of a high quality GaN film using an AlN buffer layer." *Appl. Phys. Lett.* **48**, 353 (1986).

20. S. Nakamura. "GaN growth using GaN buffer layer." *Jpn. J. Appl. Phys.* **30**, L1705 (1991).

21. S. Fischer, C. Wetzel, W.L. Hansen, E.D. Bourret-Courchesne, B.K. Meyer, and E.E. Haller. "Properties of GaN grown at high rates on sapphire and on 6H-SiC." *Appl. Phys. Lett.* **69**, 2716 (1996).

22. L. Lu, H. Yan, C.L. Yang, M. Xie, Z. Wang, J. Wang, and W. Ge. "Study of GaN thin films grown on vicinal SiC (0001) substrates by molecular beam epitaxy." Semicond. Sci. Tech. **17**, 957 (2002).

23. P. Rajagopal, T. Gehrke, J.C. Roberts, J.D. Brown, T.W. Weeks, E. Piner, and K, Linthicum. "Large-area, device quality GaN on Si using a novel transition layer scheme." *Materials Research Society Symposium Proceedings Vol. 743: GaN and Related Alloys—2002*, p. L.1.2.1 (2003).

24. X. Gu, M.A. Reshchikov, L. He, A. Teke, F. Yun, D.K. Johnstone, B. Nemeth, J. Nause, and H. Morkoç. "Epitaxy of highly optical efficient GaN on O and Zn face ZnO." *Materials Research Society Symposium Proceedings Vol. 798: GaN and Related Alloys—2003*, p. Y.9.1.1 (2004).

25. C. J. Sun, J. W. Yang, Q. Chen, M. Asif Khan , T. George, P. Chang-Chien , S. Mahajan. "Deposition of high quality wurtzite GaN films over cubic (111) $MgAl_2O_4$ substrates using low pressure metalorganic chemical vapor deposition." *Appl. Phys. Lett*. 68, 1129 (1996).

26. K. Doverspike, L.B. Rowland, D.K. Gaskill, and J.A. Freitas, Jr. "The effect of GaN and AlN buffer layers on GaN film properties grown on both c-plane and a-plane sapphire." *J. Elec Mat.* **24**, 269 (1995).

27. D. Doppalapudi, E. Iliopoulos, S.N. Basu, and T.D. Moustakas. "Epitaxial growth of gallium nitride thin films on A-plane sapphire by molecular beam epitaxy." *J. Appl. Phys.* **85**, 3582 (1999).

28. S. Tripathy, R. K. Soni, H. Asahi, K. Iwata, R. Kuroiwa, K. Asami, and S. Gonda. "Optical properties of GaN layers grown on *C*-, *A*-, *R*-, and *M*-plane sapphire substrates by gas source molecular beam epitaxy." *J. Appl. Phys.* **85**, 8386 (1999).

29. K. Hess, Thomas Swan Scientific. Personal communication. (2004).

30. M. Gautier, J.P. Durand, L. Pham Van, M.J. Guittet. "Modifications of α-$Al_2O_3$(0001) surfaces induced by thermal treatments or ion bombardment." *Surf. Sci.* **250**, 71 (1991).

31. G. Renaud, B. Vilette, I. Vilfan, A. Bourret. "Atomic Structure of the α-$Al_2O_3$(0001) ($\sqrt{31}$ x $\sqrt{31}$)R ± 9° reconstruction" *Phys. Rev. Lett.* **73**, 1825 (1994).

32. J. Guo. D.E. Ellis, D.J. Lam. "Electronic structure and energetics of sapphire (0001) and ($1\bar{1}02$) surfaces." *Phys. Rev. B* **45**, 13647 (1992).

33. K. Uchida, A. Watanabe, F. Yano, M. Kouguchi, T. Tanaka, and S. Minagawa. "Nitridation process of sapphire substarte surface and its effect on the growth of GaN." *J. Appl. Phys.* **79**, 3487 (1996).

34. A. Yamamoto, M. Tsujino, M. Ohkubo, and A. Hashimoto. "Nitridation effects of substrate surface on the metalorganic chemical vapor deposition growth of InN on Si and α-$Al_2O_3$ substrates. *J. Crys. Gr.* **137**, 415 (1994).

35. X.H. Wu, D. Kapolnek, E.J. Tarsa, B. Heying, S. Keller, B.P. Keller, U.K. Mishra, S.P. DenBaars, and J.S. Speck. "Nucleation layer evolution in metal-organic chemical vapor deposition grown GaN." *Appl. Phys. Lett.* **68**, 1371 (1996).

36. F.A. Ponce. "Defects and interfaces in GaN epitaxy." *MRS Bull.* **22** (2), 51 (1997).

37. R. Chierchia, T. Böttcher, H. Heinke, S. Einfeldt, S. Figge, and D. Hommel. "Microstructure of heteroepitaxial GaN revealed by x-ray diffraction." *J. Appl. Phys.* **93**, 8918 (2003).

38. T. Metzger, R. Hopler, E. Born, O. Ambacher, M. Stutzmann, R. Stömmer, M. Schuster, H. Göbel, S. Christiansen, M. Albrecht, and H.P. Strunk. "Defect structure of epitaxial GaN films determined by transmission electron microscopy and triple-axis x-ray diffractometry." *Phil. Mag. A* **77**, 1013 (1998).

39. R.E. Reed-Hill and R. Abbaschian. *Physical Metallurgy Principles*, Ch. 6.2. PWS Publishing Company, Boston (1994).

40. X.H. Wu, P. Fini, E.J. Tarsa, B. Heying, S. Keller, U.K. Mishra, S.P. DenBaars, and J.S. Speck. "Dislocation generation in GaN heteroepitaxy." *J. Crys. Gr.* **189/190**, 231 (1998).

41. A.H. Herzog, D.L. Keune, and M.G. Craford. "High-efficiency Zn-diffused electroluminescent diodes." *J. Appl. Phys.* **43**, 600 (1972).

42. W.A. Brantley, O.G. Lorimor, P.D. Dapkus, S.E. Haszko, and R.H. Saul. "Effect of dislocations on green electroluminescence efficiency in GaP grown by liquid phase epitaxy." *J. Appl. Phys.* **46**, 2629 (1975).

43. S.D. Lester, F.A. Ponce, M.G. Craford, and D.A. Steigerwald. "High dislocation densities in high efficiency GaN-based light-emitting diodes." *Appl. Phys. Lett.* **66**, 1249 (1995).

44. *CRC Handbook of Chemistry and Physics*, 78$^{th}$ edition. D.R. Lide, editor-in-chief. CRC Press, Boca Raton/New York (1997-1998).

45. S. Kurtin, T.C. McGill, and C.A. Mead. "Fundamental Transition in the Electronic Nature of Solids." *Phys. Rev. Lett.* **22**, 1433 (1969).

46. F.A. Ponce. "Microstructure of epitaxial III-V nitride thin films." *Optoelectronic Properties of Semiconductors and Superlattices, Vol. 2: GaN and Related Materials*. S.J. Pearton, ed. Gordon and Breach Science Publishers, Amsterdam (1999).

47. J.S. Foresi and T.D. Moustakis. "Metal contacts to gallium nitride." *Appl. Phys. Lett.* **62**, 2859 (1993).

48. E.S. Hellman. "The polarity of GaN: a critical review." *MRS Internet J. Nitride Semicond. Res.* **3**, 11 (1998).

49. M. Sumiya and S. Fuke. "Review of polarity determination and control of GaN." *MRS Internet J. Nitride Semicond. Res.* **9**, 1 (2004).

50. F.A. Ponce, D.P. Bour, W.T. Young, M. Saunders, J.W. Steeds. "Determination of lattice polarity for growth of GaN bulk single crystals and epitaxial layers." *Appl. Phys. Lett.* **69**, 337 (1996).

51. B. Daudin, J.L. Rouvière, M. Arlery. "Polarity determination of GaN films by ion channeling and convergent beam electron diffraction." *Appl. Phys. Lett.* **69**, 2480 (1996).

52. J.L. Weyher, S. Müller, I.Grzegory, and S. Porowski. "Chemical polishing of bulk and epitaxial GaN." *J. Crys. Gr.* **182**, 17 (1997).

53. F. Bernardini, V.Fiorentini, and D. Vanderbilt. "Spontaneous polarization and piezoelectric constants of III-V nitrides." *Phys. Rev. B* **56**, R10024 (1997).

54. R. Swanepoel. "Determination of the thickness and optical constants of amorphous silicon." *J. Phys. E: Sci. Instrum.* **16**, 1214 (1983).

55. G. Yu, G. Wang, H. Ishikawa, M. Umeno, T. Soga, T. Egawa, J. Watanabe, T. Jimbo. "Opitical properties of wurtzite structure GaN on sapphire around fundamental absorption edge (0.78-4.77 eV) by spectroscopic ellipsometry and the optiocal transmission method." *Appl. Phys. Lett.* **70,** 3209 (1997).

56. M.E. Twigg, D.D. Koleske, A.E. Wickenden, R.L. Henry, and S.C. Binari. "Correlation between nucleation layer structure, dislocation density, and electrical resistivity for GaN films grown on a-plane sapphire by metalorganic chemical vapor deposition." *Appl. Phys. Lett.* **79,** 4322 (2001).

57. J. Kozlowski, R. Paszkiewicz, and M. Tlaczala. "Structure characterization of (Al, Ga)N epitaxial layers by means of x-ray diffractometry." *Phys. Stat. Sol. (b)* **228**, 415 (2001).

58. H. Heinke, V. Kirchner, S. Einfeldt, and D. Hommel. "Analysis of the defect structure of epitaxial GaN." *Phys. Stat. Sol. (a)* **176**, 391 (1999).

59. G.K. Williamson and W.H. Hall. "X-ray line broadening from filed aluminum or wolfram." *Acta Metall.* **1**, 22 (1953).

60. H. Heinke, V. Kirchner, S. Einfeldt, and D. Hommel. "X-ray diffraction analysis of the defect structure in epitaxial GaN." *Appl. Phys. Lett.* **77**, 2145 (2000).

61. P. Gay, P.B. Hirsch, and A. Kelly. "The estimation of dislocation densities in metals from x-ray data." *Acta Metall.* **1**, 315 (1953).

62. D.R. Askeland. *The Science and Engineering of Materials*, Ch. 4.2. PWS Publishing Co., Boston (1994).

63. P.F. Fewster. "A high-resolution multiple-crystal multiple-reflection diffractometer." *J. Appl. Crystallogr.* **22**, 64 (1989).

64. D.K. Schroeder. *Semiconductor Material and Device Characterization*, Ch. 9.10. John Wiley & Sons, Inc., New York (1998).

65. E.J. Thrush, Thomas Swan Scientific. Private communication. (2004).

66. J.I. Pankove and J.E. Berkeyheiser. "Properties of Zn-doped GaN. II. Photoconductivity." *J. Appl. Phys.* **45**, 3892 (1974).

67. M.A. Khan, J.N. Kuznia, J.M. Van Hove, D.T. Olson, S. Krishnankutty, and R.M. Kolbas. "Growth of high optical and electrical quality GaN layers using low-pressure metalorganic chemical vapor deposition." *Appl. Phys. Lett.* **58**, 526 (1991).

68. T. Sasaki and T. Matsuoka. "Analysis of two-step-growth conditions for GaN on an AlN buffer layer." *J. Appl. Phys.* **77**, 192 (1995).

69. G.Y. Zhang, Y.Z. Tong, Z.J. Yang, S.X. Jin, J. Li, and Z.Z. Gan. "Relationship of background carrier concentration and defects is GaN grown by metalorganic vapor phase epitaxy." *Appl. Phys. Lett.* **71**, 3376 (1997).

70. M. E. Levinshtein, S. L. Rumyantsev, and M. S. Shur, Editors. *Properties of Advanced Semiconductor Materials: GaN, AlN, InN, BN, SiC, and SiGe.* John Wiley and Sons, New York (2001).

71. S. Nakamura, S. Pearton, and G. Fasol. *The Blue Laser Diode: The Complete Story*, Ch. 6.3. Springer, Berlin (2000).

72. B.G. Streetman and S. Banerjee. *Solid State Electronic Devices*, Ch. 3.4. Prentice Hall, Upper Saddle River, NJ (2000).

73. C. Kim, S, Kim, Y. Choi, and S.-J. Leem. "Correlation between the type of threading dislocations and photoluminescence characteristics at different doping concentrations of Si in GaN films." *J. Appl. Phys.* **92**, 6343 (2002).

74. I.-H. Lee, I.-H. Choi, C.R. Lee, and S.K. Noh. "Evolution of stress relaxation and yellow luminescence in GaN/sapphire by Si incorporation." *Appl. Phys. Lett.* **71**, 1359 (1997).

75. A.E. Yunovich. “A model of the ‘yellow band’ defect complex in GaN.” *Electrochemical Society Proceedings Vol. 97-34: III-V Nitride Materials and Processes.* C.R. Abernathy, W.D. Brown, D.N. Buckley, J.P. Dismukes, M. Kamp, T.D. Moustakas, S.J. Pearton, F. Ren, eds. The Electrochemical Society, Inc. Pennington, NJ (1998).

76. F.A. Ponce, D.P. Bour, W. Götz, and P.J. Wright. “Spatial distribution of the luminescence in GaN thin films.” *Appl. Phys. Lett.* **68**, 57 (1996).
77. An AFM tutorial can be found online at http://www.ncsu.edu/aif/SPM/AFM%20Tutorial.pdf

78. A. Boyd, Thomas Swan Scientific. Private communication. (2004).

79. H. Amano, M. Kito, K. Hiramatsu, and I. Akasaki. “P-type conduction in Mg-doped GaN treated with low-energy electron beam irradiation (LEEBI).” *Jpn. J. Appl. Phys.* **28**, L2112 (1989).

80. S. Nakamura, T. Mukai, M. Senoh, and N. Iwasa. “Thermal annealing effects on p-type Mg-doped GaN films.” *Jpn. J. Appl. Phys.* **31**, L139 (1992).

81. S. Nakamura, N. Iwasa, M. Senoh, and T. Mukai. “Hole compensation mechanism of p-type GaN films.” *Jpn. J. Appl. Phys.* **31**, 1258 (1992).

82. N.M. Johnson, A.V. Nurmikko, and S.P. DenBaars. “Blue diode lasers.” *Phys. Today*. **53** (10), 31 (2000).

83. S.M. Bedair. “Indium-based nitride compounds.” *Semiconductors and Semimetals, Vol. 50*, Ch. 6. Academic Press, Inc. (1997).

84. R.D. Dupuis. “Epitaxial growth of III-V nitride semiconductors by metalorganic chemical vapor deposition.” *J. Crys. Gr.* **178**, 56 (1997).

85. S. Fujita, M. Funato, D.-C. Park, Y. Ikenaga, S. Fujita. “Electrical characterization of MOVPE-grown p-type GaN:Mg against annealing temperature.” *MRS Internet J. Nitride Semicond. Res.* 4S1, G6.31 (1999).

86. J.I. Pankove and J.A. Hutchby. “Photoluminescence of ion-implanted GaN.” *J. Appl. Phys.* **47**, 5387 (1976).

87. W. Götz, N.M. Johnson, J. Walker, D.P. Bour, and R.A. Street. “Activation of acceptors in Mg-doped GaN grown by metalorganic chemical vapor deposition.” *Appl. Phys. Lett.* **68**, 667 (1996).

# 4.0 Indium Gallium Nitride

## 4.1 Structure of Active Layers

As mentioned in Chapter 1, the active layer in a nitride-based visible LED will be composed of the ternary alloy InGaN. However, bulk layers of InGaN are very inefficient for photon emission, as the charge carriers are free to diffuse to non-radiative recombination centers. Thus, an active layer structure in which these carriers can be confined to a small region would be beneficial. One such way to achieve such carrier confinement is with a double heterostructure.

A double heterostructure is composed of a layer of lower bandgap material bound on both sides by layers of larger bandgap material [1]. The carriers migrate to the energetically favorable positions inside the wells, where they are confined until recombination. Figure 4.1 depicts a typical double heterostructure commonly used in nitride LED's, in which the InGaN wells are bound on both sides by GaN barriers.

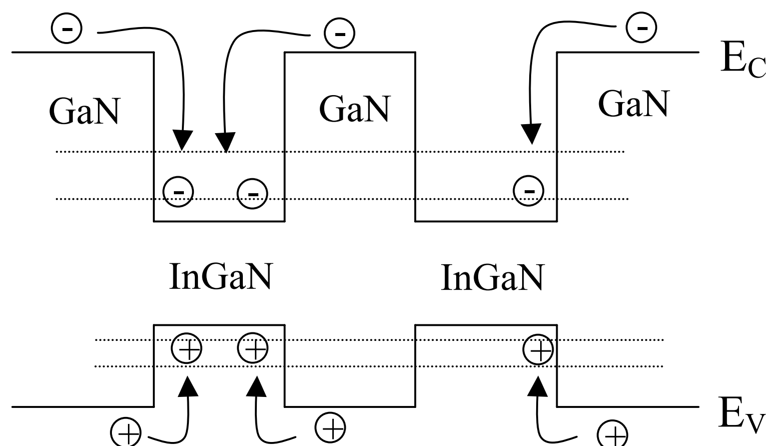


Figure 4.1 InGaN/GaN double heterostructure

Once inside the wells, carriers act in accordance with the "particle-in-a-box" concept of quantum theory, which means that a series of discrete energy states are formed within each well (see the dotted lines in the figure), as opposed to the energy continuum seen in a bulk layer. Because of the presence of these energy quanta, double heterostructures are commonly referred to as "quantum" wells. These quantized energy states within the well lead to an effective increase in the bandgap, and thus a blueshift of the emission energy.

A simplified expression for the allowed energy levels of a particle in a box is given by [2]:

$$E_n = \frac{n^2 \pi^2 \hbar^2}{2mL^2} \quad \text{(Eq. 4.1)}$$

where $n$ = any positive integer, $m$ = the mass of the confined particle and $L$ = thickness of the box. This expression points out the inverse relationship between the width of the well and the effective bandgap of a quantum well structure. This phenomenon is known as the quantum size effect [3] and must be taken into account when analyzing the emission wavelength of an LED whose active region is composed of quantum wells. Extensive modeling of the quantum size effect is given in Chapter 5.

## 4.2 Indium Nitride

A full understanding of the ternary InGaN material system begins with a discussion of the binary compound InN. In comparison to its fellow III-nitrides (AlN and GaN), indium nitride is by far the least studied and least understood of the three. The primary reason for this is the difficulties inherent in synthesizing this compound. Hovel

and Cuomo grew the first reported films of InN in 1971 [4], but since that time there have been relatively few successful efforts in this area.

One of the often-cited reasons for this difficulty is the large disparity in atomic radii between indium and nitrogen [5]. Another, perhaps more detrimental, factor is the extremely poor thermal stability of this material. Whereas most III-V materials can be readily grown by CVD processes, InN has a N equilibrium vapor pressure of $10^2$-$10^4$ torr at typical CVD growth temperatures (see Figure 4.2). This means that any InN deposited on a substrate at these temperatures will likely dissociate immediately, leaving behind In metal which will subsequently evaporate.

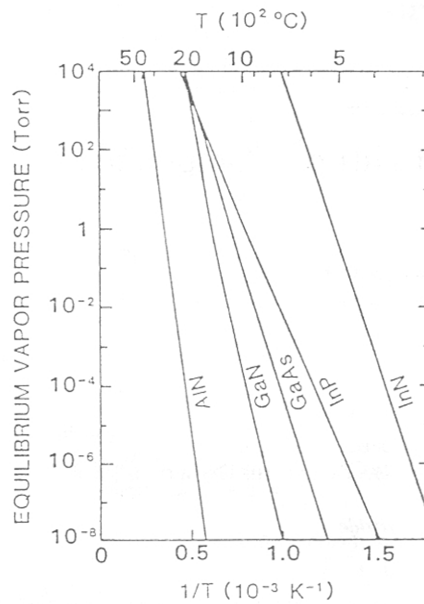

Figure 4.2 Equilibrium vapor pressures of common compound semiconductors [6]

One of the consequences of the lack of quality InN is the presence of some uncertainty regarding one of the most fundamental properties of the material: the bandgap. Early experimental [7] and theoretical [8] studies of InN reported a bandgap of

~1.9 eV, and this value was widely accepted for many years. However, recent advances in InN growth have led to synthesis of higher-quality material, and characterization of these samples has raised some questions concerning the value of the fundamental bandgap of InN.

The improved-quality InN was grown by both plasma-assisted molecular-beam epitaxy (PAMBE) [9] and metal-organic molecular beam epitaxy (MOMBE) [10]. Photoluminescence measurements of this material indicate a bandgap value of 0.7 – 0.9 eV [11], nearly 1 eV less than previously reported. Confirmation of this lower value has come through optical absorption and photomodulated reflectance measurements [12]. In light of this evidence, the majority of the III-nitride community, including the present author, has come to accept the value of $E_g^{InN} \approx 0.7$ eV.

## 4.3 Growth of the Ternary Alloy InGaN

### *4.3.1 Introduction to InGaN*

Due in part to the difficulties in its synthesis, InN itself has thusfar attracted little attention outside of the laboratory. However, InN can be readily alloyed with GaN, and its subsequent ternary compound, InGaN, has revolutionized the optoelectronics industry. InGaN has found widespread use in the active regions of violet to green LED's, as well as solid-state blue lasers [13]. InGaN may also potentially be used for the fabrication of monolithic white LED's (see Chapter 1), a possibility which the present work is exploring in detail.

InGaN is most often grown by the same techniques used to grow GaN: MOCVD and MBE. However, the growth of InGaN is significantly more difficult than that of

GaN. The many challenges and complications which arise when attempting to synthesize this alloy will be discussed in the following sections.

*4.3.2 InGaN growth model*

The growth of InGaN can best be understood by examining the model presented by Bedair *et. al.* [14,15], which describes the competitive processes which occur during the growth process. This model defines the following three quantities, representing the three possible reaction pathways for an In atom arriving at a growing film surface:

1. In incorporation in the solid ternary alloy, $F_s$ (atoms/cm$^2$·sec)
2. In atom desorption from the growth surface, $F_d$ (atoms/cm$^2$·sec)
3. In incorporated as In metal droplets, $F_m$ (atoms/cm$^2$·sec)

The successful growth of InGaN requires the maximization of $F_s$ and the minimization of $F_d$ and $F_m$. For an incoming indium flux, $F_{in}$, one can present the mass balance equation:

$$F_{in} = F_s + F_d + F_m \qquad \text{(Eq. 4.1)}$$

This is shown schematically in Figure 4.3.

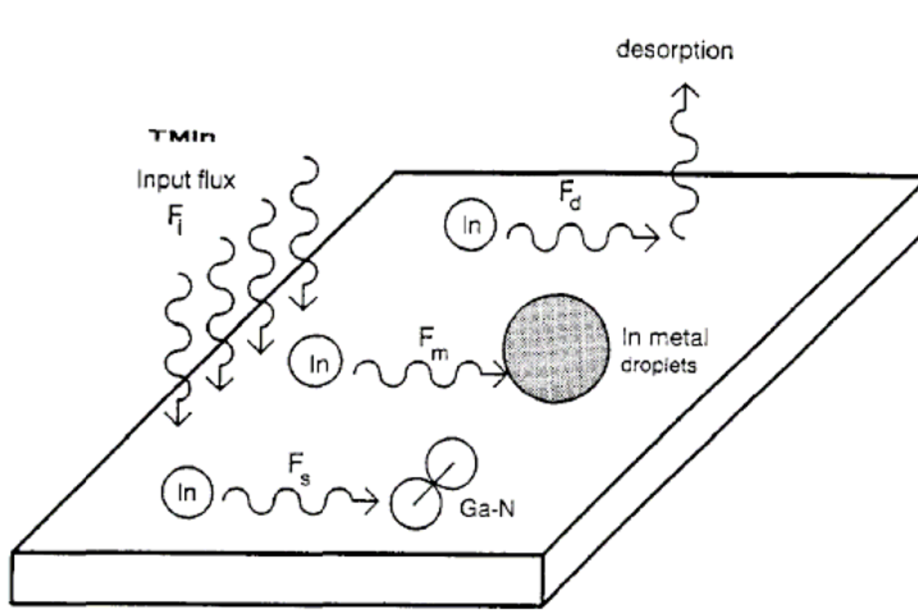


Figure 4.3 Reaction pathways for the deposition of In-based nitride compounds [15]

The Bedair model relates $F_d$ to the residence lifetime, τ, of the In adatom to the growing film surface. This lifetime can be expressed as:

$$\tau = \tau_0 e^{+E_d/kT} \qquad \text{(Eq. 4.2)}$$

where $E_d$ is the activation energy for desorption, T is the growth temperature, and $\tau_0$ is fixed for the given system.

Equation 4.2 gives rise to the following proportionality:

$$F_d \propto e^{-E_d/kT} \qquad \text{(Eq. 4.3)}$$

This expression indicates that higher growth temperatures lead to an exponential increase in the rate of indium desorption, $F_d$. This is in agreement with published experimental data [15,16], which reports that the In content of an InGaN film (i.e., $F_s$) is inversely proportional to growth temperature. This strong temperature dependence is a consequence to the aforementioned weakness of the In—N bond; as temperature

increases so does the likelihood of this bond breaking and the indium desorbing (i.e., an increase in $F_d$).

The values of $E_d$ and $\tau$ have not been experimentally determined for the III-nitride material system. However, for the sake of comparison, one may look to the values obtained for the InGaAs system. Arthur determined that the lifetime of a Ga adatom on a GaAs surface at 600˚C is approximately an order of magnitude higher than that of an In adatom [17]. For this reason, increasing the In/Ga ratio in an attempt to increase $F_s$ has somewhat limited effectiveness, particularly at high growth temperatures. Experimental evidence has shown this to be the case [16].

The Bedair model has thus far demonstrated that the most efficient way to increase $F_s$ is by increasing $F_{in}$ and reducing growth temperature. However, these conditions are also conducive to an increase in $F_m$. The low growth temperature (and hence inefficient cracking of $NH_3$) reduces the amount of nitrogen available for bonding. This lack of nitrogen, combined with a high density of In adatoms, will lead to the formation of small droplets of In metal. These droplets may then act as sinks for incoming In atoms, thus further reducing $F_s$.

Of course, this indium droplet issue becomes much more prevalent as the attempted In content of the alloy increases, thus making the growth of InGaN progressively more difficult as the target bandgap is lowered. This is one of the reasons why the LED industry is struggling in manufacture of long (>525 nm) wavelength InGaN-based devices.

### 4.4 Lattice Mismatch in InGaN

Another major issue related to the growth of InGaN is the very large (11%) lattice mismatch between InN and GaN ($a_{GaN}$ = 3.189Å, $a_{InN}$ = 3.544Å) [13]. This mismatch affects the material in two primary ways: strain and compositional fluctuations. Each of these will be discussed in greater detail in the following sections.

#### *4.4.1 Strain in InGaN*

The amount of strain present in an InGaN quantum well with GaN barriers can be approximated as [18]:

$$\varepsilon = -0.1065x - 0.0003 \qquad \text{(Eq. 4.4)}$$

where x is the In content of the alloy. Using this expression, one can see that the strain in this type of structure can be remarkably high: -1.1% for mere x = 0.10, an enormous -3.2% if one manages to grow x = 0.30 material.

One of the consequences of the high strain in this material system is the presence of a severe piezoelectric polarization field. Piezoelectricity is defined as the ability of a material to convert mechanical stress (strain) into an electric field [19]. In order for this to occur, the material in question must be anisotropic and electrically poled. Wurtzite GaN meets both of these criteria, as it possesses an anisotropic crystal structure and is polar along (0001), i.e., the growth direction [20].

The high strain values in the InGaN/GaN structure will thus induce sizeable piezoelectric fields in the (0001) direction, perpendicular to the quantum well structure. These fields will lead to the bending of the conduction and valence bands of the wells, as seen in Figure 4.4.

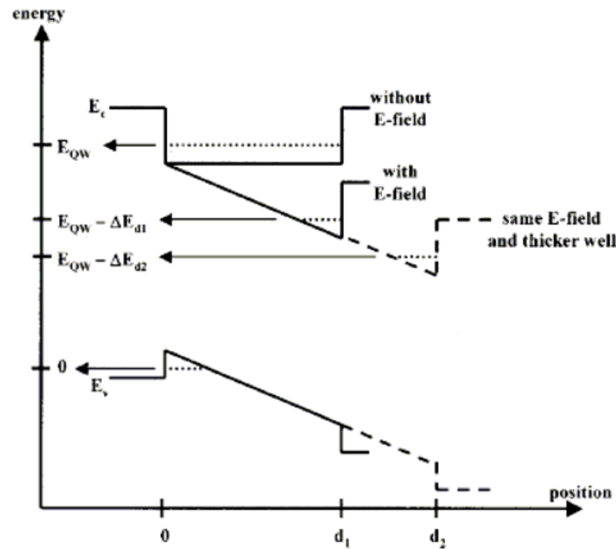


Figure 4.4 Band-bending in a double heterostructure [21]

When piezoelectric band-bending takes place, the conduction band minimum is shifted to a lower energy. The valence band maximum, however, remains energetically at the same location. Thus the effective bandgap of the material is lowered; i.e. emission will be redshifted. This phenomenon is known as the quantum-confined Stark effect (QCSE) [22], and is quite beneficial to LED structures because it allows InGaN-based structures to achieve longer emission wavelengths than would be possible for an unstrained alloy of equal In composition. Due to the aforementioned difficulties in synthesizing high In-content InGaN, one can readily see why this effect is so critical.

However, the QCSE also has some negative effects on LED structures. First of all, it tends to broaden emission spectra relative to the flat-band case. This is because the band-bending causes a range of emission energies, as opposed to the (theoretically) single value present in the unstrained material. Also, the QCSE causes a decrease in internal

quantum efficiency due to decreased overlap of the electron and hole envelope functions. This issue will be discussed in further detail in Chapter 5.

*4.4.2 Composition modulation in InGaN*

Another major consequence of the 11% lattice mismatch is the emergence of nonhomogeneities in the In composition of the alloy. One such example is the formation of "nanoislands", which are nanometer-scale regions within the material which contain a higher In content than the surrounding matrix. The presence of these regions has been predicted theoretically [23] and detected by TEM [24,25]. The average size of these nanoislands been reported to be approximately 4-5 nm while their density is estimated to be on the order of $10^{12}$ $cm^{-3}$ [25].

The presence of nanoislands is actually quite beneficial for LED structures. These quantum-dot-like states cause localized minima/maxima in the conduction/valence band of the quantum well, thus providing energetic traps for charge carriers [26]. This leads to an increase in the internal quantum efficiency of the structure, as the enhanced confinement prevents the trapped carriers from diffusing to nonradiative recombination centers, such as dislocations.

Another consequence of the large interatomic spacing mismatch between GaN an InN is the presence of a solid phase miscibility gap. A phase diagram of the InGaN system is given in Figure 4.5.

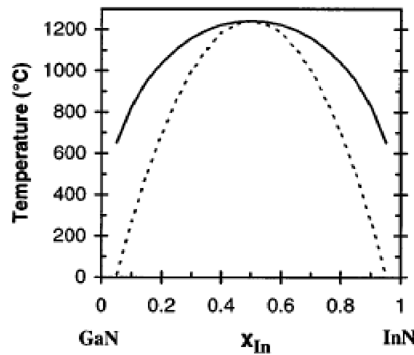

Figure 4.5 Binodal (solid) and spinodal (dashed) curves for the InGaN system [27]

If a point representing a given composition and temperature falls outside of both lines, the material is considered to be thermodynamically stable with respect to phase separation. On the other hand, if the point falls inside the dashed lines, the material is thermodynamically unstable and will transform homogeneously (i.e., without nucleation and growth) via spinodal decomposition into two separate phases: one containing a high In concentration and one containing a low In concentration. The predicted composition of each phase can be determined from this diagram by drawing an isotherm through the point and noting the two places where this line crosses the binodal curve.

A third possibility is that the point lies between the binodal and spinodal curves. This represents a material in a metastable state; phase separation may occur by a nucleation and growth process, but only if triggered by lattice discontinuities [28] or InN precipitation [29]. Experimental verification of this phase separation has been well-reported [30,31].

Obviously, this compositional instability is quite an impediment to the growth of high In content material. It puts a severe limit on the amount of In that can be

incorporated into the alloy, thus making the growth of long-wavelength InGaN-based devices even more challenging.

It is important to note that Figure 4.5 was calculated for bulk InGaN. The situation may actually be somewhat less severe when dealing with InGaN/GaN quantum wells. This can be understood by referring to Cahn's theory of spinodal decomposition [32], which deals with three energy terms: the free energy per unit volume (i.e., the driving force of the spinodal); the gradient energy term (which arises from the non-constant composition); and the strain energy term [33]. Whereas the free energy per unit volume is necessary for the spinodal to take place, the gradient and strain energy terms work against its presence. Therefore, in a highly-strained structure (such as an InGaN well sandwiched between GaN barriers), the spinodal may perhaps be suppressed relative to the unstrained case. For this reason, it has been suggested [34] that one can achieve somewhat higher In content in InGaN/GaN structures without phase separation than what is predicted by the standard models. This theory, however, is not universally accepted.

## 4.5 Growth of InGaN – Experimental

### *4.5.1 Growth conditions*

Growth of InGaN-based structures was successfully carried out using the TSS-CCS. The overall goal of this study was to obtain, if possible, a series of InGaN/GaN structures which achieved emission over the entire visible spectrum. In the process, we hoped to experiment with and verify some of the theory discussed in the previous section.

The conditions used to grow InGaN-based structures differed in many ways from those used for binary GaN. The major parameters are listed as follows:

- Trimethylindium (TMI) was introduced as an indium source. This is the standard In-containing organometallic for MOCVD use.
- The growth temperature was lowered to the 700˚-800˚C range. As explained in Section 4.3, lower growth temperatures are necessary in order to incorporate any appreciable amount of In into the alloy.
- The ammonia flow was increased to 4 slm. Lowered growth temperature leads to inefficient cracking, thus more $NH_3$ is necessary. As discussed in Section 4.3, a large overpressure of N is desirable in order to suppress the formation of In metal droplets.
- Pressure was increased to 500 torr. This was also in an effort to increase the N overpressure.
- TMG flow was reduced to 3.5 μmol/min, thus dropping the growth rate to 27.0 Å/min. (Details of the measurement of this growth rate will be given in Section 4.5.3). This is necessary because the reduced growth temperature leads to a reduced cracking efficiency of $NH_3$ and thus less atomic nitrogen present during the growth process.
- No hydrogen was introduced into the chamber during InGaN growth; as Piner *et. al.* have demonstrated that hydrogen reduces the amount of In incorpation into the alloy [35].
- InGaN structures were grown on a 1.5-2.0 μm n-type GaN template, as if they were part of a device structure.

- Unless otherwise noted, the InGaN structures were not thick InGaN layers but rather InGaN quantum wells with GaN barriers.
- As mentioned in Section 3.5, there were two different substrate sizes used in this substrate. For each set of data, the appropriate size will be noted in the text and shown schematically in the figures.

#### *4.5.2 Dependence of TMI flow and growth temperature*

Intuitively one may believe that increasing the TMI flow would lead to an increase in In content in an InGaN alloy. However, as discussed in Section 4.3.2, this is not always the case, particularly at high growth temperatures. This is illustrated in Figure 4.6 for a series of 1.0 μm InGaN layers grown at a relatively high temperature of 875 ºC on square substrates.

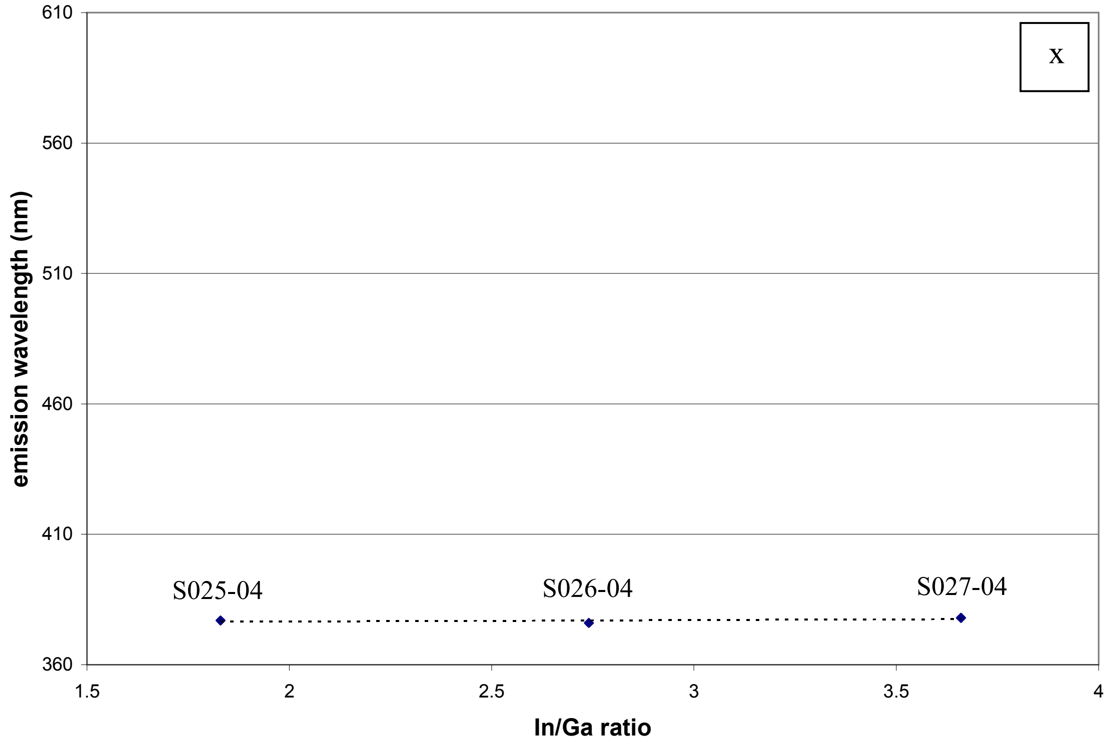


Figure 4.6 Emission wavelength vs. In/Ga ratio for samples grown at 875ºC

An explanation for the behavior shown in Figure 4.6 lies in the Bedair model. For high growth temperatures, $F_d$ is the controlling factor in the rate equation. An increase in $F_{in}$ simply leads to a corresponding increase in $F_d$ and hence no increase in $F_s$. Thus, one should not expect to see an increase in emission wavelength under the stated conditions.

In contrast, reducing the growth temperature has been shown to be effective way to increase $F_s$. This was verified by a series of InGaN/GaN quantum well structures grown at different temperatures on square substrates. For each point, well/barrier growth time was 90 sec/270 sec (~45Å/120Å thickness) and the In/Ga ratio was 0.73. The data is shown in Figure 4.7.

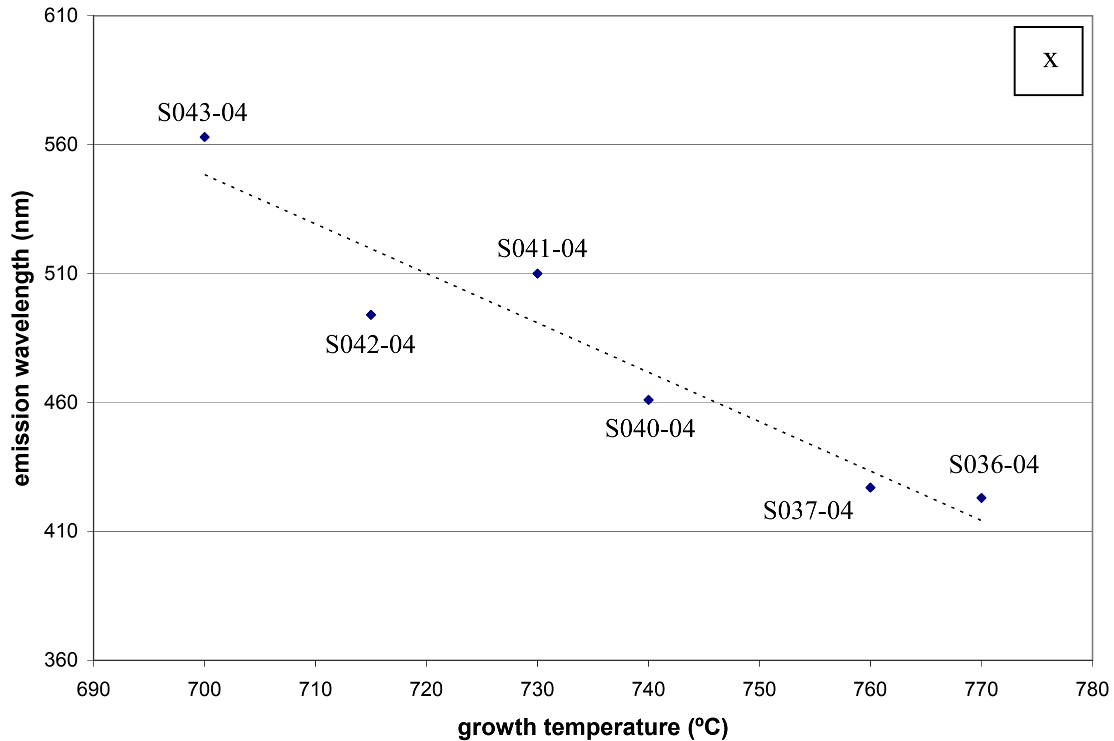


Figure 4.7 Emission wavelength vs. growth temperature for a series of InGaN/GaN quantum wells

This figure illustrates what may be the single most important principle in the study of InGaN growth: growth temperature, not In/Ga ratio, is the primary parameter that determines the indium content of a given structure.

### *4.5.3 Capping of InGaN structures*

The wavelength vs. temperature data given in Figure 4.7 are useful insofar as it illustrates the critical relationship between growth temperature and indium content. However, these data are of limited use if one is considering device growth. This is because, after growth of the InGaN wells, the device structure will be subject to further growth steps that could affect the active layers. This can explained through use of the simplified diagram of a typical InGaN-based LED structure shown in Figure 4.8:

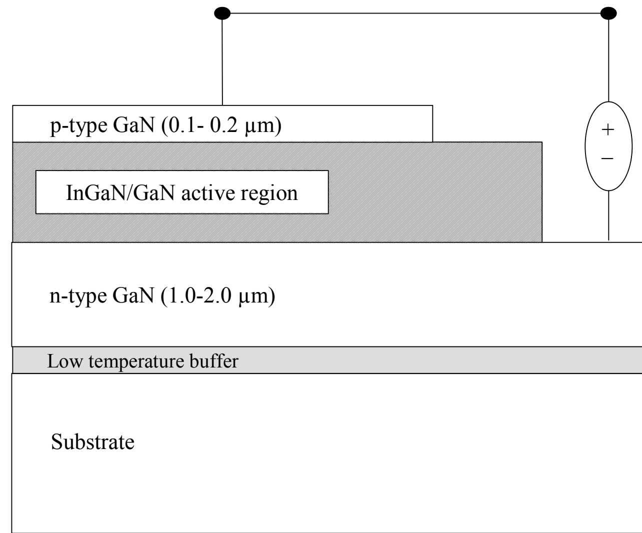


Figure 4.8 Simplified diagram of a typical InGaN-based LED structure

Figure 4.8 shows that, in a typical LED structure, a layer of p-type GaN must be grown on top of the InGaN active region, i.e. the InGaN must be "capped." As discussed in Chapter 3, p-type GaN is usually grown at a temperature of ~1020ºC. This is well above the temperature at which InGaN can be successfully grown, so the InGaN can potentially be negatively affected by the final high-temperature growth step. Experimental research has shown this to be the case [37,38].

There are two primary ways in which the capping procedure can affect the underlying InGaN structure. The first is a darkening of the sample surface. This is due to the out-diffusion of In atoms from the InGaN layers and subsequent formation of metallic In platelets. This loss of In from the ternary layers will then, of course, cause a second problem: a blueshift of emission wavelength as compared to an uncapped sample.

In more extreme cases, the In loss from the active layers is so great that visible emission is no longer measured from the sample.

In order to minimize these detrimental effects on the LED structures, several steps were taken. First, p-type GaN was optimized at a slightly lower growth temperature (950-975ºC), as discussed in Chapter 3. This will reduce the thermal damage as compared to growth at the standard temperature of 1020ºC.

It was also necessary to add an extra set of process steps to the growth recipe. After the growth of the final InGaN/GaN period, the growth temperature was increased by 90ºC and allowed to stabilize. This was followed by 6-20 minutes of GaN growth at the same TMG and $NH_3$ flows as the InGaN steps. A very small (50 sccm) H2 flow was introduced as well. This resulted in the deposition of a 400-1200Å low-temperature (LT) capping layer. After this LT layer was grown, the temperature was increased to the p-type capping temperature (950°C - 975ºC) and p-type GaN growth under standard conditions was begun [39].

Throughout the remainder of this dissertation, all InGaN/GaN data to be presented was measured from samples capped using the technique outlined above.

### *4.5.4 Growth rate of capped InGaN/GaN layers*

As mentioned in Section 4.5.1, the growth rate of the InGaN/GaN structures was reduced significantly from the value determined in Chapter 3. The new value was calculated from a series of $\omega$-2$\theta$ XRD measurements for 4-well InGaN/GaN structures. Data was taken from both the center and the tip of capped wedge-shaped samples. The scans are shown in Figure 4.9.

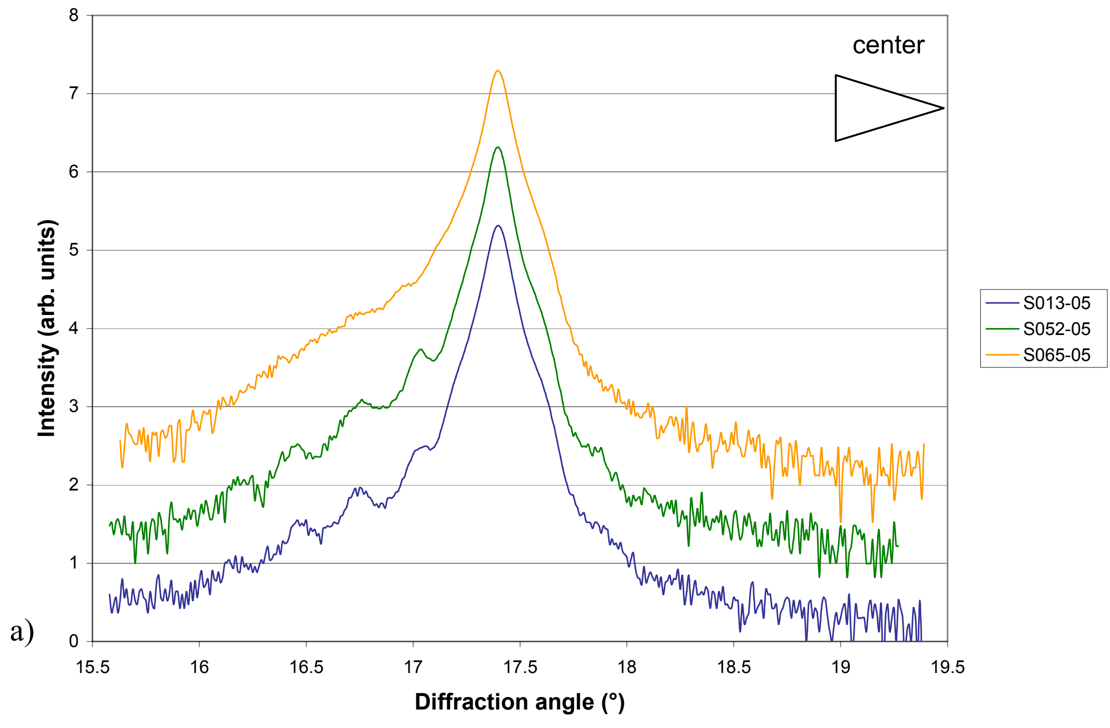


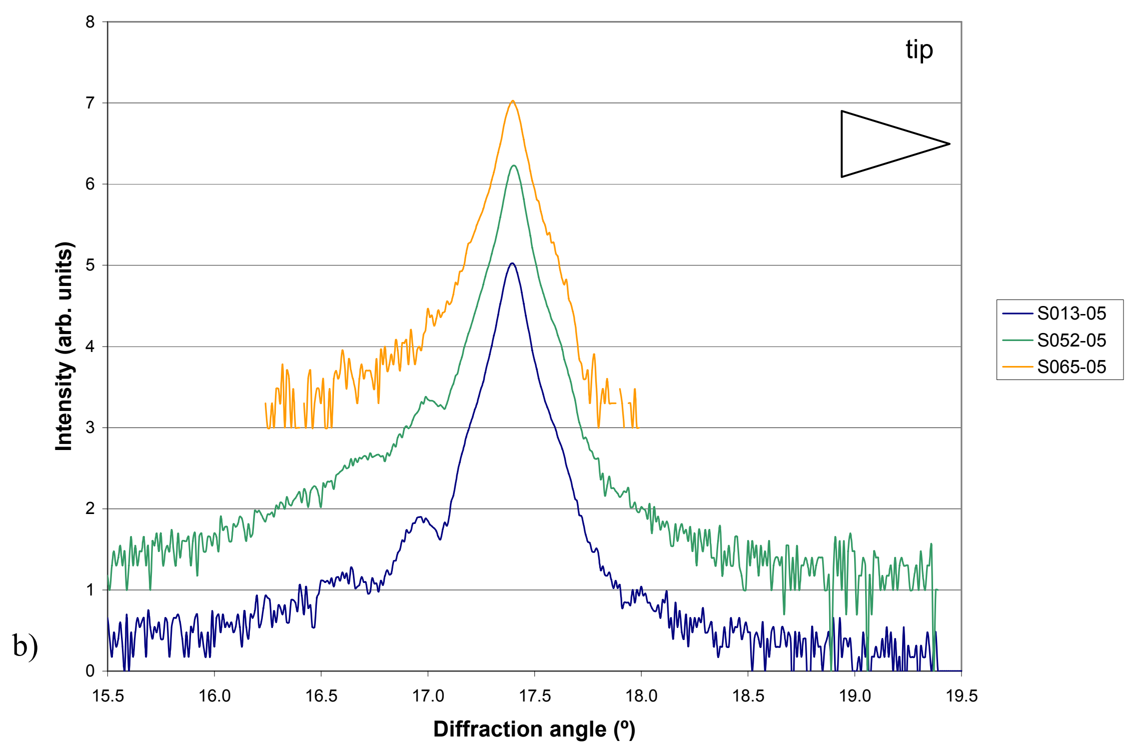


Figure 4.9 ω-2θ x-ray scan of a series of capped 4-well InGaN/GaN structures, measured at the (a) center; and (b) tip

Each curve shows a series of superlattice peaks which are the result of the periodicity of the quantum well structures. The period of each superlattice can be calculated from the following formulation of Bragg's law [36]:

$$t = \frac{\lambda_{CuK\alpha}}{2(\sin\theta_1 - \sin\theta_2)} \qquad \text{(Eq. 4.5)}$$

where $\lambda_{CuK\alpha}$ = the wavelength of Cu Kα x-rays (1.54 Å), $\theta_1$ and $\theta_2$ are adjacent superlattice peaks, and t is the period thickness.

Table 4.1 lists the thickness values and growth rate, along with quantum well growth temperature, for both regions on each of the samples.

Table 4.1 Growth rate and temperature of a series of InGaN/GaN MQW structures

| Sample | Well growth temperature (°C) | center | | tip | |
|---|---|---|---|---|---|
| | | Period thickness (Å) | Growth rate (Å/min) | Period thickness (Å) | Growth rate (Å/min) |
| S013-05 | 750 | 149 | 27.0 | 135 | 24.6 |
| S052-05 | 740 | 165 | 29.9 | 177 | 32.2 |
| S065-05 | 700 | 184 | 33.5 | 192 | 35.0 |

These measurements indicate only minimal differences in growth rate between the center and tip regions of the wafer. Moreover, the slight variation that is seen is not consistent from sample to sample and therefore likely due to experimental scatter. For these reasons, InGaN/GaN MQW growth rate can be regarded as fairly uniform across each wafer.

These data do, however, clearly show that the growth rate is temperature-dependant. This observation holds true for both tip and center measurements. The trend is plotted in Figures 4.10 and 4.11 for center measurements and tip measurements, respectively.

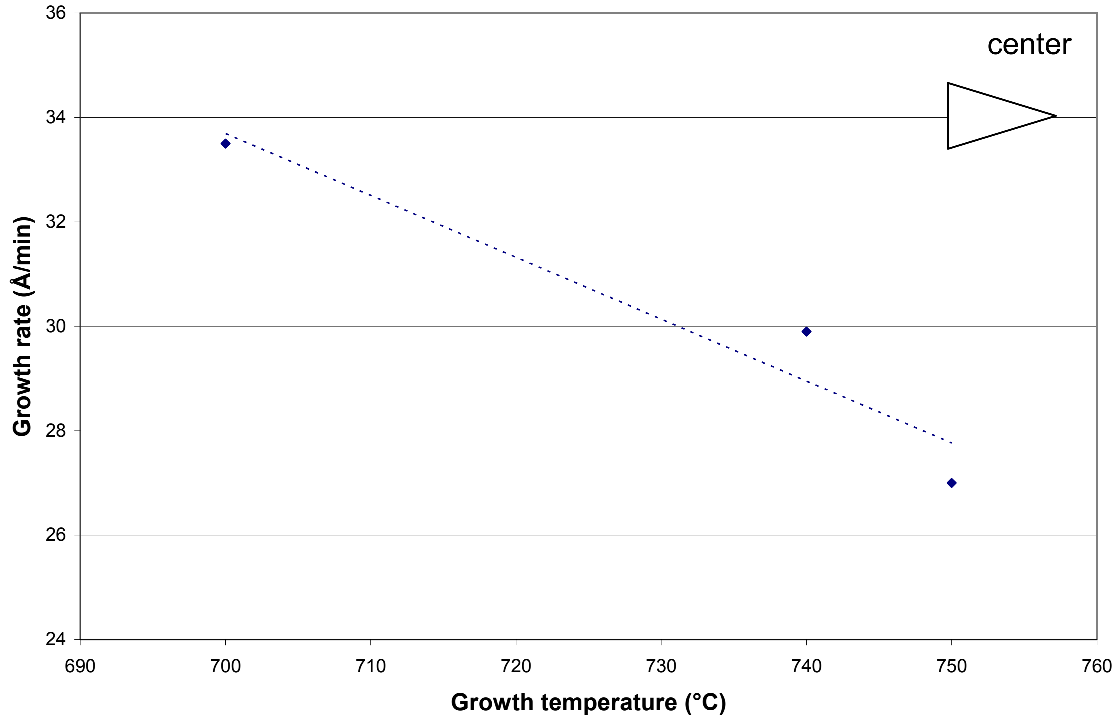


Figure 4.10 Growth rate vs. growth temperature for capped InGaN/GaN structures, measured at the center

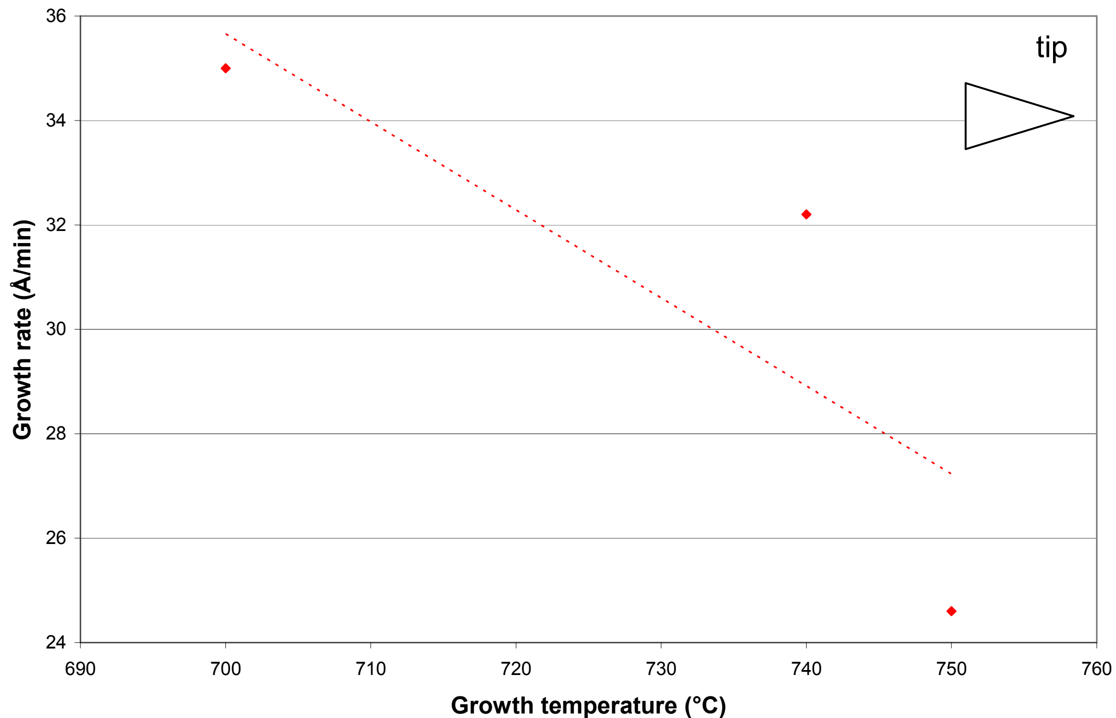


Figure 4.11  Growth rate vs. growth temperature for capped InGaN/GaN structures, measured at the tip

This dependence arises because an increased growth temperature leads to increased desorption of In during growth, as per the Bedair model. Thus, lower-temperature growth retains more alloyed InGaN on the surface ($F_s$), leading to increased growth rates.

Another important conclusion from the ω-2θ XRD scans is the experimental verification of a periodic multi-quantum well (MQW) structure. If this periodicity did not exist, the x-ray spectra would not show the superlattice peaks present on the low-angle side of the GaN peak. Indeed, in Figure 4.9, as temperature was lowered and crystal quality degraded, the superlattice peaks became less distinct.

Further verification of the crystal structure came from transmission electron microscopy (TEM) analysis. The sample analyzed was that from Figure 4.9 labeled "S013-05"(4 wells grown at 750ºC, well/barrier growth time = 60 sec/270 sec). The microscope used was a TOPCON 002B. The resulting images are given in Figure 4.12.

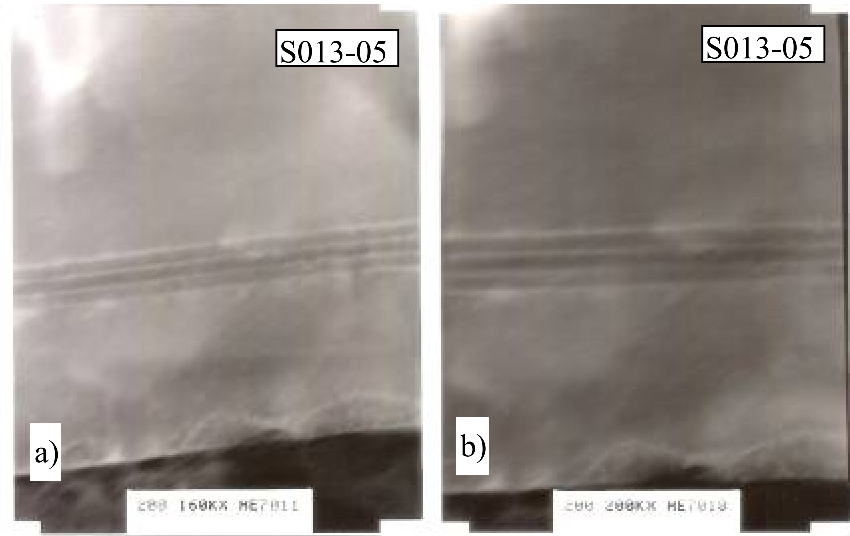


Figure 4.12 TEM images of a capped 4-well MQW structure at (a)160kX magnification; and (b) 200kX magnification

These images give additional verification of the structural integrity of the samples' InGaN/GaN MQW layers. They can also be used to roughly verify the XRD measurements given in Figure 4.9 and Table 4.1. In the 200kX image, 1 mm is equivalent to 50Å; leading to well and barrier thickness estimates of 38Å and 100Å, respectively. This is in good agreement with the values given for sample S013-05 in Table 4.1.

*4.5.5. Emission properties of capped of InGaN/GaN MQW structures*

Several series of capped InGaN samples were grown with the TSS-CCS. The capping procedure was as documented in the preceding section, excepting that there was no Mg flow during the "p-type" layer. This is because Mg-doped GaN has very distinctive PL characteristics (see Section 3.6.3) that would mask the PL measurements from the InGaN layers.

Figure 4.13 gives a plot of emission wavelength vs. growth temperature for a series of square-substrate samples capped at 975ºC. For this series, the well growth temperature is equal to the barrier growth temperature, the well/barrier growth time is 75 sec/270 sec, and the In/Ga ratio is 0.73.

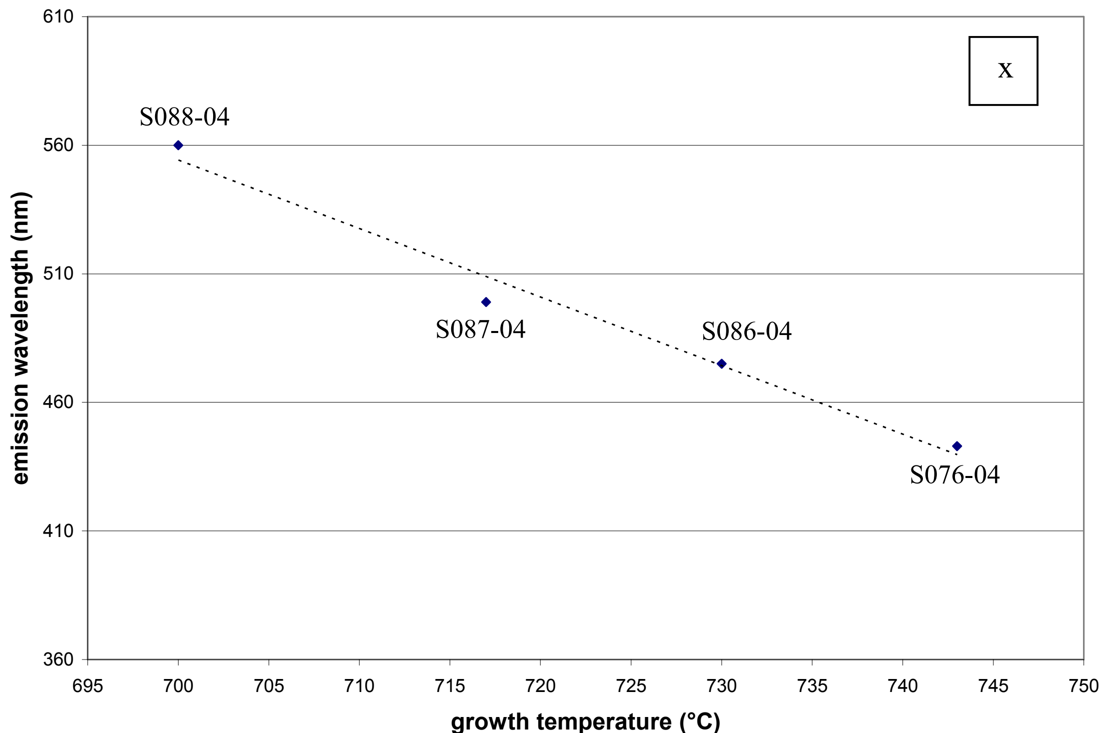


Figure 4.13 Emission wavelength vs.growth temperature for InGaN/GaN quantum well structures capped at 975ºC

This graph confirms what was seen for uncapped samples in Figure 4.7 and explained by Bedair model: a reduction in growth temperature leads to an increase in the amount of In incorporation in the alloy and therefore a redshift in the emission wavelength. This redshift is due not only to the reduced bandgap of the higher In-content material, but also the increased band-bending which accompanies the increased compressive strain that results from the higher In incorporation.

Figure 4.14 plots the full width at half-maximum of the emission peak for the same set of samples.

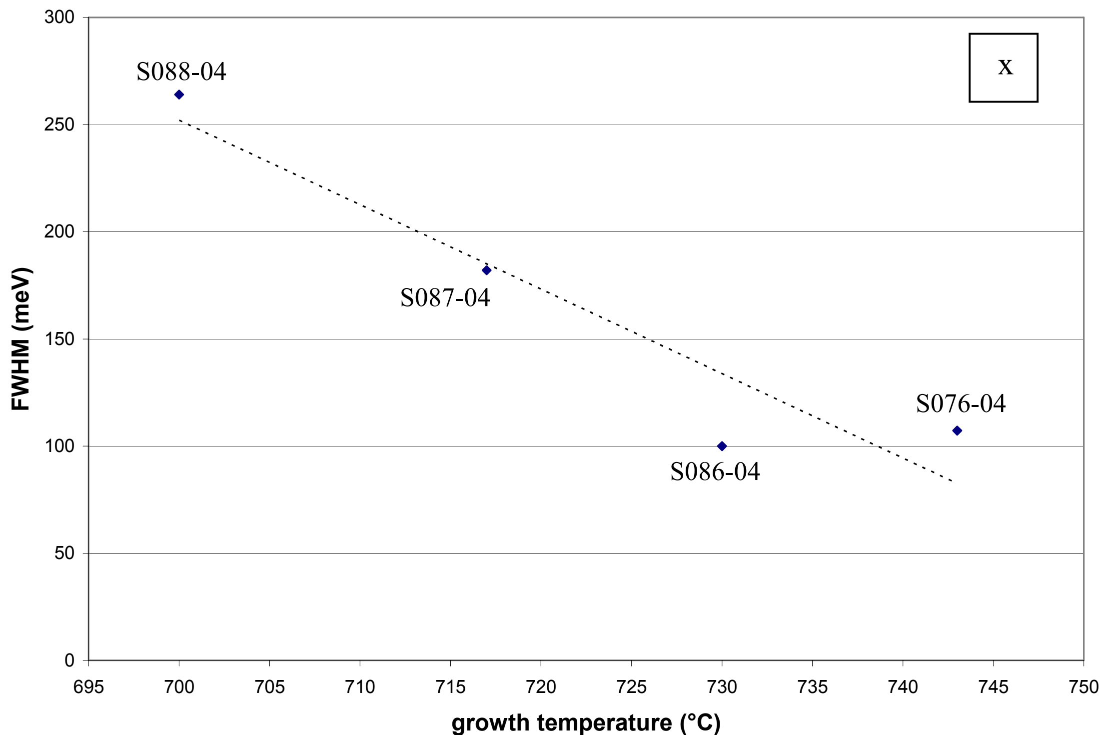


Figure 4.14 FWHM of emission peak vs. growth temperature for InGaN/GaN quantum well structures capped at 975ºC

The data in Figure 4.14 show a broadening of emission peak linewidths as the growth temperature is reduced. This is as expected, as the decreased growth temperature

will lead to greater indium incorporation, greater compressive strain, and thus increased band bending in the material. This increase in band-banding leads to broader linewidths because, as discussed in Section 4.4.1, greater deviation from the flat-band case will result in a greater range of emission energies.

Another trend that was examined is the relationship between emission wavelength and quantum well growth time. For this set of samples, $T_{well}$ = 708ºC, $T_{barrier}$ = 725ºC, In/Ga ratio is 0.73, and barrier growth time is 270 sec. Square substrates were used, and capping temperature was 975ºC. A plot of this data is given in Figure 4.15.

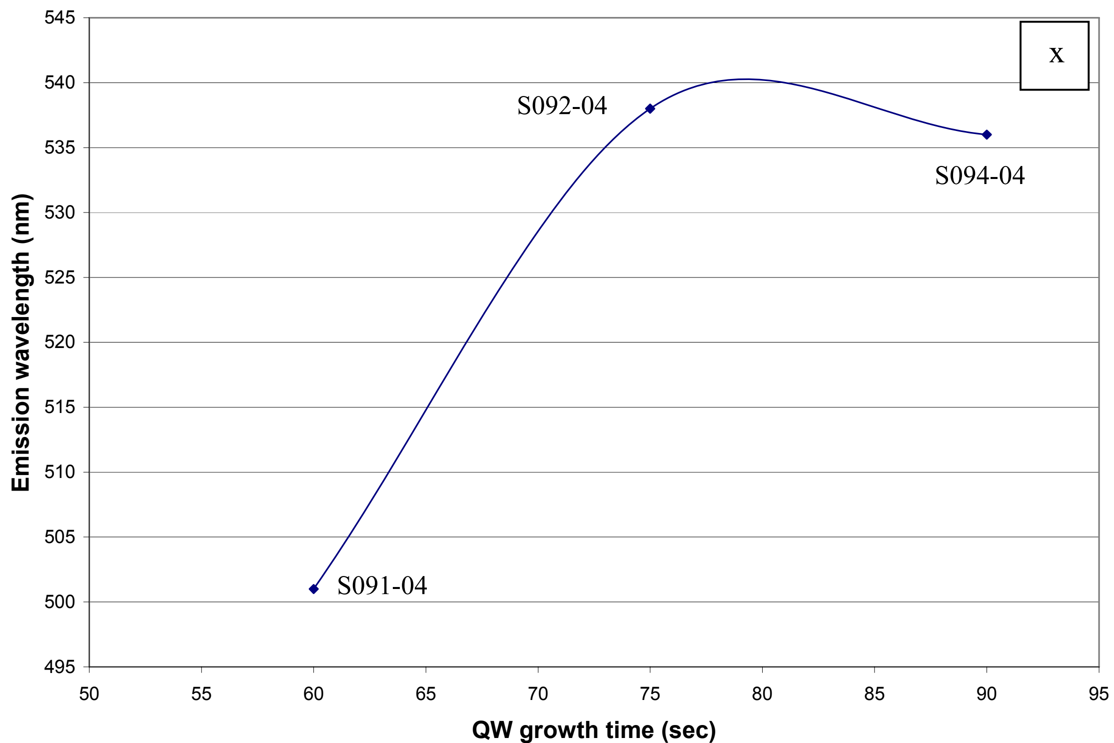


Figure 4.15 Emission wavelength vs. quantum well growth time for InGaN/GaN quantum well structures capped at 975ºC

The curve in Figure 4.15 shows on initial increase in emission wavelength that tapers off as growth time increases.

The initial increase can be explained due to two different phenomea: the quantum size effect (Section 4.1) and the quantum-confined Stark effect (Section 4.4.1). The quantum size effect (QSE) was explained in Eq. 4.1, which states that quantum energy levels in a potential well are reduced as the length of the well increases. InGaN/GaN quantum wells, in general, follow this relation. Thus, an increase in well width is accompanied by a small decrease in emission energy.

The role of the QSE, however, is minor compared to that of quantum-confined Stark effect (QCSE) (see Section 4.41). As the well becomes longer, the strain in the well increases and thus the band-bending becomes more severe. This increased band-bending leads to a reduction in the effective bandgap of the material, which is manifested in the increased emission wavelength.

However, Figure 4.15 also seems to indicate that there comes a point when the effects of QCSE appear to taper off. This is likely due to the onset of relaxation of the strain in the layer, thus reducing the amount of band-bending present. Relaxation in a strained film will occur once that layer reaches its critical layer thickness [40].

A series of calculations detailing with both the quantum size effect and quantum-confined Stark effect, as well as a discussion of strain relaxation and critical layer thickness, is given in Chapter 5.

The relationship between emission wavelength and trimethylgallium flux was also studied. Well/barrier growth temperature was 717ºC /740ºC and well growth type was 45Å. Square substrates were used. The data from these measurements are plotted in Figure 4.16.

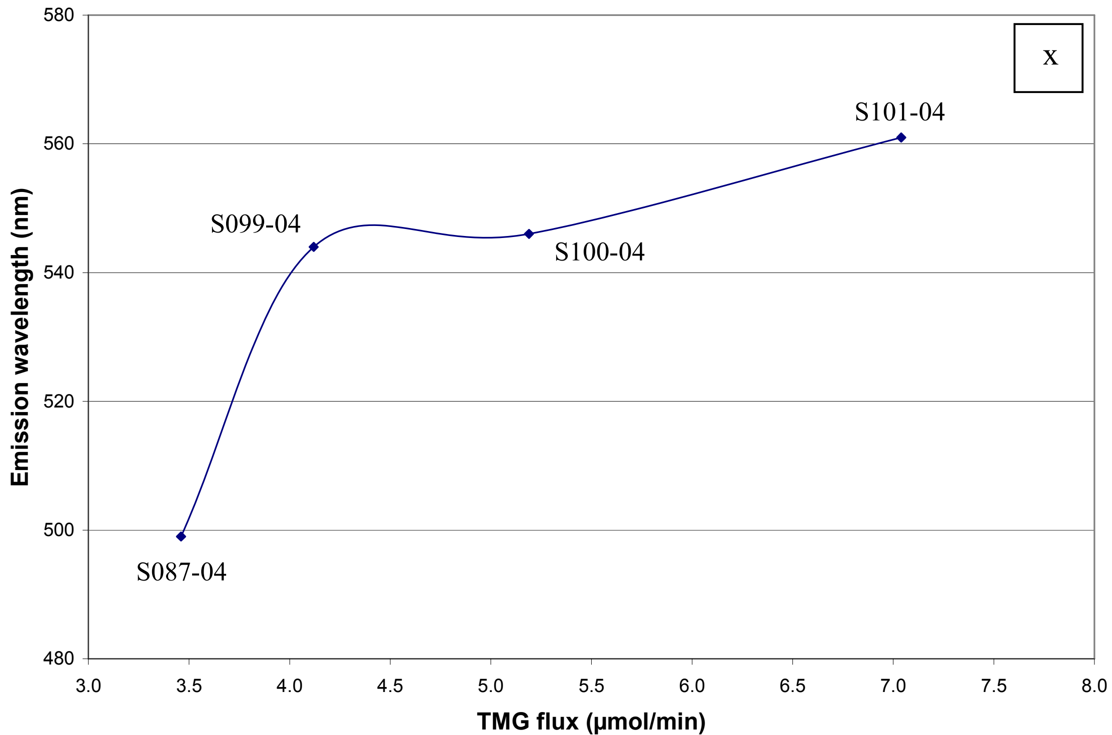


Figure 4.16 Emission wavelength vs. TMG flux for InGaN/GaN quantum well structures capped at 975ºC

The data in Figure 4.16 show a sharp initial increase in emission wavelength, which tapers off into a more gradual increase. The reason for this redshift is that a higher TMG flux enhances the In incorporation into the alloy.

This phenomenon can be explained using the Ga vs. In adatom residence time argument discussed in Section 4.3.2. Because Ga adatoms remain on the growing film surface longer than In adatoms, they can retain N atoms more efficiently. These N atoms will have unsaturated bonds, and therefore will be favorable sites for the formation of InN. If TMG flux is increased, the number of Ga adataoms will, of course, increase as well, leading to a greater quantity of unsaturated N atoms on the growing film surface. This will promote an increase in In incorporation and, consequently, an emission redshift.

*4.5.6 Spectrum achieved through capped InGaN structures*

Figure 4.17 shows the extent of the visible spectrum that was successfully achieved with 975º-capped InGaN/GaN structures grown with the TSS-CCS on 14x14mm square substrates. All intensities have been normalized in order to clearly distinguish the peak features. Without normalization, the peak intensities are inversely proportional to emission wavelength. This is due to the reduction in overlap of the electron and hole wavefunctions which results from the quantum-confined Stark effect.

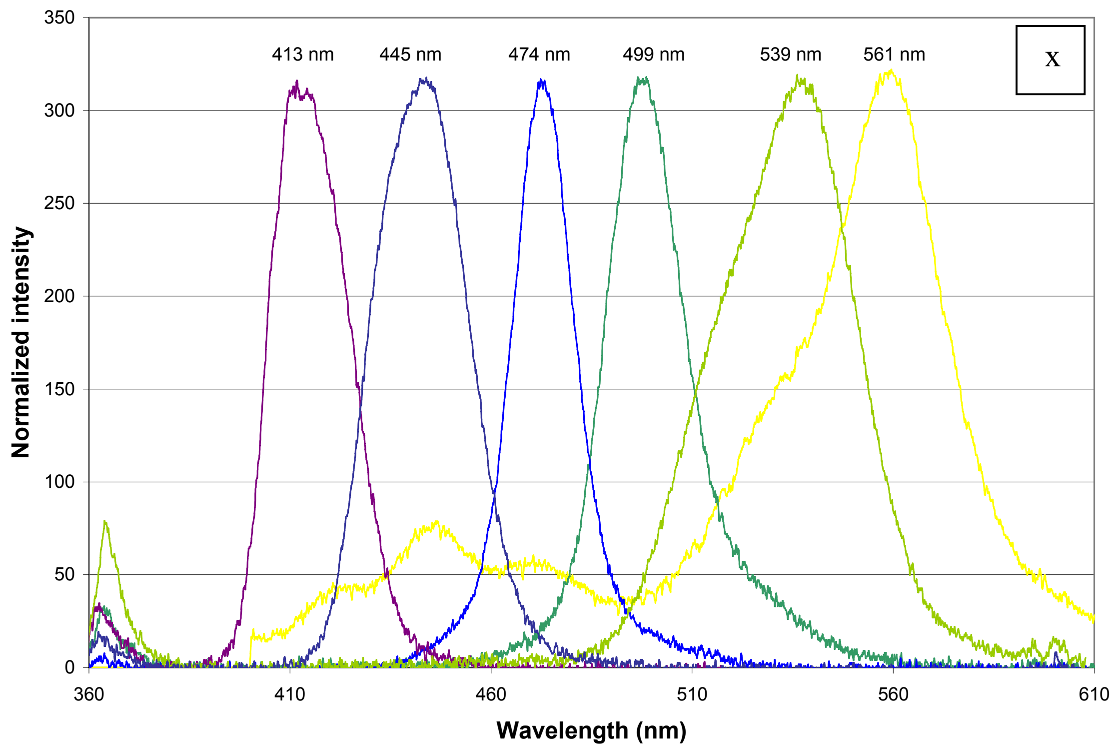


Figure 4.17 PL emission spectra obtained by capped InGaN/GaN structures grown on square substrates

Table 4.2 gives the run conditions necessary to achieve each spectrum given in Figure 4.17.

Table 4.2 Growth conditions used to achieve the spectra shown in Figure 4.17

| Run number | Emission wavelength (nm) | Well/barrier growth temperature (ºC) | Well/barrier growth time (sec) | Number of wells |
|---|---|---|---|---|
| S074-04 | 413 | 760/760 | 90/270 | 4 |
| S078-04 | 445 | 743/743 | 90/270 | 4 |
| S086-04 | 474 | 730/730 | 75/270 | 3 |
| S091-04 | 499 | 708/725 | 60/270 | 2 |
| S092-04 | 539 | 708/725 | 75/270 | 2 |
| S105-04 | 561 | 701/725 | 75/270 | 2 |

One of the key observations from this set of data is the presence of a minimum barrier temperature (725°C). It was found that any structures in which the barrier was grown at $T<725°C$ were metallic in appearance and exhibited poor emission characteristics; i.e., multiple peaks, weak emission, or no visible signal at all (see Section 4.5.8). This can be explained by that fact that, as growth temperature is reduced, the crystal quality of GaN is diminished and its surface becomes rougher. In this particular study, a temperature of 725°C is necessary in order to obtain the minimum crystal quality and surface smoothness necessary to obtain efficient quantum well structures.

Also note that the longest wavelength obtained was 561 nm, which is just at the onset of yellow emission. No structures that emitted amber or red photoluminescence were obtained. This is not surprising, as it becomes increasingly more difficult to grow efficient GaN based structures as the target wavelength increases. (This issue will be

discussed further is Chapter 5.) This apparent inability to achieve long wavelength emission makes it seem unlikely that the RGB device discussed in Chapter 1 can be fabricated. Thus, a different approach must be taken if one is to obtain a monolithic white LED based in the nitride system (see Chapter 6).

*4.5.7 Uniformity of InGaN/GaN MQW samples*

As mentioned in Section 4.5, there were two types of substrate used: 14x14 mm squares positioned in the center of the susceptor, and 1 in. long wedge placed radially across the susceptor. The purpose of the wedge-shaped substrates was to test the uniformity of growth across the susceptor. Initially, it was assumed that the growth would indeed be uniform based on the following observations:

a) Steady-state temperature uniformity across the susceptor was verified during the temperature calibration step (Section 2.3.2).
b) A nominally undoped GaN sample grown on a full 2" wafer gave uniform XRD and PL measurements.

However, experimental results proved otherwise, specifically in the case of InGaN-based structures. There was a significant degree of non-uniformity in the wedge-shaped samples. First, there was a remarkable change in appearance of the center and edge area as opposed to the tip. Whereas the tip always remained clear, the center and edge often had a gray or black-purple metallic appearance.

Additionally, these samples showed a marked difference in emission wavelength along the radial length of the sample. Variations were typically in the 30-40 nm range

from tip to center and 15-25 nm from center to edge. An example of these non-uniform emission characteristics is shown in Figure 4.18.

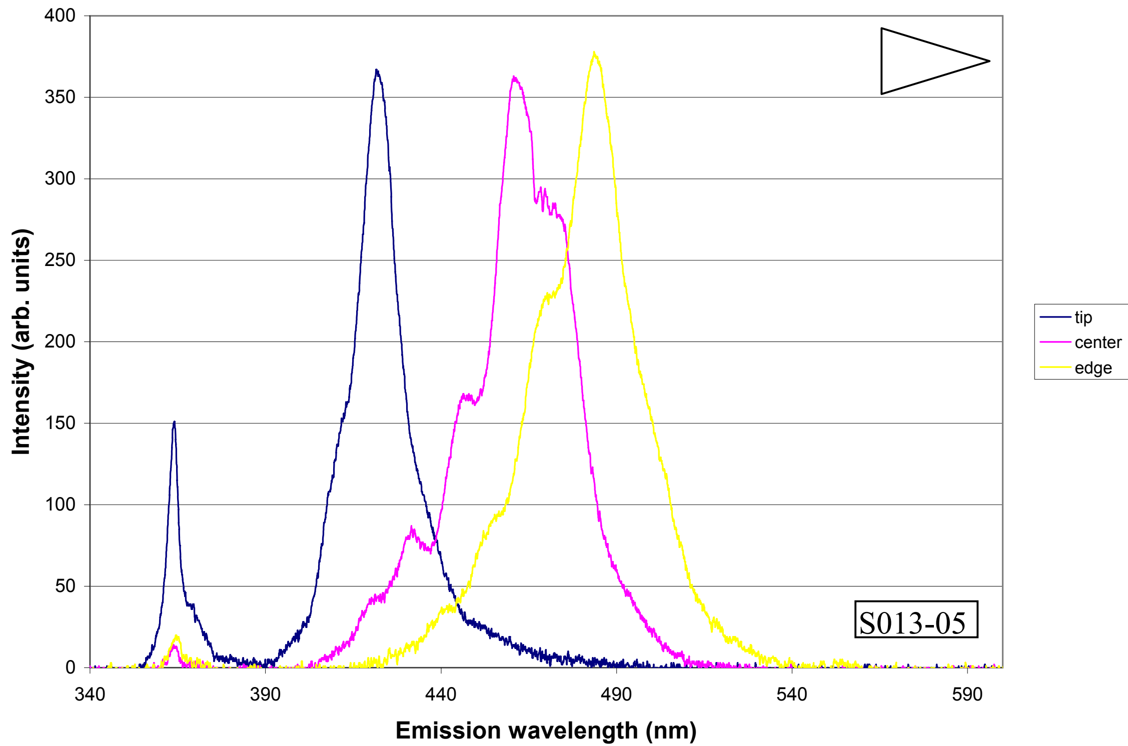


Figure 4.17 Example of non-uniform emission in an InGaN/GaN QW structure

The difference in emission wavelength ($\Delta\lambda$) across the given sample is quite severe: 62 nm, covering the visible spectrum from the violet to the far-blue. Such non-uniformity causes a serious problem, as it becomes impossible to grow the appropriate structures with well-controlled characteristics in the presence of this sizable radial variation.

One cause of the non-uniformity of the InGaN-GaN quantum well samples was found to lie in the geometry of the reactor's PBN-coated graphite heater. Top and side views of this heater are given in Figure 4.19.

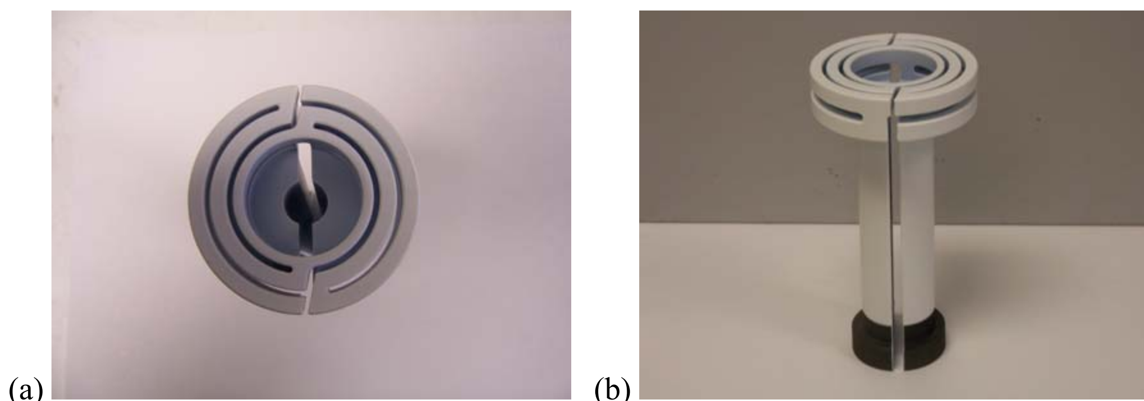

(a) (b)

Figure 4.19 (a) Top and (b) side views of reactor's PBN-coated graphite heater
Note: The reactor's thermocouple is fed through the center of the heater.

The photos show that the heater's main conductive elements are spread out to the edge, thus leaving an empty area in the center of the heater. Such a design does indeed leads to temperature uniformity over the susceptor, as reported by the manufacturer and verified by calibration. However, the *heating rate* will not be uniform when using a heater of this design. The edges of the susceptor will heat up first; then the temperature of the center will catch up as the edges are cooled by the reactor's gas flow.

Once this problem was identified, appropriate steps were taken to reduce the effects of the ramp rate non-uniformity. The ramp times of the protective layer and the p-type cap were lowered to 0.30 °C/min and 0.17 °C/min, respectively. This had the desired effect of improving the uniformity over the bulk of the susceptor, as shown in Figure 4.20.

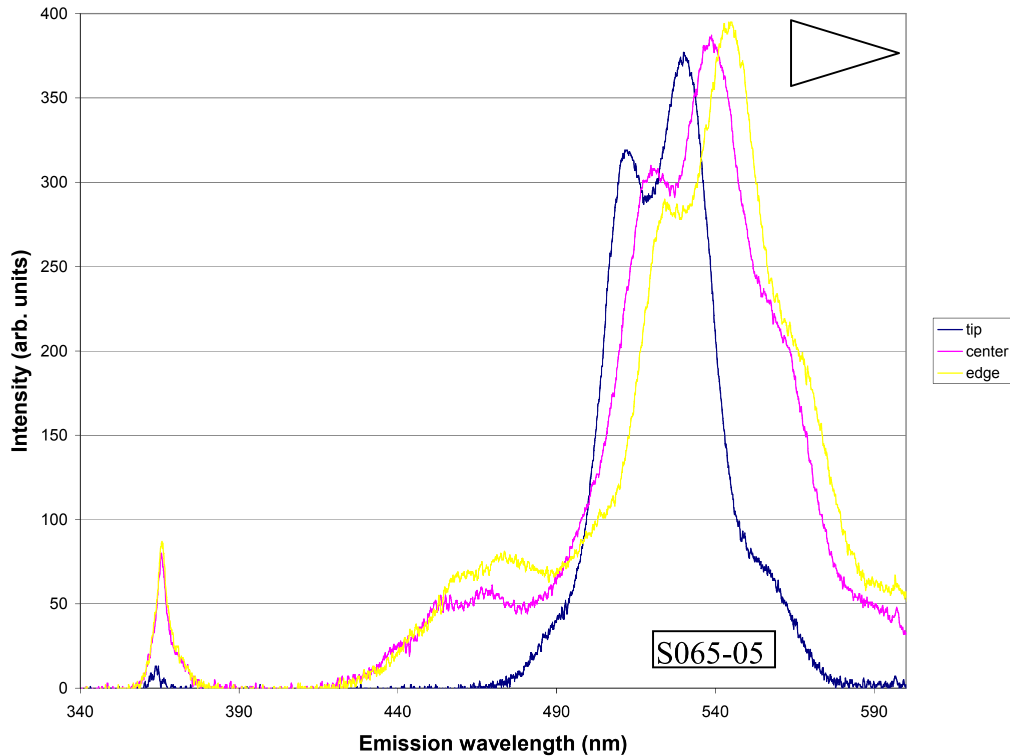


Figure 4.20 Example of improved emission uniformity in an InGaN/GaN structure due to reduced temperature ramp rate

These data show a marked improvement in emission uniformity (total variation of only 14 nm) over that shown in Figure 4.18. However, the nonuniformity was not eliminated completely; a certain degree of variation remained present in all subsequent samples. The general trend remained consistent: shortest wavelengths in the tip, increasing as one moves toward the base. Also, the $\Delta\lambda$ between tip and center was generally larger than that between center and base.

One potential source for this nonuniformity is of thickness variation. As discussed in Section 4.4.1 (and shown in Figure 4.15), emission wavelength is dependent on quantum well width. However, the growth rate data given in Section 4.5.4 showed little thickness variation between the tip and center; and the slight variation that was seen

did not follow any consistent trend. For this reason, it seems unlikely that variation in well width is the root cause of the observed emission nonuniformity.

Another possible explanation of this nonuniformity is the variation in surface roughness in the underlying n-type GaN layer. As discussed in section 3.6.1, the surface roughness of wedge-shaped n-type GaN sample was shown to increase as one travels from tip to base. It can be speculated that the rougher film surfaces at the center and base offer better nucleation sites for InGaN nanoislands (Section 4.4.2) than the smoother surface at the tip. This enhanced nucleation may then lead to larger diameter nanoislands with higher In content. Further study is needed before a conclusion regarding this possible roughness/wavelength relationship can be reached.

Once the uniformity issue was addressed, more experimentation was carried out in order to replicate the spectra in Figure 4.17 (which were measured from a small spot in the center of square substrates) with emission measurements take from the center of wedge-shaped substrates. This is critical because centers of the wedges offer more workable area with which devices can be fabricated than the centers of the squares. The results are shown in Figure 4.21, with run conditions given in Table 4.3.

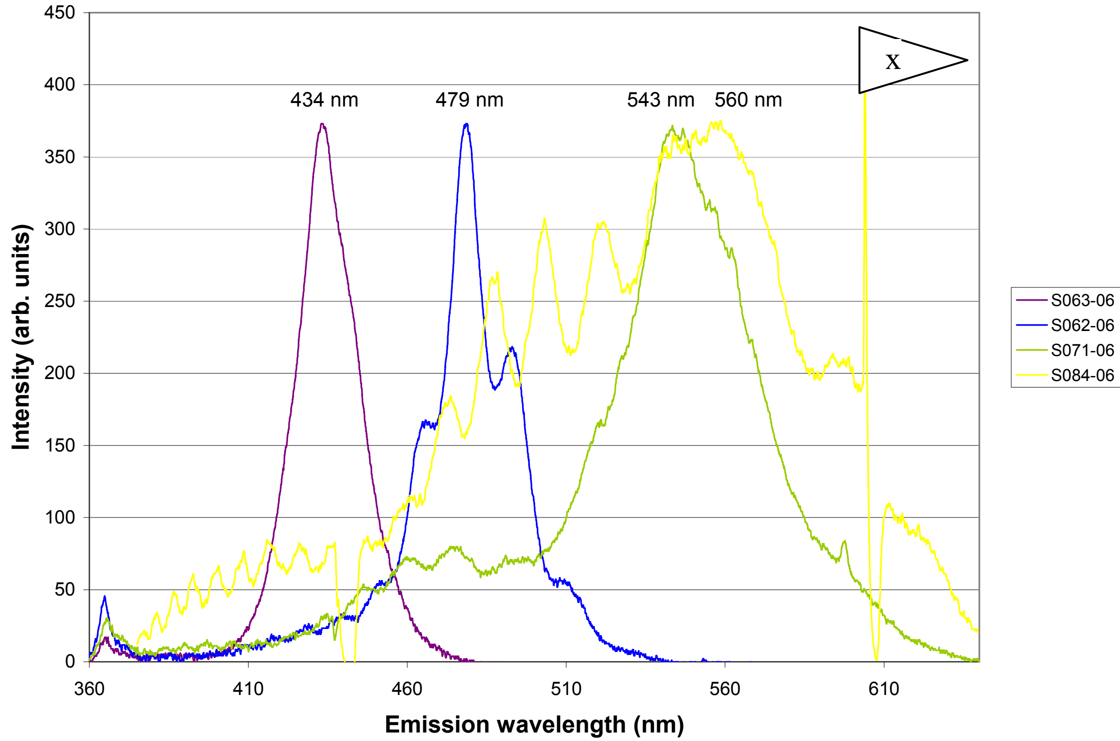


Figure 4.21 PL emission spectra obtained by capped InGaN/GaN structures on wedge-shaped substrates

Table 4.3 Growth conditions used to achieve the spectra shown in Figure 4.21

| Run number | Emission wavelength (nm) | Well/barrier growth temperature (ºC) | TMG flux (μmol/min) | TMI flux (μmol/min) |
|---|---|---|---|---|
| S063-06 | 434 | 770/770 | 3.3 | 2.5 * |
| S062-06 | 479 | 750/750 | 3.3 | 2.5 |
| S071-06 | 543 | 725/760 | 3.3 | 2.5 |
| S084-06 | 560 | 725/760 | 6.6 | 5.0 |

* capped at 1000°C

PL emission spectra comparable to that obtained from the square substrates was successfully achieved for wedge-shaped substrates.

*4.5.8 Indium platelet formation in capped InGaN/GaN structures*

Even after uniformity was established, some samples still took on a dark, metallic appearance, as shown in Figure 4.22. Such discoloration was especially common for samples with high In content, high capping temperature, or a fast temperature ramp rate.

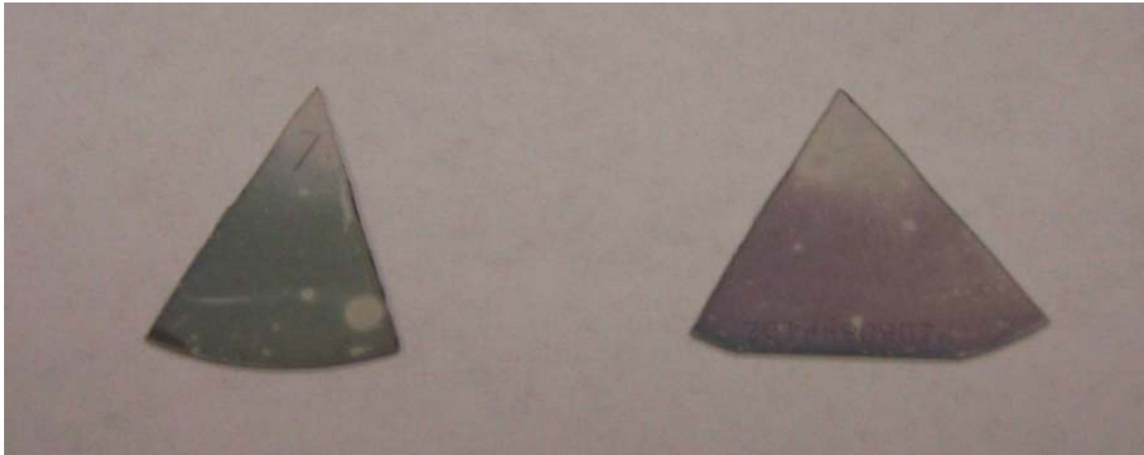

Figure 4.21 Photos of capped InGaN/GaN QW samples with metallic appearances

It was noticed that the onset of this metallic appearance coincided with a degradation of the emission characteristics of the sample. In less severe cases, there was merely a small blueshift (as compared to similar uncapped structures) in the emission peak. However, most metallic-looking samples exhibited multiple broad, weak peaks; or in the most extreme cases, a total loss of visible emission. This indicates that the metallic appearance is a visual indication of indium metal that has been lost from the InGaN quantum wells. Figure 4.23 shows an example of the degraded emission characteristics that arise from a sample with appreciable metal formation.

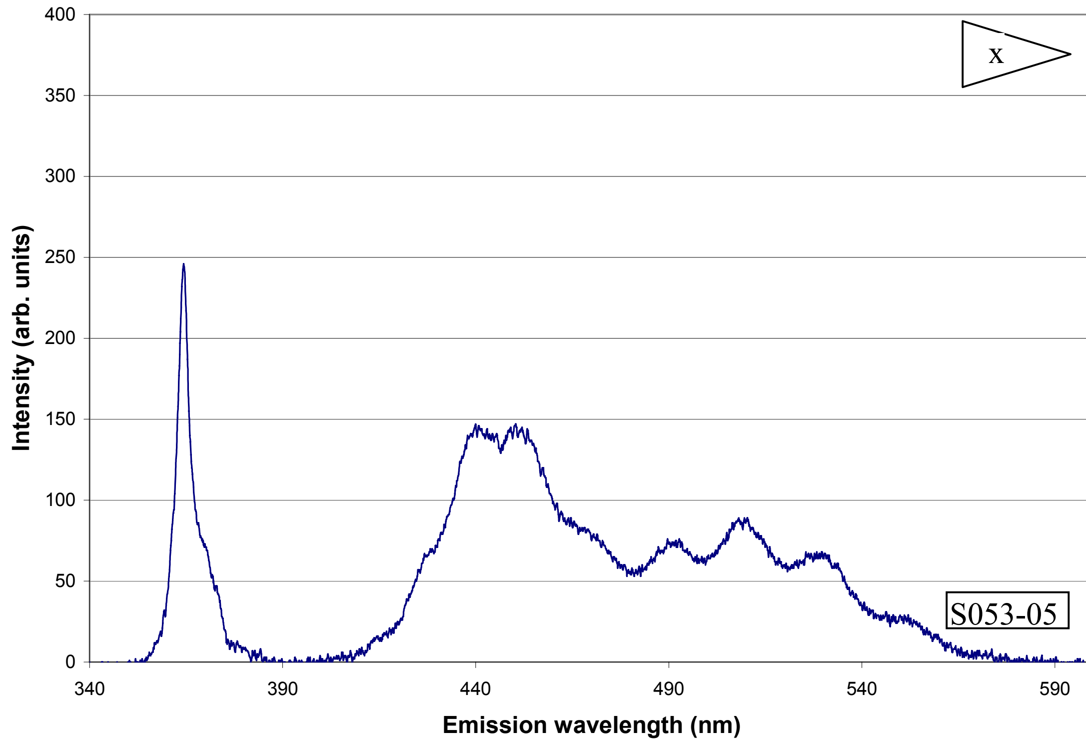


Figure 4.23 Degraded emission characteristics from metallic InGaN/GaN structure

One of the first questions to be addressed was whether an appreciable amount this visible indium had accumulated on the surface of the sample. This was done placing a number of metallic-appearing samples in a 2-hour hydrochloric acid bath. This treatment had no observable effect on the appearance of the samples. Thus it can safely be assumed that the visible indium is not actually on the surface of the sample, but rather embedded in the quantum-well structure itself.

The formation of this metallic appearance was found to be the result of the growth of the high temperature capping layer. This was determined by a series of samples which were grown with (a) no cap, (b) a protective layer only, or (c) a protective and high-temperature cap. Visible indium was observed only in the sample in which the high temperature cap was grown.

In an effort to understand the microstructural changes that cause the formation of visible indium, an XRD study was carried out. ω-2θ curves were measured for several capped InGaN/GaN samples. Some were clear (labeled S013-05, S052-05, and S065-05), while others were metallic-looking (S034-05 and S053-05). The scans are shown in Figure 4.24.

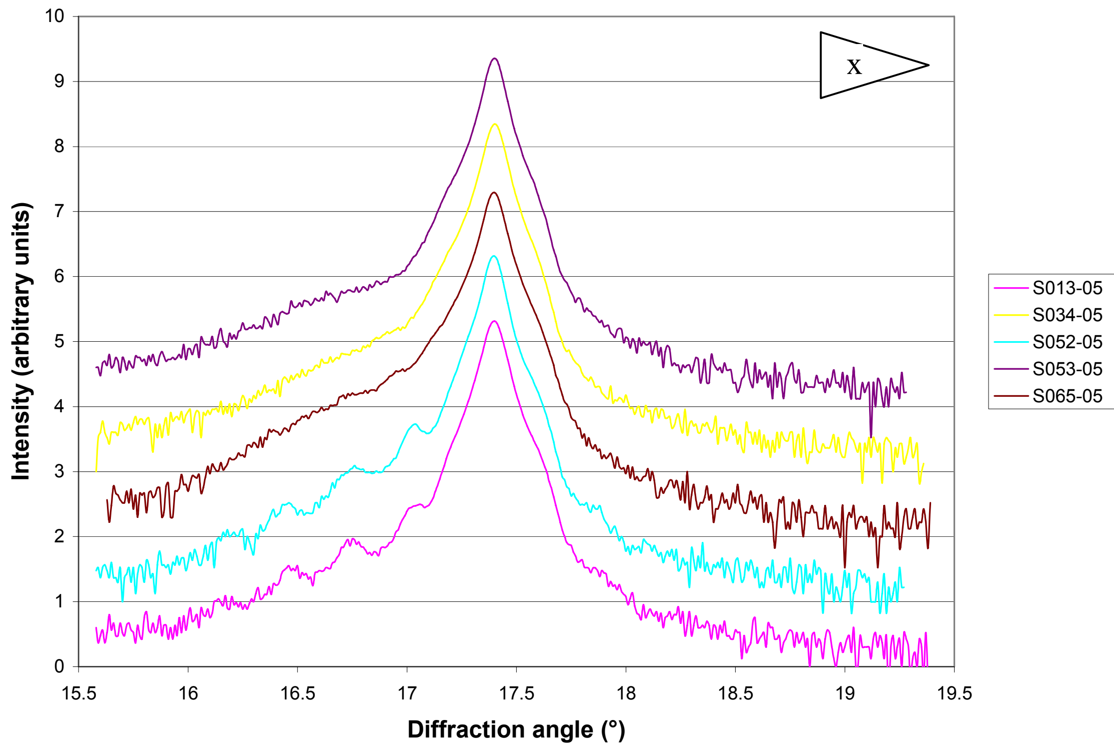


Figure 4.24 XRD of clear and metallic-looking capped InGaN/GaN samples

What these data show is that when the sample is capped in such a way that the sample remains clear (as in the case of S013-05, S052-05, and S065-05), the sample retains its periodic quantum well structure, as evidenced by the presence of superlattice peaks. However, when appearance of the sample becomes metallic (S034-05 and S053-05), there is a loss of this periodicity, i.e., the quantum wells have been compromised.

With this loss of the quantum well structure, of course, comes the loss of well-defined carrier confinement. This helps explain why emission characteristics are degraded when the sample becomes discolored.

Jacobs, *et. al.*, have carried out similar XRD measurements on clear and metallic-looking samples and reported similar results to those seen here [37]. Their publication also contains TEM images which further demonstrate the loss of the quantum well structure for samples showing visible indium. These images also reveal the presence of In platelets which are the root cause of the samples' metallic appearance.

A complete explanation of this In platelet formation has not been ascertained. One possible explanation is that high-temperature capping coarsens In droplets that form in the layer during growth ($F_m$ in the Bedair model). This is likely because In droplets are very effective nucleation centers for platelet growth [37].

Another possibility is related to the miscibility gap present in InGaN [38]. As discussed in Section 4.4.2, InGaN is either metastable or unstable with respect to spinodal composition over a wide area of the material's phase diagram. Thus, the high temperature cap growth may trigger the transformation of relatively homogeneous InGaN into two distinct phases: one of higher In content and one of lower In content. However, if the In-rich phase is nitrogen-starved, or the formation of the In—N bond is thermodynamically unstable, this "phase" may simply be indium metal.

More research into the exact mechanism of (and, of course, the prevention of) indium platelet formation is sorely needed. It is a serious detriment toward the realization of long-wavelength InGaN-based LED's.

## 4.6 References


1. B.G. Streetman and S. Banerjee. *Solid State Electronic Devices*, Ch. 3.2.5. Prentice Hall, Upper Saddle River, NJ (2000).

2. R.A. Serway, C.J. Moses, and C.A. Moyer. *Modern Physics*, Ch. 5.4. Harcourt Brace Jovanovich College Publishers, Forth Worth (1989).

3. R. Dingle, W. Wiegmann, and C.H. Henry. "Quantum states of confined carriers in very thin $Al_xGa_{1-x}As$-GaAs-$Al_xGa_{1-x}As$ heterostructures." *Phys. Rev. Lett.* **33**, 827 (1974).

4. H.J. Hovel and J.J. Cuomo. "Electrical and optical properties of rf-sputtered GaN and InN." *Appl. Phys. Lett.* **20**, 71 (1972).

5. S. Strite and H. Morkoç. "GaN, AlN, and InN: a review." *J. Vac. Sci. Tech. B* **10**, 1237 (1992).

6. T. Matsuoka, H. Tanaka, T.Sasaki, and A. Katsui. "Wide-gap semiconductor (In,Ga)N." *Inst. Phys. Conf. Ser. No 106: International Symposium on GaAs and Related Compounds*, p.141 (1989).

7. C.P. Foley and T.L. Tansley. "Optical band gap of indium nitride." *J. Appl. Phys.* **59**, 3241 (1986).

8. C.P. Foley and T.L. Tansley. "Pseudopotential band structure of indium nitride." *Phys. Rev. B* **33**, 1430 (1986).

9. V.V. Mamutin, V.A. Vekshin, V. Yu. Davydov, V.V. Ratnikov, T.V. Shubina, S.V. Ivanov, P.S. Kopev, M. Karlsteen, U. Söderwall, and M. Willander. "MBE growth of hexagonal InN films on sapphire with different initial growth stages." *Phys. Stat. Sol. (a)* **176**, 247 (1999).

10. J. Aderhold, V. Yu. Davydov, F. Felder, H. Klausing, D. Mistele, T. Rotter, O. Semchinova, J. Stemmer, and J. Graul. "InN thin films grown by metalorganic molecular beam epitaxy on sapphire substrates." *J. Crys. Gr.* **222**, 701 (2001).

11. V. Yu. Davydov, A.A. Klochikhin, R.P. Seisyan, V.V. Emtsev, S.V. Ivanov, F. Bechstedt, J. Furthmüller, H. Harima, A.V. Mudryi, J. Aderhold, O. Semchinova, and J. Graul. "Absorption of emission of hexagonal InN. Evidence of narrow fundamental band gap." *Phys. Stat. Sol. (b)* **229**, R1 (2002).

12. J. Wu, W. Walukiewicz, K.M. Yu, J.W. Ager III, E.E. Haller, H. Lu, W.J. Schaff, Y. Saito, and Y. Nanishi. "Unusual properties of the fundamental band gap of InN." *Appl. Phys. Lett.* **80**, 3967 (2002).

13. S. Nakamura, S. Pearton, and G. Fasol. *The Blue Laser Diode: The Complete Story*. Springer, Berlin (2000).

14. S.M. Bedair. “Indium-based nitride compounds.” *Semiconductors and Semimetals, Vol. 50*, Ch. 6. Academic Press, Inc. (1997).

15. S.M. Bedair, F.G. McIntosh, J.C. Roberts, E.L. Piner, K.S. Boutrous, N.A. El-Masry. “Growth and characterization of In-based nitride compounds.” *J. Crys. Gr.* **178**, 32 (1997).

16. T. Matsuoka, N. Yoshimoto, T. Sakaki, and A. Katsui. *J. Electron. Mat.* **21**, 157 (1992).

17. J. R. Arthur, Jr. “Interaction of Ga and $As_2$ Molecular Beams with GaAs Surfaces.” *J. Appl. Phys.* **39**, 4032 (1968).

18. A full derivation of this expression is given in Chapter 5.

19. B. Culshaw. *Smart Structures and Materials*, Ch. 3.4.1. Artech House, Inc., Boston (1996).

20. E.T. Yu, X.Z. Dang, P.M. Asbeck, S.S. Lau, and G.J. Sullivan. “Spontaneous and piezoelectric polarization effects in III-V nitride heterostructures.” *J. Vac. Sci. Tech. B* **17**, 1742 (1999).

21. M.E. Aumer, S.F. LeBoeuf, B.F. Moody, and S.M. Bedair. “Strain-induced piezoelectric field effects on light emission energy and intensity from AlInGaN/InGaN quantum wells.” *Appl. Phys. Lett.* **79**, 3803 (2001).

22. D.A.B. Miller, D.S. Chemla, T.C. Damen, A.C Gossard, W. Wiegmann, T.H. Wood, and C.A. Burrus. “Band-edge electroabsorption in quantum well structures: the quantum-confined stark effect.” *Phys. Rev. Lett.* **53**, 2173 (1984).

23. J. Tersoff. “Enhanced nucleation and enrichment of strained-alloy quantum dots.” *Phys. Rev. Lett.* **81**, 3183 (1998).

24. Y.-S. Lin, K.-J. Ma, C. Hsu, S.-W. Feng, Y.-C. Cheng, C.-C. Liao, C.C. Yang, C.-C. Chou, C.-M. Lee, and J.-I. Chyi. “Dependence of composition fluctuation on indium content in InGaN/GaN multiple quantum wells.” *Appl. Phys. Lett.* **77**, 2988 (2000).

25. Yu. G. Musikhin, D. Gerthsen, D.A. Bedarev, N.A. Bert, W.V. Lundin, A.F. Tsatsul'nikov, A.V. Sakharov, A.S. Usikov, Zh. I. Alferov, I.L. Krestnikov, N.N. Ledentsov, A. Hoffman, and D. Bimberg. "Influence of metalorganic chemical vapor deposition growth conditions on In-rich nanoisland formation in InGaN/GaN structures." *Appl. Phys. Lett.* **80**, 2099 (2002).

26. S. Chichibu, T. Azuhata, T. Sota, and S. Nakamura. "Spontaneous emission of localized excitons in InGan single and multiquantum well structures." *Appl. Phys. Lett.* **69**, 4188 (1996).

27. I. Ho and G.B. Stringfellow. "Solid phase immiscibility in GaInN." *Appl. Phys. Lett.* **69**, 2701 (1996).

28. T.D. Moustakas. "Growth of wide-bandgap nitride semiconductors by MBE." in *Gallium-Nitride-based Technologies,* p. 1. M. Osiński, ed. SPIE Optical Engineering Press, Bellingham, WA (2002).

29. F.A. Ponce, S. Srinivasan, A. Bell, L. Geng, R. Liu, M. Stevens, J. Cai, H. Omiya, H. Marui, and S. Tanaka. "Microstructure and electronic properties of InGaN alloys." *Phys. Stat. Sol. (b)* **240**, 273 (2003).

30. N.A. El-Masry, E.L. Piner, S.X. Liu, and S.M. Bedair. "Phase separation in InGaN grown by metalorganic vapor phase deposition." *Appl. Phys. Lett.* **72**, 40 (1998).

31. M.K. Behbehani, E.L. Piner, S.X. Liu, N.A. El-Masry and S.M. Bedair. "Phase separation and ordering coexisting in $In_xGa_{1-x}N$ grown by metal organic chemical vapor deposition." *Appl. Phys. Lett.* **75**, 2202 (1999).

32. J.W. Cahn. "Spinodal decomposition." *Trans. of the Metall. Soc. Of AIME* **242**, 166 (1968).

33. C.C. Koch. MSE 706 class notes. North Carolina State University (2001).

34. S. Yu. Karpov. "Suppression of phase separation in InGaN due to elastic strain." *MRS Internet J. Nitride Semicond. Res.* **3**, 16 (1998).

35. E.L. Piner, M.K. Behbehani, N.A. El-Masry, F.G. McIntosh, J.C. Roberts, K.S. Boutros, and S.M. Bedair. "Effect of hydrogen on the indium incorporation in InGaN epitaxial films." *Appl. Phys. Lett.* **70**, 461 (1996).

36. B.D. Cullity. *Elements of X-Ray Diffraction.* Addison Wesley Publishing Company, Inc., Reading MA (1978).

37. K. Jacobs, B. Van Daele, M.R. Leys, I. Moerman, and G. Van Tendeloo. "Effect of growth interrupt and growth rate on MOVPE-grown InGaN/GaN MQW structures." *J. Crys. Gr.* **248**, 498 (2003).

38. B. Van Daele, G. Van Tendeloo, K. Jacobs, I. Moerman, and M.R. Leys. "Formation of metallic In in InGaN/GaN multiquantum wells." *Appl. Phys. Lett.* **85**, 4379 (2004).

39. F.E. Arkun. Personal communication. North Carolina State University (2004).

# 5.0 Mathematical Calculation of InGaN Emission

## 5.1 Preliminary Considerations

The bandgap (and corresponding emission wavelength) of an InGaN/GaN quantum well structure is dependent upon two primary factors: indium content (x) and well width ($L_{well}$). These two variables, in turn, control the major physical parameters that determine the effective bandgap of the structure (i.e., strain, quantum size effect, and quantum-confined Stark effect). All of these factors have been analyzed in detail and worked into a series of established equations. The resultant calculations can be used to estimate the bandgap/emission wavelength for a given heterostructure based on indium content and well width.

The following assumptions were made when carrying out these calculations:

- All structures are Type I heterostructures
- All structures are held at ambient temperature and pressure
- All material is Ga-polar
- The band offset ($\Delta E_V/\Delta E_C$) is assumed to be 0.7/0.3, as per ref. [1]
- InGaN wells are fully strained and pseudomorphic to GaN barriers. There is no partial relaxation.
- The only source of strain in the structures is due to lattice mismatch. Localized strain due to defects and strain due to differences in thermal expansion coefficient are not considered. Thus, the strain can be calculated using the simple expression $\varepsilon_{xx} = -\left|\frac{a_{InGaN} - a_{GaN}}{a_{GaN}}\right|$ (Eq. 5.1).

- The InGaN wells are compositionally uniform up to x=0.40. It is assumed that this is below the threshold of spinodal phase transformation. Realistically, this indium content is a bit high for this assumption, but this overestimation of the critical concentration will provide a more complete picture.
- The effects of band-tailing due to InGaN nanoislands (as discussed in Section 4.4.2) are not considered.

Another important assumption was that the material constants of InGaN are compositionally dependent and can be linearly interpolated using reported values [2,3,4] of GaN and InN as endpoints. The endpoint values and corresponding linear equations are given in Table 5.1.

Table 5.1 Material constants for GaN, InN, and InGaN

| Material constant | GaN value | InN value | InGaN value (x) |
|---|---|---|---|
| Elastic constant $C_{11}$ (GPa) | 367 | 223 | -144x + 367 |
| Elastic constant $C_{12}$ (GPa) | 135 | 115 | -20x + 135 |
| Elastic constant $C_{13}$ (GPa) | 103 | 92 | -11x + 103 |
| Elastic constant $C_{33}$ (GPa) | 405 | 224 | -181x + 405 |
| Piezoelectric constant $d_{31}$ (m/V) | $-1.7\text{x}10^{-12}$ | $-1.1\text{x}10^{-12}$ | $(0.6x – 1.7)\text{x}10^{-12}$ |
| Relative dielectric constant $\varepsilon_r$ | 15.3 | 8.9 | 6.4x + 8.9 |
| Electron effective mass (kg) | $0.2m_0$ | $0.11m_0$ | $(-0.09x + 0.2)m_0$ |
| Hole effective mass (kg) | $0.8m_0$ | $0.5m_0$ | $(-0.3x + 0.8)m_0$ |

## 5.2 Bandgap Calculation of Bulk InGaN

The analysis starts by assuming a bulk InGaN sample pseudomorphically strained to a GaN template. In this case, there is only one independent variable (x, indium content) and the parameters dealing with quantum confinement (quantum size effect, quantum-confined Stokes shift) can be neglected. Therefore the bandgap can be expressed simply by the fundamental expression [5]:

$$E_g^{InGaN} = E_g^{GaN}(1-x) + E_g^{InN}x - bx(1-x) \text{ eV} \qquad \text{(Eq. 5.2)}$$

where x is the indium content of the sample, b is the bowing parameter, $E_g^{GaN}$ is the bandgap of of GaN (3.4eV) and $E_g^{InN}$ is the bandgap of InN pseudomorphically strained to GaN. Bear in mind that the InN bandgap value given in Chapter 4 ( $E_g^{InN}$ = 0.7 eV) is representative of *relaxed* material, and therefore not appropriate for this particular formulation. The proper value, i.e., that which represents *strained* InN, is calculated by the expression [6]:

$$E_g^{InN} = 3.478 + 15.4\varepsilon_{zz} \text{ eV} \qquad \text{(Eq. 5.3)}$$

where $\varepsilon_{zz} = -2C_{13}/C_{33}$. This results in $E_g^{InN}$ = 1.71 eV.

Reported values for the bowing parameter of InGaN vary quite widely, generally falling in the range of 1.0 to 3.42 eV. One of the possible reasons for this scatter is the uncertainty in determining Poisson's ratio, υ, for InGaN. It has been shown that by normalizing υ to 0.17 and re-calculating published data, a more consistent value for

bowing parameter value can be obtained (b = 2.1 - 2.6 ev) [7]. Also, there is some evidence to suggest that the bowing parameter is dependent on the composition range [8]. For these calculations, b will be assumed to be constant and equal to 2.5 eV, as reported in ref. [7].

Strain also plays a role in determining the bandgap of InGaN, assuming the film has not reached its critical layer thickness. The amount of strain present can be calculated using Eq. 5.1, where $a_{GaN}$ is the lattice parameter of the GaN template and $a_{InGaN}$ is the lattice parameter of the InGaN film. This model assumes Vegard's Law is valid for $0 < x < 0.4$, so the InGaN lattice parameter for any In composition can be calculated by linear interpolation using the values [9] of $a_{GaN}$ (3.189 Å) and $a_{InN}$ (3.544 Å) as endpoints. The resulting expression in given as:

$$a_{InGaN}(x)=0.355x + 3.189 \text{ Å}. \qquad \text{(Eq. 5.4)}$$

The change in bandgap due to strain can then be calculated by the expression [6]:

$$\Delta E_g = -14.755\varepsilon_{xx} - 51.148\varepsilon_{xx}^2 \text{ eV} \qquad \text{(Eq. 5.5)}$$

A plot outlining the bandgap (and emission wavelength) for bulk InGaN is given in Figure 5.1. The solid line gives the values for a strained InGaN layer, while the dotted line gives the values for a relaxed film (i.e., neglecting Eq. 5.5).

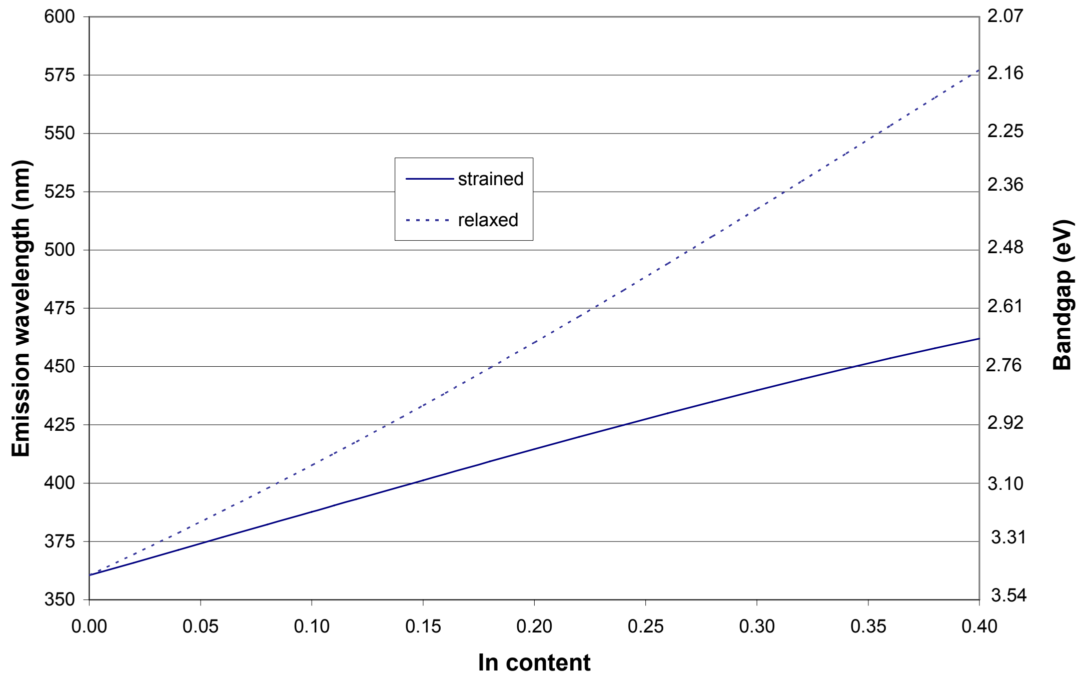


Figure 5.1 Emission wavelength vs. indium content for relaxed and strained InGaN

As can be seen by the plot, the blueshift which arises due to the strain component is sizable. Also, notice that it is not possible to achieve emission greater than 462 nm ($E_g < 2.68$ eV) in a bulk layer within the specified composition range. This demonstrates that quantum effects are necessary if green (510 nm) to red (650 nm) emission is to be seen in InGaN-based structures.

### 5.3 Calculation of the Quantum Size Effect in InGaN/GaN Quantum Wells

As mentioned in section 4.1, the quantization of energy states within a double heterostructure leads to an increase in the effective bandgap of the structure. This is known as the quantum size effect (QSE). Precise calculation of the QSE involves solving

the corresponding Schrödinger equation, whose solution is in the form of the Kronig-Penney equation (KPE) [10]:

$$\cos qd = \cos(2k_A a)\cos(2k_B b) - \tfrac{1}{2}(\alpha + 1/\alpha)\sin(2k_A a)\cos(2k_B b) \qquad \text{(Eq. 5.6)}$$

where:

$$k_A = i\sqrt{2m_A(E - V_0)/\hbar^2} \qquad \text{(Eq. 5.7)}$$

$$k_B = \sqrt{2m_B E/\hbar^2} \qquad \text{(Eq. 5.8)}$$

a is $L_{barrier}/2$, b is $L_{well}/2$, $m_A$ is the effective carrier mass in the barrier, $m_B$ is the effective carrier mass in the well, $V_0$ is the band offset, and E is the quantized energy level.

A recent publication by Szmulowicz [11] offers a convenient formulation of the KPE which will be used in this model to calculate $\Delta E_g$ due to the quantum size effect. In this technique, the determinant of the 2x2 equation resulting from the boundary conditions of the wavefunction is expressed in the tangents-only form:

$$D_{sz} = [\tan(k_B b) + \tanh(k_A a)/\beta] * [\tan(k_B b) - \beta \tanh(k_A a)] \qquad \text{(Eq. 5.9)}$$

where

$$\beta = \frac{m_B k_A}{m_A k_B}. \qquad \text{(Eq. 5.10)}$$

This determinant can then by multiplied by $\cos^2(k_B b)$ (to eliminate the singularities due to the tangents) and plotted vs. E for the conduction or valence band of a given quantum well structure with a fixed indium concentration, well width, and barrier width (for simplification, $L_{barrier}$ will be assumed to be 2* $L_{well}$). The points at which the

$D_{sz}\cos^2(k_B b)$ curve crosses the x-axis represent the quantized energy states n=1, 2, 3 etc. If calculated to a high enough x-value, the curve will display a singularity at $E=V_0$.

An example of a series of Kronig-Penney/Szmulowicz plots is given in Figure 5.2 for a quantum well structure with constant In content (0.16) and varying $L_{well}$. Plots (a) and (b) give the results for conduction band calculations and valence band calculations, respectively. (Note the singularity for each conduction band curve at $x = V_0 = 86$ meV). Table 5.2 then lists the values of the quantized energy values taken from each curve.

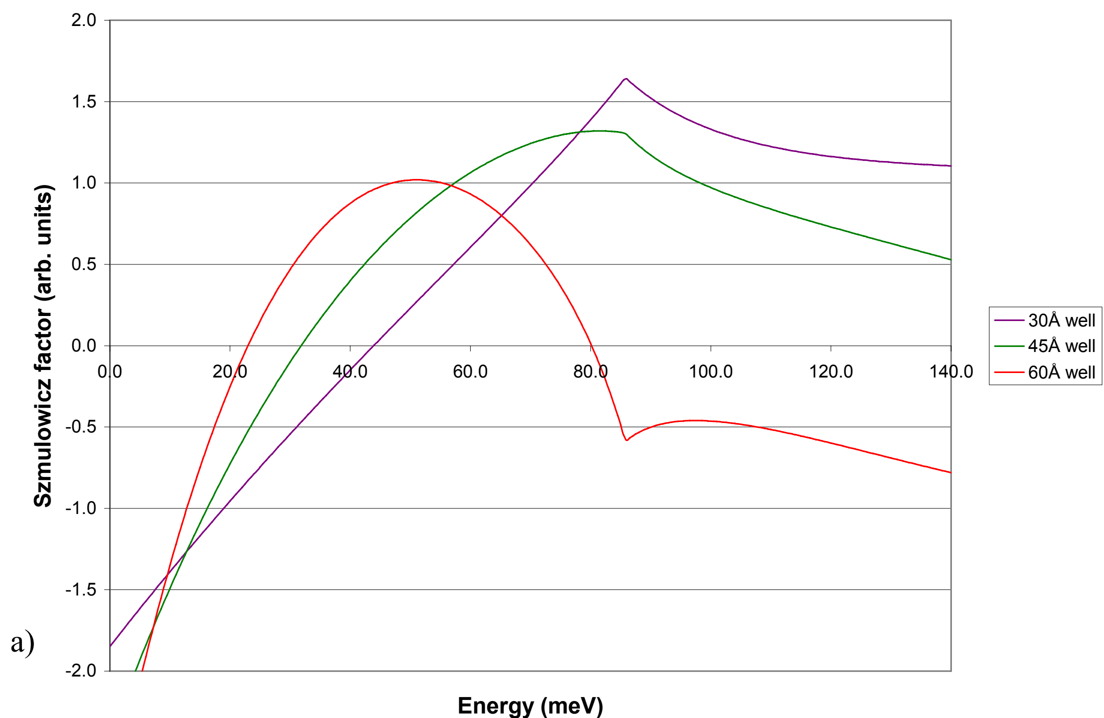


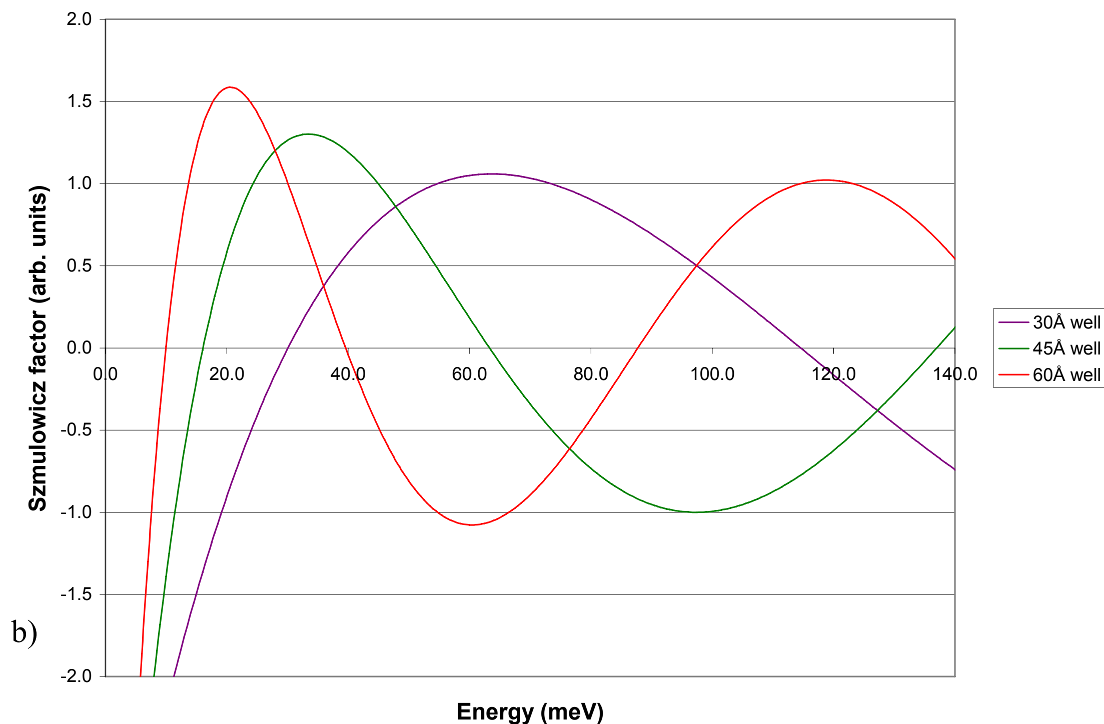


Figure 5.2 Calculation of the Szmulowicz formulation of the Kronig-Penney model for a 16% InGaN/GaN QW structure for (a) the conduction band and (b) the valence band

Table 5.2 Quantized energy levels within a 16% InGaN/GaN QW structure, as calculated by the Szmulowicz formulation of the Kronig-Penney model

| | Conduction band energy levels (meV) | | Valence band energy levels (meV) | | |
|---|---|---|---|---|---|
| | $E_{C1}$ | $E_{C2}$ | $E_{V1}$ | $E_{V2}$ | $E_{V3}$ |
| 30Å | 44 | -- | 30 | 115 | -- |
| 45Å | 32 | -- | 16 | 63 | 137 |
| 60Å | 23 | 80 | 10 | 40 | 88 |

Such a series of plots was made for every In composition from x = 0 to x = 0.40 at 0.02 intervals with well thicknesses from 30 - 60Å at 5 Å intervals. It was thus possible to calculate the bandgap shift due to the quantum effect for a series of well widths and In composition, assuming $E_{C1}$ - $E_{V1}$ transitions. The results are given in Figure 5.3.

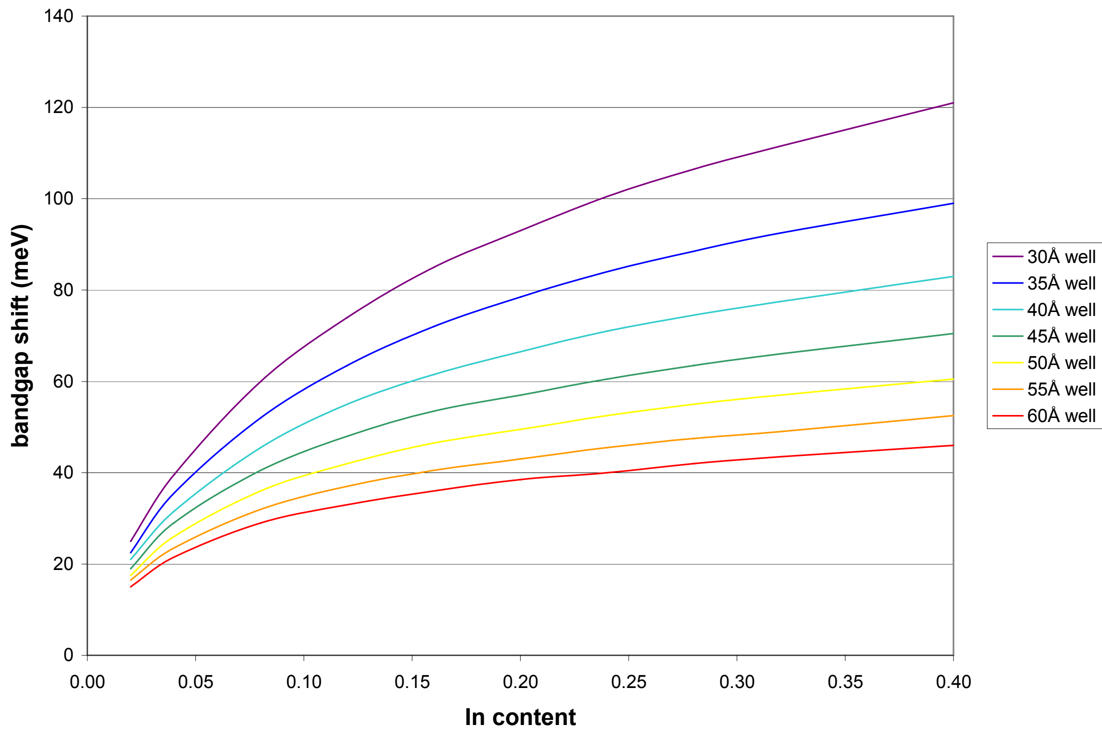


Figure 5.3 Bandgap shift due to quantum size effect vs. In content for various length quantum wells

As can be seen in the figure, shorter well widths lead to more severe $\Delta E_g$ due to the quantum size effect. This is to be expected, as per the basic particle-in-a-box equation discussed in Section 4.1. Also, $\Delta E_g$ increases along with In concentration. This is due an increase in well depth as In content gets higher.

It is also important to note the magnitude of $\Delta E_g$ due to QSE. Generally speaking, $\Delta E_{g,QSE}$ is quite small—less than 100 meV in most cases. This translates to a variation of ≤6% for InGaN/GaN structures emitting in the visible range.

### 5.4 Calculation of the Polarization fields in InGaN/GaN quantum wells

As discussed in Sections 3.4 and 4.4, there exists in InGaN an electric field due to polarization. There are two components to this field: spontaneous polarization due to the lack on inversion symmetry in the wurtzite crystal, and piezoelectric polarization which arises due to strain. The electrical field of each component, and subsequently the total electric field will be calculated.

The spontaneous polarization values of GaN and InN are, respectively, -0.029 $C/m^2$ and –0.032 $C/m^2$ [12]. The corresponding value of $In_xGa_{1-x}N$ will be assumed to be a linear interpolation of the two. This means that the spontaneous polarization values in the $In_xGa_{1-x}N$ well will exhibit a gradient from that of the GaN barrier for x>0. This gradient will lead to an electric field which can be calculated by the expression:

$$F_{sp} = -0.03x/\varepsilon_r\varepsilon_0 \text{ V/m} \qquad \text{(Eq. 5.11)}$$

These values will be negative, as the electric field due to spontaneous polarization points toward the substrate in Ga-polar material[13].

The calculation of the second component, the electric field due to the piezoelectric effect, is given by the expression [14]:

$$F_{pz,z} = {}^{2d_{31}\left(C_{11}+C_{12}-\frac{2C_{13}^2}{C_{33}}\right)\varepsilon_{xx}}\Big/_{\varepsilon_0\varepsilon_r} \quad \text{V/m} \qquad \text{(Eq. 5.12)}$$

where $C_{11}$, $C_{12}$, $C_{13}$, and $C_{33}$ are the elastic stiffness constants, $\varepsilon_{xx}$ is the strain in the layer, $\varepsilon_r$ is the relative dielectric constant, and $d_{31}$ is the piezoelectric coefficient relating the strain in the x-y plane to the electric field in the z-direction. The values for the electric field due to the piezoelectric effect will be positive, as this electric field points away from the substrate [13].

Figure 5.4 plots the values of electric field due to spontaneous polarization and piezoelectric polarization, as well as the sum of the two, as a function of indium composition.

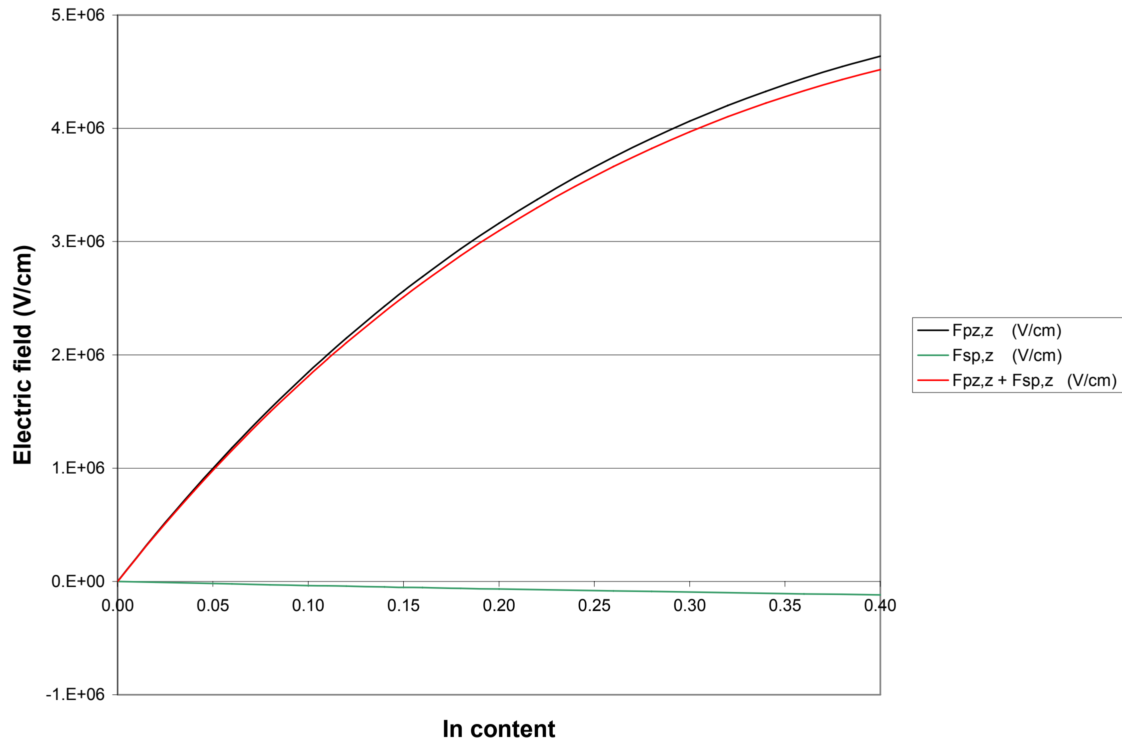


Figure 5.4 Electric field [from both spontaneous and piezoelectric polarization] vs. In content

These calculations show that the electric field due to spontaneous polarization is negligible in comparison to the electric field caused by the piezoelectric effect. This is because strain values, which are a factor in the piezoelectric polarization field calculations, are exceptionally high in InGaN. This, of course, is a direct result of the high degree of lattice mismatch between GaN and InN. On the other hand, the difference in spontaneous polarization between GaN and InN is small, leading to relatively insignificant values of spontaneous polarization field.

### 5.5 Effect of Polarization Fields on the Bandgap of InGaN/GaN Quantum Wells

As discussed in Section 4.4.1, the large electric fields present in InGaN/GaN double heterostructures lead to significant band bending. This bending causes the conduction band minimum to be energetically closer to the valence band maximum, thus effectively reducing the bandgap. This phenomenon is known as the quantum-confined Stark effect.

The amount by which the bandgap shifts due to an internal electrical field is given by the expression [15]:

$$\Delta E_{g,QCSE} = \frac{15-\pi^2}{24\pi^4}\frac{\left(m_e^* + m_h^*\right)q^2 F^2 L_{eff}^4}{\hbar^2} \qquad \text{(Eq. 5.13)}$$

where $m_e^*$ and $m_h^*$ are the effective electron and hole masses, $L_{eff}$ is the well width, and F is the electric field. Note the exceptionally strong (power of 4) effect well width has on the bandgap shift.

Eq. 5.13 can be combined with this chapter's previous equations to give an overall expression bandgap . This equation will taken the general form:

$$\begin{aligned} E_g^{InGaN} &= E_g^{GaN}(1-x) + E_g^{InN}x - bx(1-x) \\ &+ \Delta E_{g,strain} + \Delta E_{g,QSE} - \Delta E_{g,QCSE} \end{aligned} \qquad \text{(Eq. 5.14)}$$

Substitution of the relevant expression yields:

$$
\begin{aligned}
E_g^{InGaN} &= 3.4(1-x) + (3.478 + 15.4\varepsilon_{zz})x - bx(1-x) \\
&- 14.755\,\varepsilon_{xx} - 51.148\,\varepsilon_{xx}^2 + \Delta E_{g,QSE} - \\
&\frac{15-\pi^2}{24\pi^4}\frac{\left(m_e^* + m_h^*\right)q^2 L_{eff}^4}{\hbar^2} * \\
&\left[\frac{-0.03x}{\varepsilon_r\varepsilon_0} + \frac{2d_{31}(C_{11} + C_{12} - {2C_{13}^2}/{C_{33}})\varepsilon_{xx}}{\varepsilon_r\varepsilon_0}\right]^2
\end{aligned}
\qquad \text{(Eq. 5.15)}
$$

Eq. 5.15 gives an expression for the bandgap of InGaN that is dependent only upon well width, indium content, and indium-content dependent material constants. Using this expression the emission wavelength as a function of indium content can be determined for an InGaN/GaN double heterostructure with a given well width. The results of this series of calculations are shown in Figure 5.5.

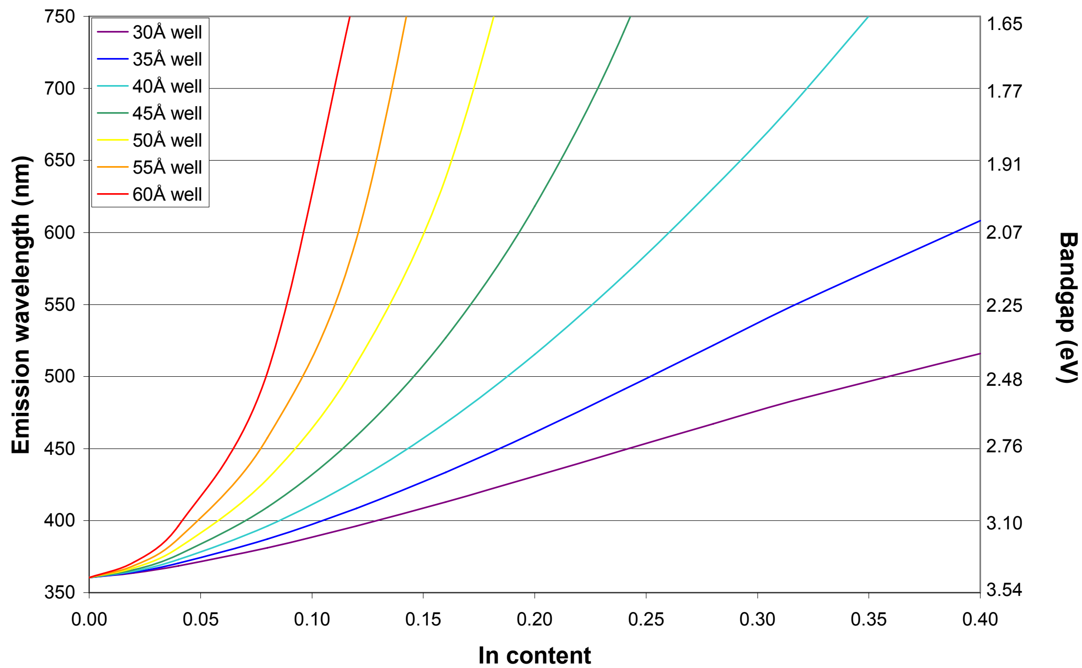


Figure 5.5 Emission wavelength vs. In content for various length quantum wells

### 5.6 Difficulties in the Use of Wide Quantum Wells in InGaN/GaN Structures

Figure 5.5 provides a visual representation of how strongly the piezoelectric polarization redshifts the emission of an InGaN/GaN quantum well structure. From this diagram, one could infer that double heterostructures with wide quantum well widths could, with relative ease, provide devices in the 550-700 nm range and beyond. However, there are other factors that arise when using wide quantum wells which make their prospects less appealing.

The first issue to consider is that of the critical layer thickness (CLT). The CLT is the thickness threshold beyond which a strained film relaxes through the formation of misfit dislocations [16]. This process degrades the quality of the material and, in the case of InGaN, reduces the piezoelectric polarization necessary to obtain the desired redshift.

An estimate of the CLT of III-V compounds can be obtained from the Matthews-Blakeslee model [17]. This model expresses CLT as a function of strain, and has been shown to be fairly accurate in the case of InGaAs/GaAs structures [18]. Applying this model to InGaN/GaN results in a CLT values of ~ 30Å for very high (x = 0.40) In content material, increasing to 200-400Å for material in the $0.05<x<0.10$ range.

Although the CLT's for low In content material predicted by Matthews-Blakeslee are larger than the well widths explored in the present model, the values do not differ greatly. Bearing in mind the error expected in each model, it is reasonable to expect that wide quantum wells will approach, or possibly reach, the critical layer thickness, particularly for higher In concentrations. Also, because the wells are bound on both sides, the actual CLT value is likely to be less than that predicted by Matthews-Blakeslee.

This issue is even more severe when dealing with a multiple-quantum well (MQW) structure. In this case, the overall strain in the structure builds with each successive well [19]. Thus, the individual CLT for each InGaN layer will be lower, and the wells will be more susceptible to relaxation.

A second major problem with wider wells (independent of CLT) is related to the piezoelectric polarization. As mentioned previously, the piezoelectric polarization within the material leads to band-bending which causes a decrease in effective bandgap of the well. Another consequence of this band-bending is the spatial separation of the electron and hole envelope functions (see Figure 5.6), leading to decreased overlap.

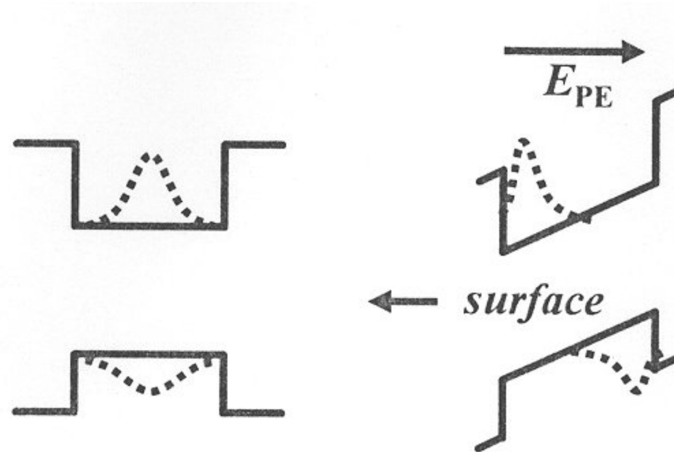


Figure 5.6 Electron and hole envelope functions for (a) an unstrained quantum well, and (b) a compressively strained quantum well [20]

This separation means that the overlap between the two wavefunctions will be reduced as compared to the flat-band scenario. If the well width is increased, the envelope functions will get pushed further apart, thereby reducing the overlap even more. This phenomenon is important to consider because, according to Fermi's Golden Rule, wavefunction overlap is proportional, by a power of two, to transition probability [21]. The transition probability in an LED structure is equivalent to its internal quantum efficiency (IQE) [22]. Thus, the IQE of a quantum well structure will be greatly reduced in structures in which the electron and hole envelope function have a large separation. For this reason, in the few cases where red InGaN-based structures are reported [23,24,25], the emission is so weak that any such devices would have little practical use.

Experimental evidence of the reduced emission from wider quantum wells is given in Figure 5.7. These PL spectra are taken from the centers of two wedge-shaped samples grown at $T_{well}/T_{barrier}$ = 700ºC/750ºC and capped at 950ºC. The only difference between the two is well width: the more intense sample had a QW growth time of 60 sec

($d_{well} \approx 35$Å), while the QW growth time of the weaker sample was 75 sec ($d_{well} \approx 44$ Å). Moreover, the increased well thickness did not lead to an appreciable wavelength shift, which is likely due to the onset of relaxation.

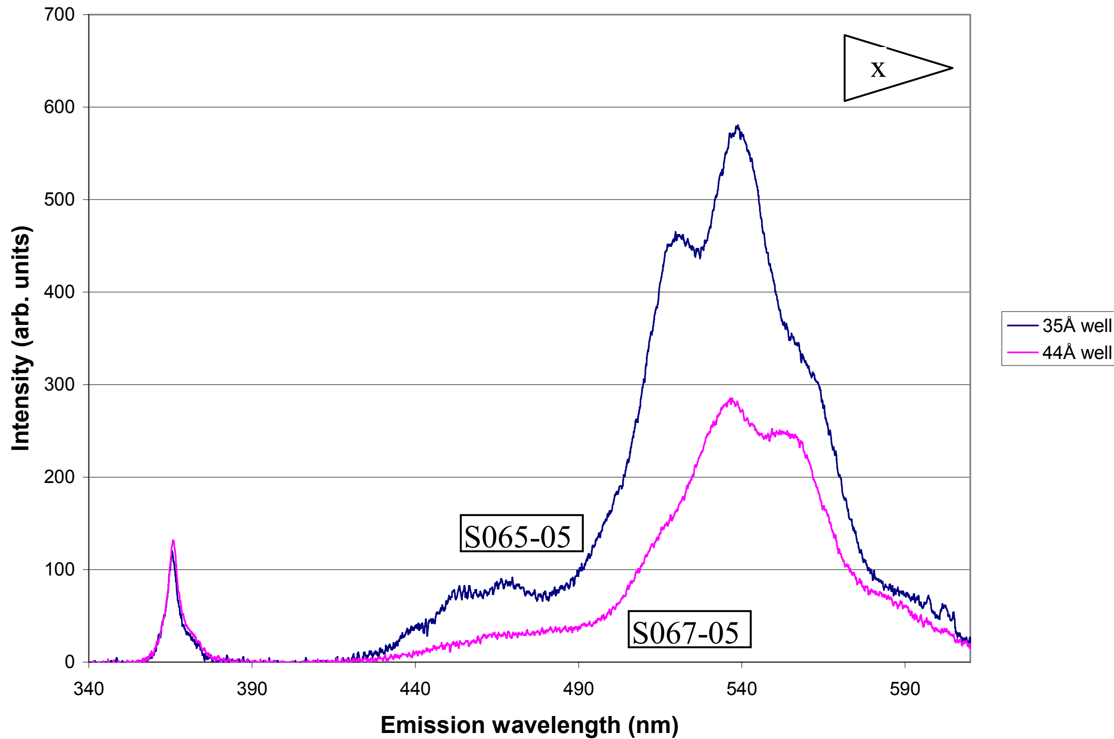


Figure 5.7 Comparison of emission spectra of 35Å and 44Å quantum-well structures

This section outlines one of the major dilemmas involved with the use of InGaN/GaN quantum well structures for long-wavelength ($\lambda \geq 550$nm) light-emitting diodes. On one hand, it has been shown that piezoelectric polarization is necessary to shift the InGaN bandgap into the appropriate range. This is best achieved by growing longer quantum wells. However, the piezoelectric effect also works to decrease the efficiency of double heterostructures, a problem which is exacerbated by wider wells. Longer wells also can also lead to partial relaxation as the InGaN regions approach their

critical layer thickness. This issue of well width is an obstacle which is seriously hampering emergence of InGaN-based yellow to red and monolithic white LED's.

### 5.7 Application to Experimental Data

The calculations summarized in Figure 5.5 can be quite useful in the study of InGaN-based LED structures. For example, they can be used to provide an estimate of the In content of given InGaN/GaN structures. Since the measurement of alloy composition in MQW structures is not straightforward, experimentation is often carried out without knowing its values. However, one may use the above plots (Figure 5.5 in particular) to estimate the In content of a given structure, assuming well width and emission wavelength are known.

This exercise is carried out below for the range of capped InGaN/GaN structures presented in Figure 4.16 and Table 4.2. Emission wavelengths have been measured by PL, and well width has been estimated based on a growth rate of 30 Å/min (calculated in Section 4.5.4). These values are given in Table 5.3, along with the estimated In content taken from Figure 5.5.

Table 5.3 Estimated In content for the structures shown in Figure 4.16

| Emission wavelength (nm) | Well/barrier growth temperature (ºC) | Estimated well thickness (Å) | **Estimated In content (%)** |
|---|---|---|---|
| 413 | 760/760 | 45 | **8** |
| 445 | 743/743 | 45 | **11** |
| 474 | 730/730 | 38 | **18** |
| 499 | 708/725 | 30 | **35** |
| 539 | 708/725 | 38 | **24** |
| 561 | 701/725 | 38 | **27** |

In five out of six cases, Figure 5.5 yields very reasonable values of In content. The exception is the very large value (35%) estimated for the 499nm structure. The exact reason for this anomaly is not clear; perhaps this series of calculations becomes less valid as QW width is reduced. Regardless, Figure 5.5 appears to give, in cases where $38Å < d < 45Å$, a reasonable approximation of In content for MQW structures emitting in the violet to near-yellow spectral range.

## 5.8 References

1. J. Piprek, R.K. Sink, M.A. Hansen, J.E. Bowers, and S.P. DenBaars. "Simulation and optimization of 420 nm InGaN laser diodes." *Physics and Simulation of Optoelectronic Devices VIII.* R. Binder, P. Blood & M. Osinki, eds. SPIE Proc. 3944 (2000).

2. A.F. Wright. "Elastic Properties of zinc-blende and wurtzite AlN, GaN, and InN." *J. App. Phys.* **82**, 2833 (1997)

3. R.D. Underwood, P. Kozody, S. Keller, S.P. DenBaars, and U.K. Mishra. "Piezoelectric surface barrier lowering applied to InGaN/GaN field emitter arrays." *App. Phys. Lett.* **73**, 405 (1998).

4. Ioffe Physico-Technical Institute electronic archive: Physical properties of semiconductors. Found online at http://www.ioffe.rssi.ru/SVA/NSM/Semicond/index.html.

5. C.A. Parker, J.C. Roberts, S.M. Bedair, M.J. Reed, S.X. Liu, N.A. El-Masry, and L.H. Robins. "Optical band gap dependence on composition and thickness of $In_xGa_{1-x}N$ ($0<x<0.25$) grown on GaN." *Appl. Phys. Lett.* **75,** 2566 (1999).

6. T. Azuhata, T. Sota, S. Chichibu, A. Kuramata, K. Horino, M. Yagamuchi, T. Yagi, and S. Nakamura. "Valence band physics in wurtzite GaN." *Materials Research Society Proceedings Vol. 468: Gallium Nitride and Related Materials II*, p.445 (1997).

7. S. Stepanov, W.N. Wang, B.S. Yavich, V. Bougrov, Y.T. Rebane, and Y.G. Shreter. "Influence of Poisson's ratio uncertainty on calculations of the bowing parameter for strained InGaN layers." MRS Internet J. Nitride Semicond. Res. 6, 6 (2001).

8. M.D. McCluskey, C.G. Van de Walle, C.P. Master, L.T. Romano, and N.M. Johnson. "Large band gap bowing of $In_xGa_{1-x}N$ alloys." *Appl. Phys. Lett*. **72**, 2725 (1998).

9. S. Nakamura, S. Pearton, and G. Fasol. *The Blue Laser Diode: The Complete Story*, Chapter 3.2.1. Springer, Berlin (2000).

10. R. de L. Kronig and W.G. Penney. "Quantum mechanics of electrons in crystal lattices." *Proc. R. Soc. A* **130**, 499 (1931).

11. F. Szmulowicz. "Kronig-Penney model: a new solution." *Eur. J. Phys.* **18**, 392 (1997).

12. F. Bernardini, V. Fiorentini, and D. Vanderbilt. "Spontaneous polarization and piezoelectric constants of III-V nitrides." *Phys. Rev. B.* **56**, R10024 (1997).

13. E.T. Yu, X.Z. Dang, P.M. Asbeck, S.S. Lau, and G.J. Sullivan. "Spontaneous and piezoelectric polarization effects in III-V nitride heterostructures." *J. Vac. Sci. Tech. B* **17**, 1742 (1999).

14. A. Bykhovski, B. Gelmont, and M.Shur. "The influence of the strain-induced electric field on the charge distribution in GaN-AlN-GaN structure." *J. Appl. Phys.* **74**, 6734 (1993).

15. S.L. Chuang. *Physics of Optoelectronic Devices*, Chap. 13.4.6. John Wiley & Sons, New York (1995).

16. M. Ohring. *The Materials Science of Thin Films*, Chapter 7.3.1. Academic Press, San Diego (1992).

17. J.W. Matthews and A.E. Blakeslee. "Defects in epitaxial multilayers." *J. Crys. Gr.* **27**, 118 (1974).

18. I.J. Fritz, S.T. Picraux, L.R. Dawson, T.J. Drummond, W.D. Laidig, and N.G. Anderson. "Dependence of critical layer thickness on strain for $In_xGa_{1-x}As$/GaAs strained-layer superlattices." *Appl. Phys. Lett.* **46**, 967 (1985).

19. S.J. Chang, W.C. Lai, Y.K. Su, J.F. Chen, C.H. Liu, U.H. Liaw. "InGaN—GaN Multiquantum-well blue and green light emitting diodes." *IEEE J. on Selected Topics in Quant. Elec*. **8**, 278 (2002).

20. M.E. Aumer. "Effects of strain on the optical properties of AlInGaN quaternary alloys and their heterostructures." Ph.D Thesis. North Carolina State University (2001).

21. J. Singh. *Physics of Semiconductors and Their Heterostructures*. McGraw-Hill, New York (1993).

22. E.F. Schubert. *Light-Emitting Diodes,* Chapter 2.8. Cambridge University Press, Cambridge (2003).

23. T. Mukai, M. Yamada, and S. Nakamura. "Characteristics of InGaN-based UV/blue/green/amber/red light-emitting diodes." *Jpn. J. Appl. Phys.* **38**, 3976 (1999).

24. B. Damilano, N. Grandjean, J. Massies, L. Siozade, and J. Leymarie. "InGaN/GaN quantum wells grown by molecular beam-epitaxy emitting from blue to red at 300K." *Appl. Phys. Lett.* **77**, 1268 (2000).

**25.** R.W. Martin, P.R. Edwards, R. Pecharroman-Gallego, C. Liu, C.J. Deatcher, I.M. Watson, and K.P. O'Donnell. "Light emission ranging from blue to red from a series of InGaN/GaN single quantum wells." *J. Phys. D.* **35**, 604 (2002).

# 6.0 Fabrication of InGaN-based Devices

## 6.1 LED Structures

Nitride-based monochromatic LED's, particularly in the UV-green range of the spectrum, have been exhaustively researched [1-5] and are fixtures in the lighting market. However, the technology of nitride-based white LED's is still in a nascent state. In addition to the growth-related issues discussed in the previous chapters, there are a number of questions regarding how to structure the devices themselves in order to obtain white emission the most efficiently.

### *6.1.1 RGB structure*

The most straightforward way to generate white light is through the mixture of blue ($\lambda \sim 470$ nm), green ($\lambda \sim 540$ nm), and red ($\lambda \sim 610$ nm) emission. Each color individually stimulates one of the three types of cone cells (blue, green, and red) found in the human eye. When these three colors are blended in the proper intensity ratio, the resultant light will be perceived as white by a typical human observer. Quantitatively speaking, such a mixture will fall at (x,y) = (0.3128, 0.3292) on the CIE chromaticity diagram (see Figure 6.1). This point is defined as CIE Illuminant $D_{65}$ and is typically used as a white light reference [6].

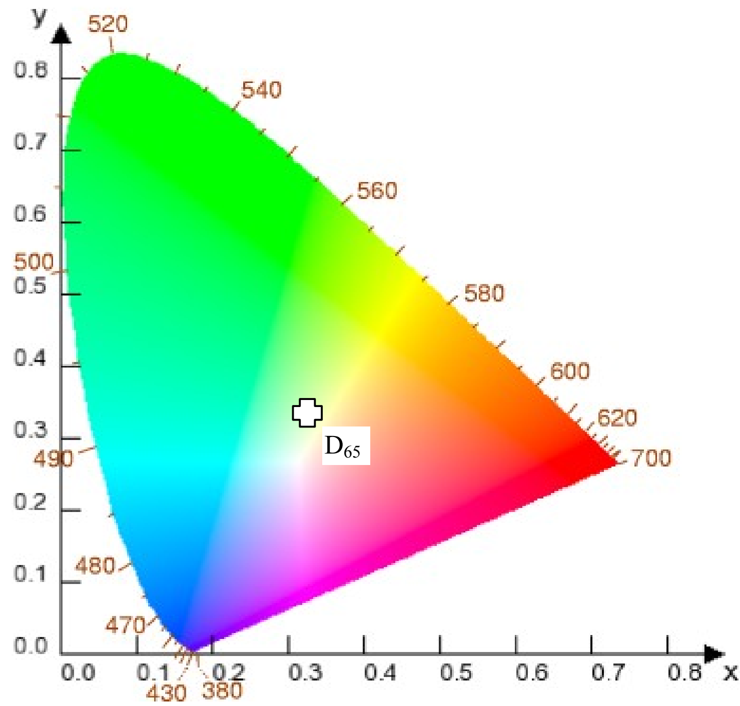

Figure 6.1 CIE Chromaticity diagram [7] showing Illuminant $D_{65}$

Determination of the intensity ratio necessary to achieve emission at a desired point (in this case, Illuminant $D_{65}$) is a fairly straightforward process. Generally speaking, for a mixture of three wavelengths ($\lambda_1$, $\lambda_2$, $\lambda_3$):

$$L_1 = \bar{x}(\lambda_1)P_1 + \bar{y}(\lambda_1)P_1 + \bar{z}(\lambda_1)P_1 \qquad \text{(Eq. 6.1)}$$

$$L_2 = \bar{x}(\lambda_2)P_2 + \bar{y}(\lambda_2)P_2 + \bar{z}(\lambda_2)P_2 \qquad \text{(Eq. 6.2)}$$

$$L_3 = \bar{x}(\lambda_3)P_3 + \bar{y}(\lambda_3)P_3 + \bar{z}(\lambda_3)P_3 \qquad \text{(Eq. 6.3)}$$

where $P_1$, $P_2$, and $P_3$ are the relative power values for each of the three individual wavelengths and $\bar{x}(\lambda)$, $\bar{y}(\lambda)$, and $\bar{z}(\lambda)$ are dimensionless quantities known as the color

matching functions (see below). The quantity $L_i$ has no physical significance in and of itself; it is merely used as an abbreviation for the quantities given in the above equations.

The color matching functions are used to quantify the sensitivity each type of cone cell in the human eye to a given wavelength. They are designated $\bar{x}$, $\bar{y}$, and $\bar{z}$; and correspond to the sensitivity of red, green and blue cone cells, respectively. A diagram showing the 1931 and 1978 version of these functions is given in Figure 6.2. [Note: The 1978 values will be used in the present analysis.]

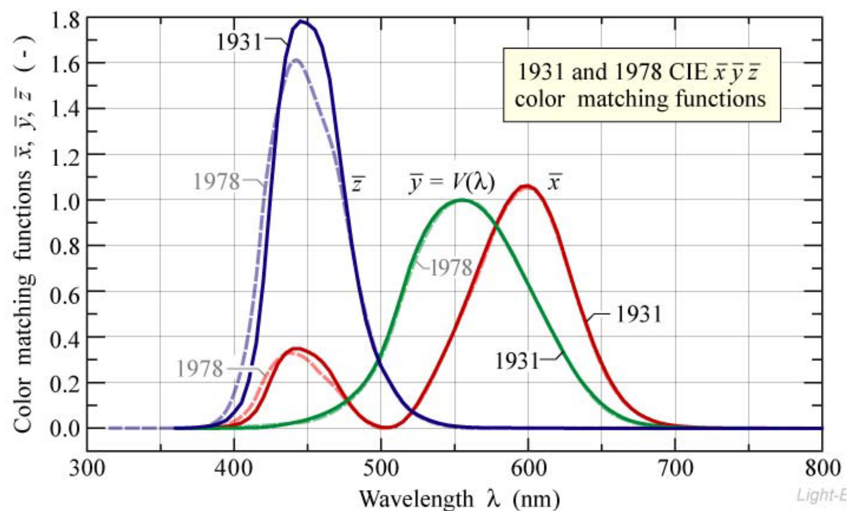


Figure 6.2 CIE Color-matching functions from 1931 and 1978 [6]

The purpose of the color-matching functions can be explained as follows. Assume, for example, a light source emitting at 450nm. At this wavelength, a typical human's blue cones will be approximately 4X as sensitive as his/her red cone cells. His/her green cone cells will hardly be able to detect the light at all. On the other hand, for emission at 600nm, red cone cell sensitivity is at its maximum, green cone cell sensitivity is ~60% of its maximum, and blue cone sensitivity is zero.

These color-matching functions are used when calculating Equations 6.1-6.3, as cone cell sensitivity information is critical in determining what mixture will be perceived as white by a human observer. The standard values of $\bar{x}$, $\bar{y}$, and $\bar{z}$ for a set of given wavelengths can be estimated graphically using Figure 6.2, or found tabulated in a typical color science reference text, such as ref. 6 or ref. 8.

Once the $L_i$ values for a given set of wavelengths and intensities are calculated (Eq. 6.1-6.3), the chromaticity coordinates describing the resultant color mix can be calculated using the following expressions:

$$x = \frac{x_1 L_1 + x_2 L_2 + x_3 L_3}{L_1 + L_2 + L_3} \qquad \text{(Eq. 6.4)}$$

$$y = \frac{y_1 L_1 + y_2 L_2 + y_3 L_3}{L_1 + L_2 + L_3} \qquad \text{(Eq. 6.5)}$$

Using the above equations, one can calculate the power ratios necessary in order to yield RGB emission at Illuminant $D_{65}$. To begin, determine the proper emission wavelength ($\lambda$) and chromaticity coordinates (x,y) for each of the three monochromatic components. For the present exercise, the typical values for LED's emitting in the red ($\lambda$ = 615nm, x = 0.68, y = 0.32), green ($\lambda$ = 520nm, x = 0.13, y = 0.72), and blue ($\lambda$ = 475nm, x = 0.12, y = 0.12) will be taken from ref. 6. This reference will also provide the color-matching functions ($\bar{x}$, $\bar{y}$, $\bar{z}$) for each component.

Once these values are known, one can select the desired chromaticity point (in this case, (x,y) = (0.3128, 0.3292); i.e., Illuminant $D_{65}$), then use an iterative process to

calculate the relative power values necessary to achieve the desired chromaticity point. In order for typical red, green, and blue LED's to mix and achieve Illuminant $D_{65}$, the blue emission must be the strongest, with green at 19.0% of the blue's intensity and the red at 20.2% of the blue's intensity (see Table 6.1).

Table 6.1 Calculation of relative power necessary to obtain white light from an RGB mixture

| λ (nm) | x | Y | $\bar{x}$ | $\bar{y}$ | $\bar{z}$ | **Relative Power** | $L_i$ |
|---|---|---|---|---|---|---|---|
| 475 | 0.12 | 0.12 | 0.142 | 0.113 | 1.042 | 1 | 1.297 |
| 520 | 0.13 | 0.72 | 0.063 | 0.710 | 0.078 | 0.190 | 0.1612 |
| 615 | 0.68 | 0.32 | 0.938 | 0.441 | 0.000 | 0.202 | 0.2787 |

These values are consistent with what one would expect, based on the human eye response curve (Figure 1.2). Whereas 520nm and 615nm have nearly equal sensitivity values, the corresponding value for 475nm is much less. Thus, in an RGB structure, much more blue intensity is needed in order for a typical human observer to perceive white.

If an RGB approach is to be used to create GaN-based white LED's, the structure shown in Figure 6.3 can potentially be used.

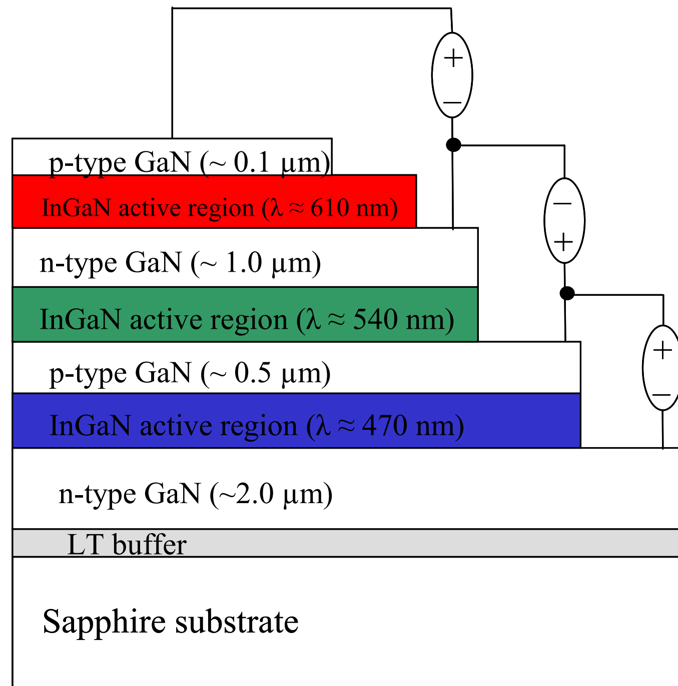


Figure 6.3 White LED structure using red, green, and blue active regions

A novel aspect of this proposed structure is the presence of four terminals. With such a set-up, one can independently provide power to each active region. This is advantageous for two reasons. First, by having such control over each color, one can readily obtain the necessary power ratios given in Table 6.1. This would be far more difficult with a single-source device.

The second advantage for the four-terminal structure is long-term device stability. As the LED ages (or even experiences temperature fluctuations) the photon flux from each active region will drift slightly from its initial value. This drift will lead to a corresponding shift in the color coordinates of each individual color region. The size of the shift will not be consistent from color to color, as shown by Figure 6.4.

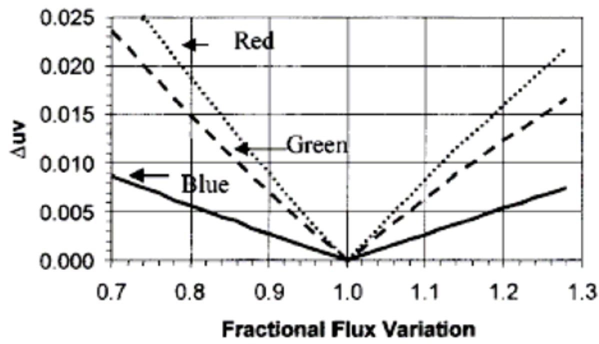


Figure 6.4 Change in color coordinates vs. fractional flux variation [9]

In the above graph, the y-axis represents the change in color coordinates while the x-axis shows the *fractional* variation of photon flux (i.e., a value of 1.0 means no change in initial flux). The plot shows a substantial difference between the flux-related color-coordinate change in blue as compared to that of green and especially red.

This color-dependence of the flux-related coordinate shift means that an RGB LED powered by a single supply will exhibit significant drift in correlated color temperature (CCT) as it ages. However, if the device allows for independent control of each active region (as in Figure 6.3), this drift can be accounted for by adjusting the power ratios, thus keeping the flux (and subsequently the color coordinates and CCT) at a constant level.

Generation of white light using the color mixture described above will give a color rendering index, $R_a$, of 80+ [9]. Such a value is acceptable for indoor home and office lighting. Therefore, the structure shown in Figure 6.3 appears to be ideal for white-light applications. However, the growth of this structure is not a trivial matter. As shown experimentally in Chapter 4 and mathematically in Chapter 5, achieving red emission from InGaN-based material is a challenging task. Additionally, even if

emission with λ ≥ 600 nm is obtained, it is unlikely to emit with sufficient efficiency as to be usable in a white-light structure.

*6.1.2 Complementary wavelength structure*

Because of the difficulties currently faced with the growth of red-emitting InGaN, it may be beneficial to consider other potential white light sources; particularly ones in which only require emission wavelengths <600 nm. One such example is the two-color structure shown in Figure 6.5.

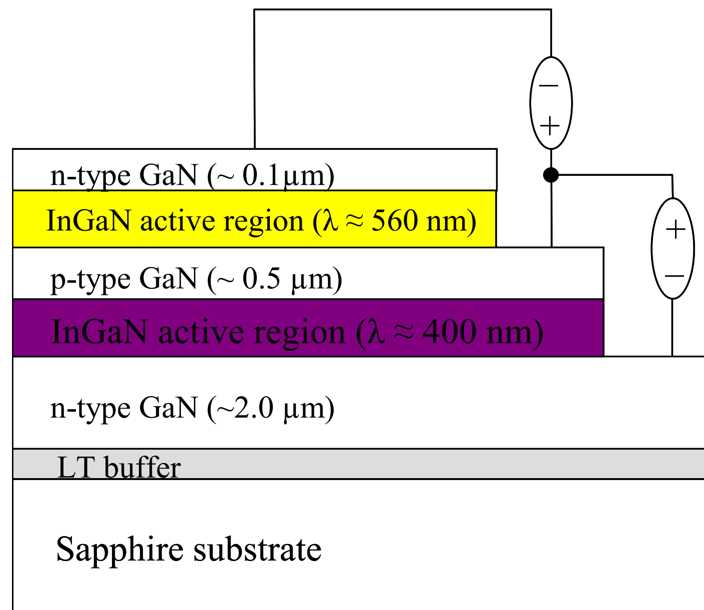


Figure 6.5 White LED structure using violet and yellow active regions

This device structure features two independently-powered active regions which emit at approximately 400 nm and 560 nm. These two wavelengths are known to be complementary, meaning that they can be mixed to yield an overall emission which gives the perception of white light; i.e. a chromaticity point at Illuminant $D_{65}$ [6, 10]. A table of complementary wavelengths, along with the appropriate power ratios, is given in Table

6.2. Figure 6.6 shows the CIE chromaticity diagram with two complementary point yielding white emission at Illuminant $D_{65}$.

Table 6.2 Complementary wavelengths and corresponding power ratios [6,10]

| **Complementary wavelengths** | | **Power ratio** |
|---|---|---|
| $\lambda_1$ (nm) | $\lambda_2$ (nm) | $P(\lambda_2)/P(\lambda_1)$ |
| 380 | 560.9 | 0.000642 |
| 390 | 560.9 | 0.00955 |
| 400 | 561.1 | 0.0785 |
| 410 | 561.3 | 0.356 |
| 420 | 561.7 | 0.891 |
| 430 | 562.2 | 1.42 |
| 440 | 562.9 | 1.79 |
| 450 | 564.0 | 1.79 |
| 460 | 565.9 | 1.53 |
| 470 | 570.4 | 1.09 |
| 475 | 575.5 | 0.812 |

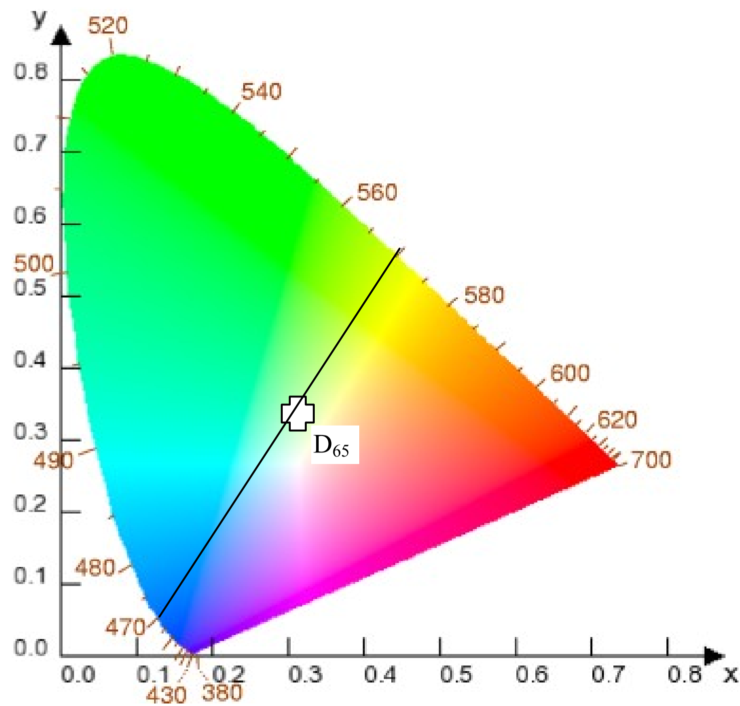


Figure 6.6 CIE chromaticity diagram showing two complementary wavelengths combining to make white light at Illuminant $D_{65}$

The two-color structure shown in Figure 6.4 has an advantage over the aforementioned RGB structure because it does not require an InGaN-based red emission layer. In fact, the maximum wavelength necessary, 561 nm, was successfully achieved and presented in Figures 4.16 and 4.21. Therefore, it appears possible to grow such a device structure using the TSS-CCS.

The major drawback to the two-color complementary-wavelength device is its poor color rendering index. Expected $R_a$ values are in the 30-40 range [9], which is insufficient for home or office use. However, this low $R_a$ value is still acceptable for some applications, such as outdoor lighting or displays.

## 6.2 Monochromatic LED Fabrication

### *6.2.1 Fabrication overview*

Based on the data presented in Chapters 3 and 4, it appears possible to grow the two-color white LED structure shown in Figure 6.5. First, however, it would be feasible to fabricate monochromatic devices emitting in the desired blue and yellow ranges. However, because short-wavelength InGaN based LED's are very well-established, our efforts were focused almost solely on the growth of longer-wavelength structures. Indeed, there have been few reports of InGaN-based devices in the emitting in the yellow spectral range [10, 12, 13], and none using Al-free MQW's grown by MOCVD.

All device structures were simple *p-i-n* diodes, as shown in Figure 4.8. The *i*-layer consisted of the MQW active region as well as the LT cap. Fabrication was carried out in the following manner:

1. Activation of p-type carriers. This was carried out by a 20 minute anneal at 735°C in an $N_2$ atmosphere.

2. Dehydration of the sample at 120°C for 5 minutes.

3. Application of Futurrex NR9-3000PY negative photoresist. This was carried out by a 5000 rpm spin using a Chemat Technology KW-4A spinner.

4. Soft bake at 150°C for 1 minute. This is to desorb any excess solvents that may come from the photoresist.

5. Mask alignment using a Karl Suss MJB3 aligner. A square pattern negative mask was chosen; the goal of this step is to prepare the sample for a mesa etch.

6. Exposure at 17 $mW/cm^2$ for 17 seconds. This will cause the polymers in the exposed area to cross-link.

7. Post-exposure bake at 100°C for 1 minute.

8. Developer dip for 30 seconds. The un-cross-linked photoresist will be washed away.

9. Hydrochloric acid dip for 1 minute.

10. E-beam evaporation of a nickel etch mask. The mask was subsequently annealed at 400ºC for 3 seconds in an $N_2$ atmosphere.

11. Inductively coupled plasma (ICP) etch using a Trion Technology Minilock II etcher. ICP power = 260 W, $BCl_3/Cl_2$ flow = 5 sccm/30 sccm, etch rate = 1600 Å/min. At this point, a 9x9 matrix of mesas had been fabricated on the sample.

12. Repeat steps 1-8. This is in preparation for p-type metallization. The p-type contact will be a small square on top of the mesa.

13. E-beam evaporation of p-type contacts using a Thermionics vacuum system. Metallization scheme was 700Å Ni/700Å Au. Gold was chosen because its high work function will lead to low barrier to holes [13]. The Ni layer is a diffusion barrier, which necessary due to the high diffusivity of Au in GaN.

14. Anneal of p-type contact at 500ºC for 8 minutes in air.

15. Repeat steps 1-8. This in is preparation for n-type metallization. The n-type contact will be a ring that goes around the mesa, i.e. will be contacting the n-type material exposed by the mesa etch.

16. E-beam evaporation of n-type contacts using a Thermionics vacuum system. Metallization scheme was 200Å Ti/1500Å Al/300Å Ti/500Å Au. Aluminum was chosen because its low work function will lead to low barrier for electrons [14]. The Ti acts as both a wetting layer and a barrier to AlN formation.

*6.2.2 Fabrication of p-n junction*

In Chapter 3, Hall and PL data were given which verified successful n- and p-type doping of GaN. These measurement techniques are certainly valid; however, the true test of n- and p-type material is the demonstration of a rectifying junction between the two. Figure 6.7 shows the I-V characteristic of such a junction. This structure is composed of standard n-type GaN (n~$5 \times 10^{17}$ $cm^{-3}$) capped with a p-type layer grown at 950°C.

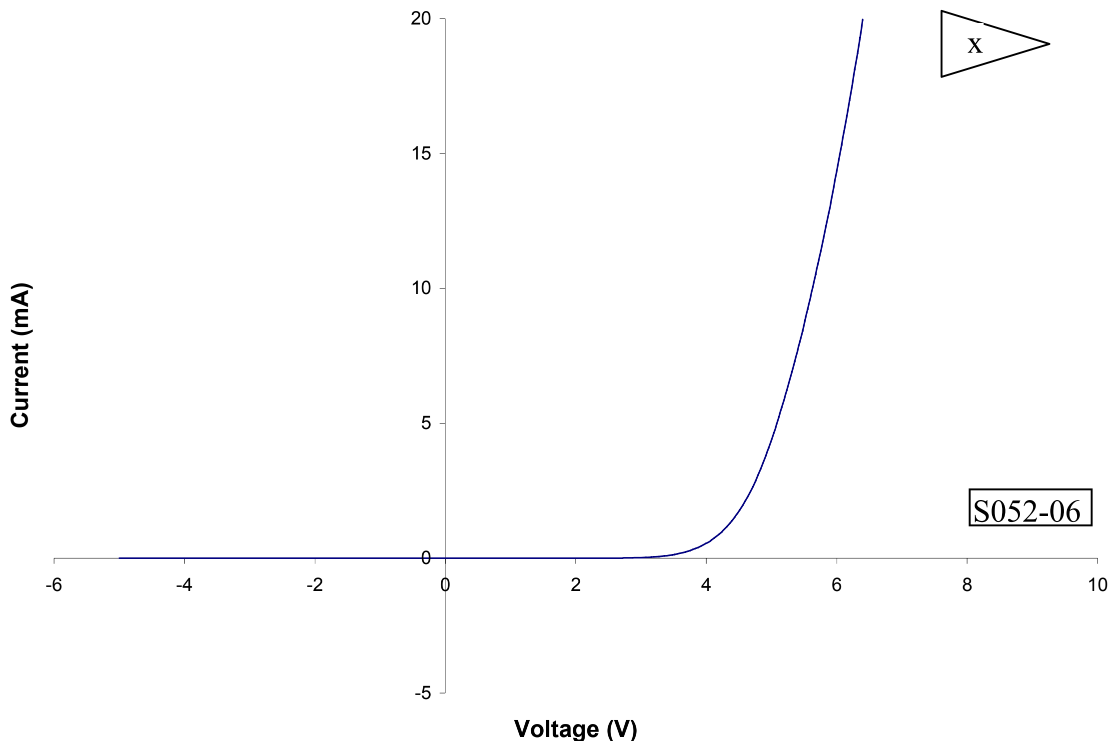


Figure 6.7 I-V characteristic of p-n junction

The observed rectifying behavior offers further confirmation that successful n- and p-type doping has been achieved.

From this I-V the ideality factor can be determined. It is calculated through the diode equation, which is given as:

$$I = I_0 e^{(qV/nkT)} - 1 \qquad \text{(Eq. 6.6)}$$

where n is the ideality factor. Assuming V>>kT (and, subsequently, $e^{(qV/nkT)}$>>1), Equation 6.6 can be re-written as:

$$\ln I = q(\frac{1}{nkT})V + \ln I_0 \qquad \text{(Eq. 6.7)}$$

Thus, the inverse of the slope of a ln I vs. V plot will yield an energy term, E, which can be divided by kT to obtain the ideality factor, n. Generally, low current data ($I<10^{-5}$A) are used in order to minimize device heating effects. The resultant plot for the p-n junction is given in Figure 6.8.

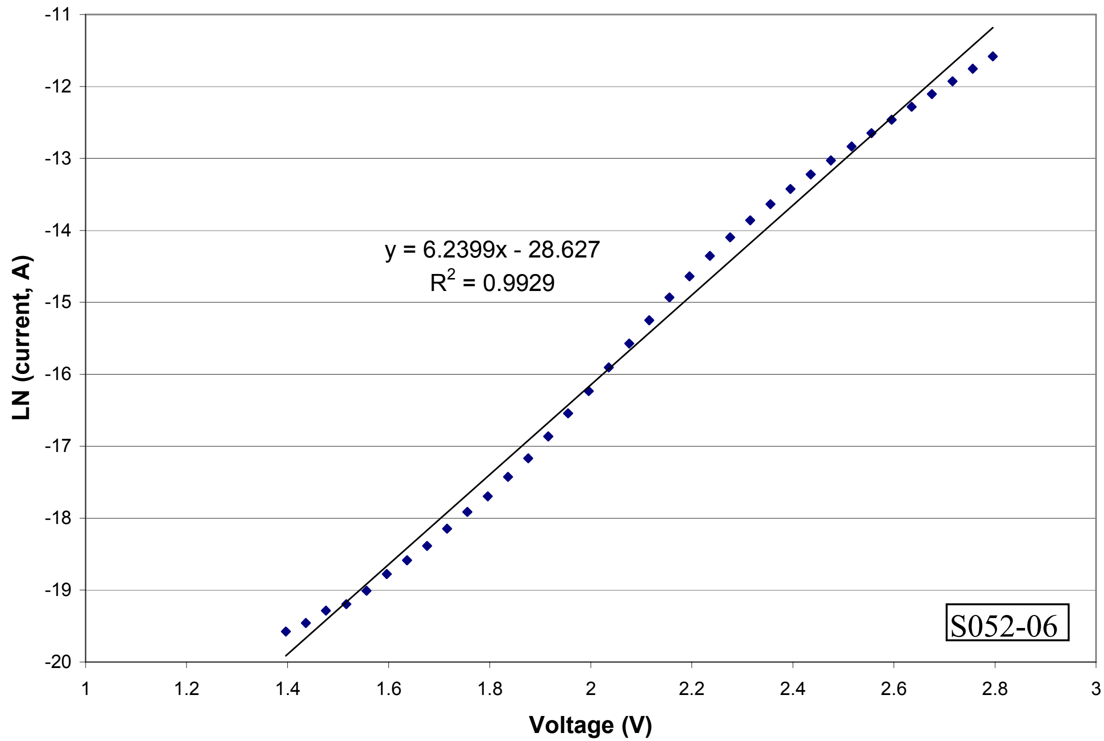


Figure 6.8 Ideality factor plot for p-n junction

For the given diode, E=160 meV, which results in an ideality factor of 6.2. This does not conform to the standard Sah-Noyce-Shockley model [15], which states the ideality factor must be between n=1 (diffusion-dominated) and n=2 (recombination-dominated). However, such seemingly anomalous ideality factors are commonly seen in GaN-based devices [16,17,18]. This behavior has been explained by Shah, *et. al.*[18], who theorize that the calculated ideality factor is actually the sum of the ideality factors of all rectifying junctions (metal/semiconductor junctions, unipolar heterojunctions, etc.) within the device.

*6.2.3 Fabrication of long-wavelength LED's*

The next step in the process was to mimic the p-n junction growth process with a long-wavelength InGaN/GaN MQW structure sandwiched between the n- and p-layers. This was done successfully on a wedge-shaped substrate grown with the following conditions, given in Table 6.3:

Table 6.3 Growth conditions of long-wavelength LED structure (S069-06)

| | | | |
|---|---|---|---|
| MQW structure growth temperature ($T_{well}/T_{barrier}$, °C) | 720/760 | Low-temperature (LT) cap growth temperature (°C) | 840 |
| MQW structure growth time ($t_{well}/t_{barrier}$, sec) | 60/270 | LT cap thickness (Å) | 440 |
| Number of wells | 4 | LT→HT ramp time (sec) | 526 |
| TMG flux (μmol/min) | 3.3 | P-type cap growth temperature (°C) | 950 |
| TMI flux (μmol/min) | 2.5 | P-type cap thickness (Å) | 2200 |

As discussed in Section 4.5.7, the InGaN/GaN structures grown for this study on wedge-shaped substrates exhibited a certain degree of nonuniformity. The sample grown under the above conditions was no different. Thus, after fabrication, the resultant wafer had two fairly distinct regions (tip and center), each containing a number of devices that behaved differently than those in the other region.

*6.2.4 Tip region – green devices*

The tip region yielded an area of green-emitting LED's. Electroluminescence was performed using a Keithley 2430 SourceMeter to supply power. An Ocean Optics HR2000 spectrometer was used to collect the spectra. Two sets of typical

electroluminescence spectra for these devices are shown in Figures 6.9 and 6.10, representing high injection current and low injection current, respectively.

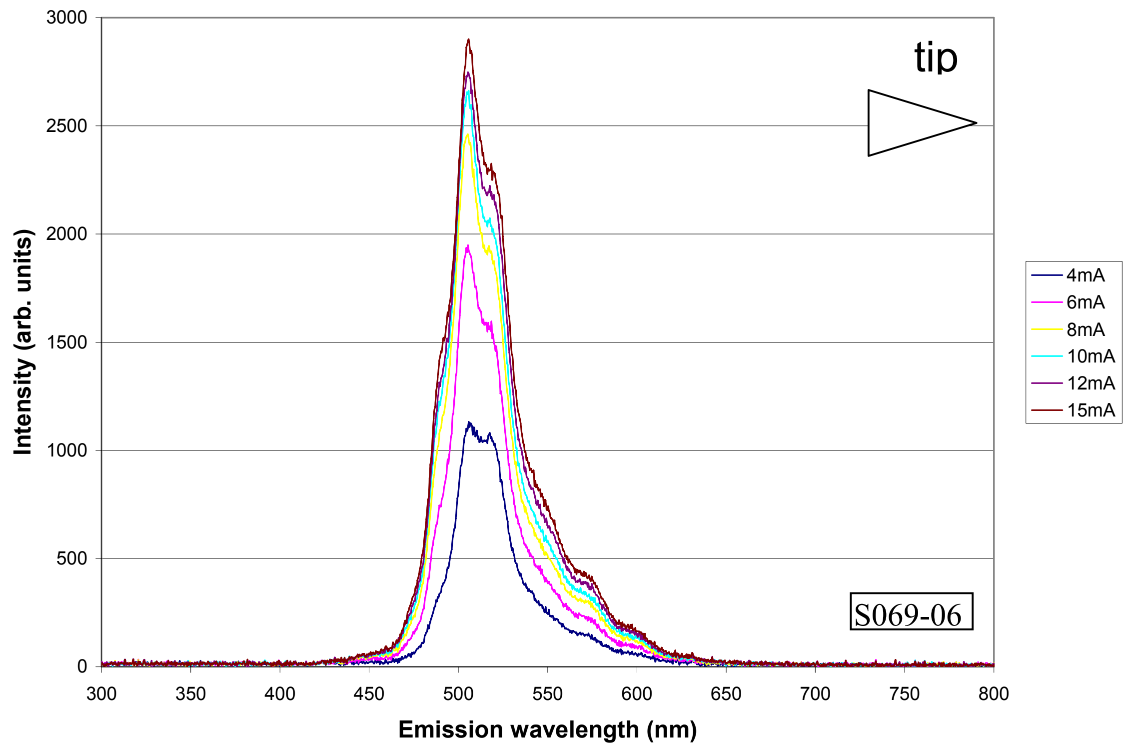


Figure 6.9 Electroluminescence spectra of green LED under high injection current

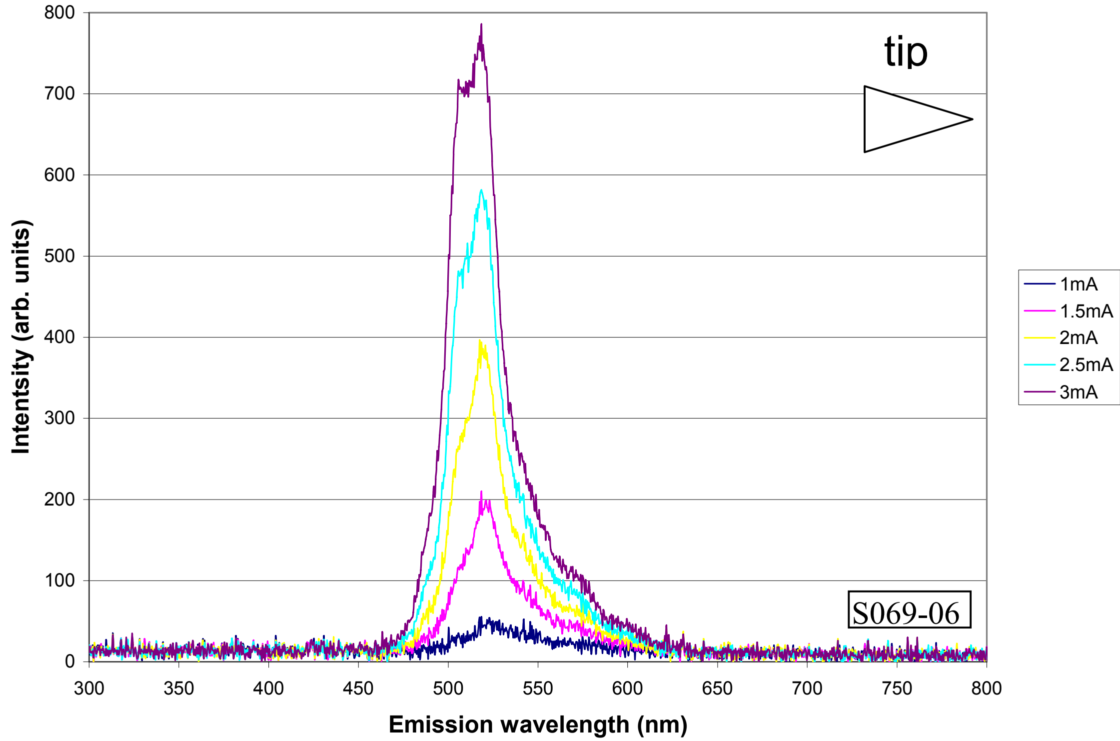


Figure 6.10 Electroluminescence spectra of green LED under low injection current

The devices were quite bright, visible from several yards even in the presence of ambient white lighting. At high injection currents (>4mA), the peak emission wavelength was measured at 506nm. A redshift was seen with decreasing current once a lower threshold current was reached (4mA). The emission wavelength shifted as long as 525nm at 1mA, below which emission is no longer visible. This phenomenon has been reported previously [12], and attributed to either screening of the piezoelectric field (thus reducing band bending); or band-filling, in which the lower energy states become completely filled with carriers and thus higher energy states are forced to become populated.

*6.2.5 Center region – yellow/amber devices*

In Section 4.5.7, data was presented showing a clear PL redshift from traveling from the tip to the center of the wedge. EL measurements exhibited the same effect; as devices in the center of the Table 6.3 sample emitted in the yellow (high injection current) and amber (low injection current) spectral ranges. These spectra are shown in Figures 6.11 and 6.12, respectively.

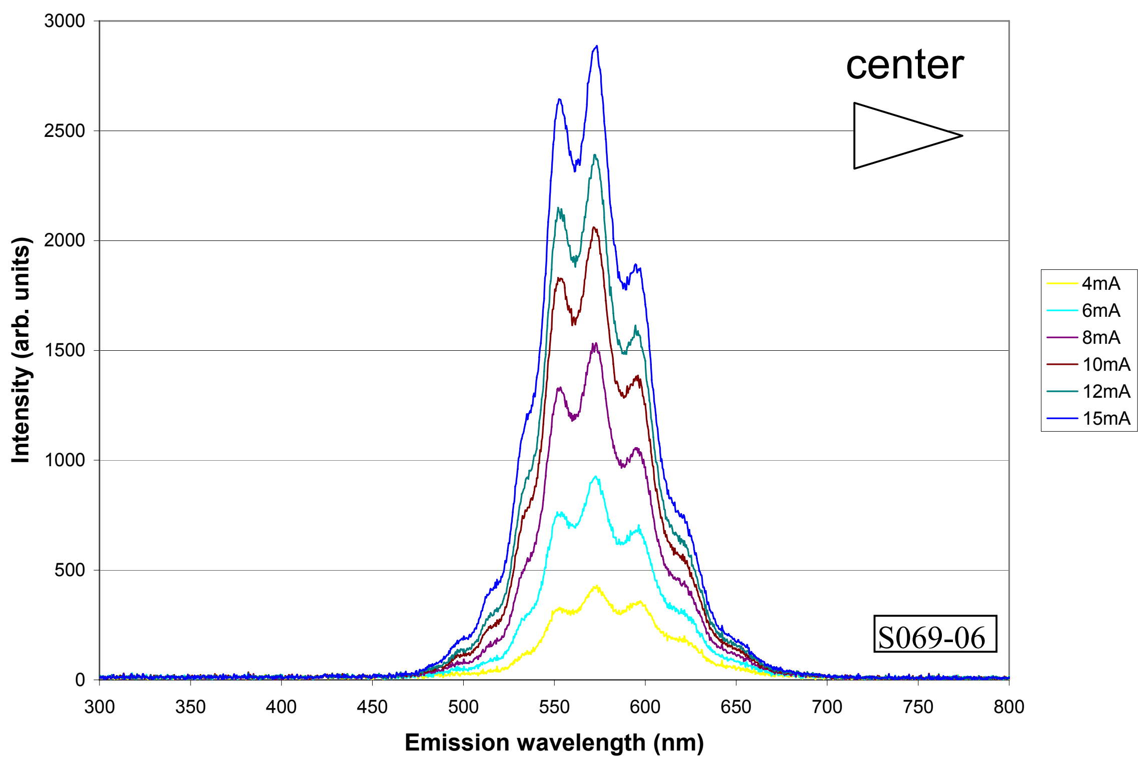


Figure 6.11 Electroluminescence spectra of yellow/amber LED under high injection current

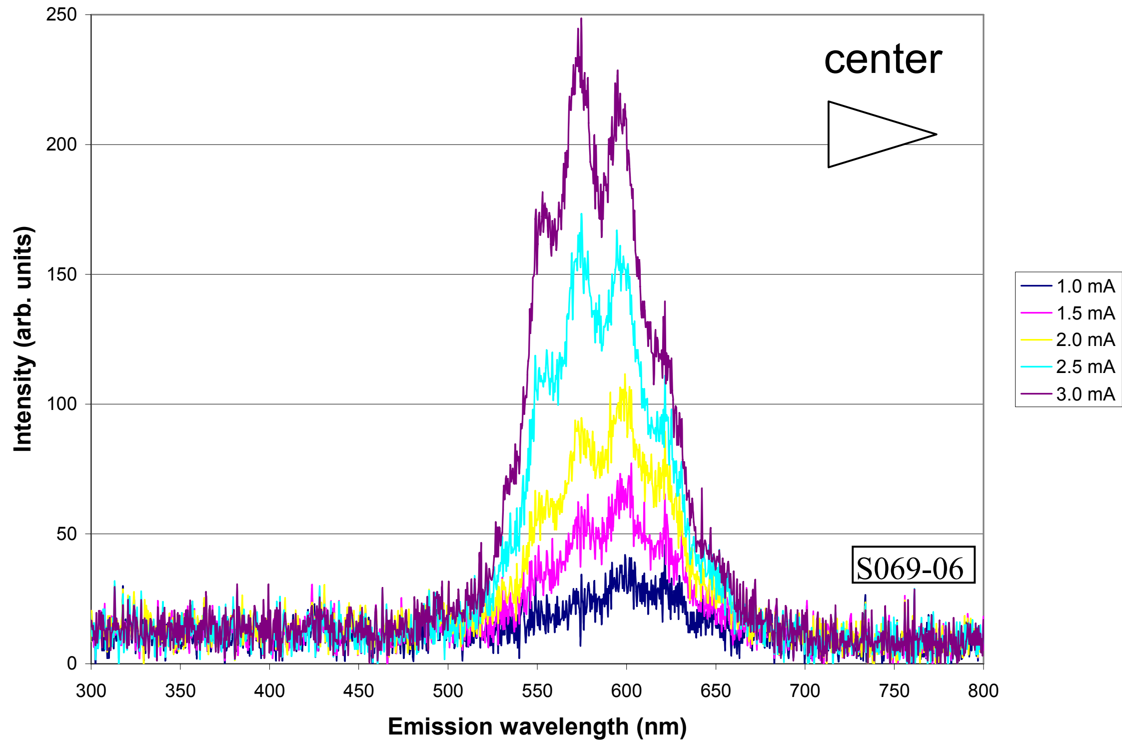


Figure 6.12 Electroluminescence spectra of yellow/amber LED under low injection current

The peak emission wavelength for these devices was 573nm at high injection currents. Like the aforementioned green diodes, the yellow LED's exhibited a red shift with decreasing current below 2mA. The emission wavelength reached a maximum of 601nm @ 1mA injection current.

Photographs of these surprisingly bright devices are shown in Figure 6.13.

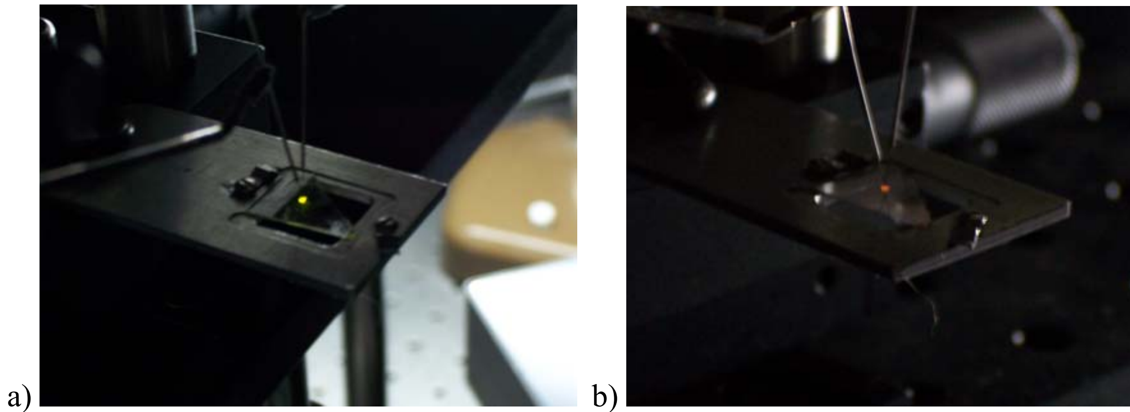

a) b)

Figure 6.13 Photographs of LED #S069-06 operating at (a)10 mA and (b) 2mA

As mentioned previously, there are very few published reports of InGaN-based LED's emitting in this wavelength range. Damilano, et. al., have reported wavelengths of 600 nm for MBE-grown devices [10]. Researchers at Nichia report EL emission in the 594-675 nm range for single-well devices with an AlGaN barrier [12, 13]. The data presented in this dissertation represents the longest reported emission wavelengths for Al-free InGaN/GaN multiple quantum-well LED's grown by MOCVD.

*6.2.6 Photoluminescence of yellow devices*

Photoluminescence was carried out on an unprocessed sample grown under similar conditions as those listed in Table 6.3 (i.e., yellow device conditions). The purpose of this study was to compare the emission spectra generated by laser excitation (PL) to that shown in Figures 6.11 and 6.12 for electrical excitation (EL). For the PL measurements, a series of neutral density (ND) filters was placed in the laser beam in an effort to study the effects of reduced excitation. This is roughly analogous to reducing the injection current when performing EL. These spectra are given in Figure 6.14.

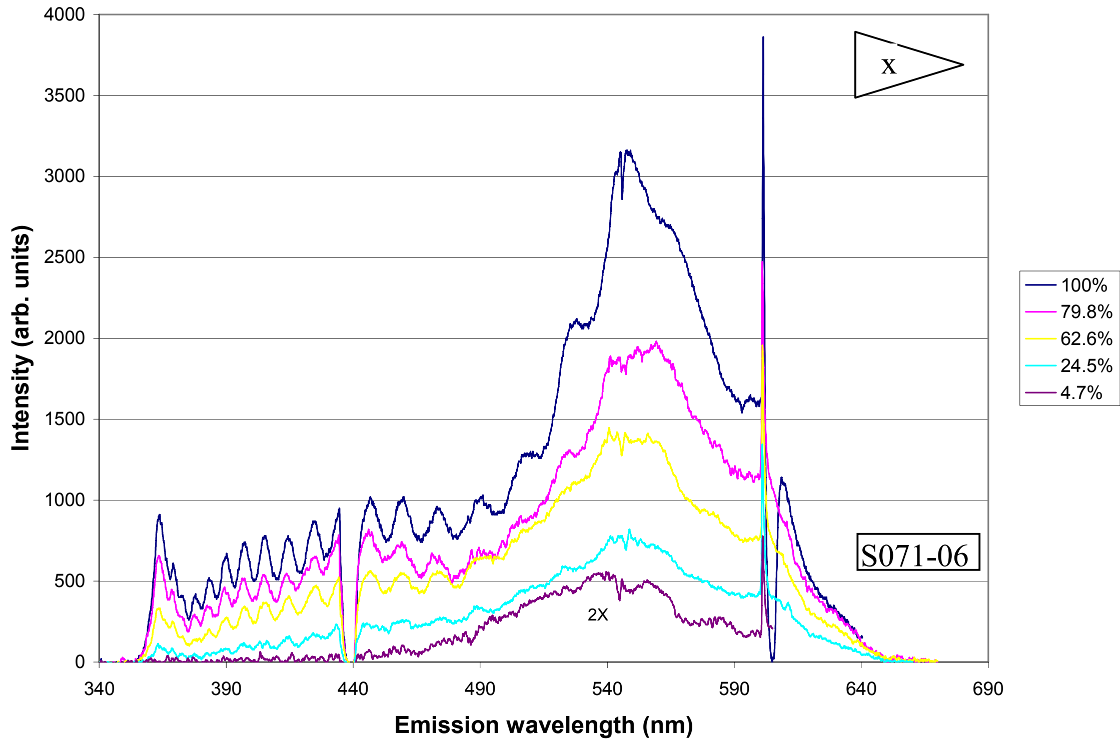


Figure 6.14 PL spectra of yellow-emitting device structure

The legend in the Figure 6.14 denotes what percentage of the beam power was passed though the ND filter and thus allowed to excite the sample.

There are two particularly interesting observations to make from the spectra in Figure 6.14:

(a) The emission peak is shorter (~550nm) than it was in the EL measurements (573nm).

(b) There is no redshift with decreasing laser intensity, as there was with decreasing injection current.

As mentioned previously, the redshift observed in EL measurements was attributed to either band-filling or piezoelectric field screening. This PL data seems to indicate piezoelectric field screening is the more likely candidate. One possible

explanation is as follows: if low-current redshift was due to band-filling, it would likely appear in Figure 6.14 as the laser power was filtered. On the other hand, we should not expect to see this redshift if piezoelectric field screening were the cause. This is because the PL laser, even when strongly filtered, generates much more electron-hole pairs (ehp's) in the material than are injected during EL. This large number of ehp's screens the piezoelectric field, thus reducing band-bending in the material and leading to shorter-wavelength emission.

This argument can be verified by calculating a rough estimate of the number of electron-hole pairs generated by PL as opposed to EL. For PL, the value of ehp/cm$^{-3}$ can be obtained by dividing the laser power density by the laser photon energy and multiplying by carrier lifetime. The specifications of the PL laser used in this study (see Section 3.5.4) are a power of 35 mW and an emission wavelength of 325nm. Assuming a laser interaction volume of 982 μm$^3$ (50 μm spot size and 0.5 μm penetration depth) and a carrier lifetime of 0.1 μsec, a series of ehp concentration values can be calculated. These values are plotted vs. ND filter transmission values in Figure 6.15.

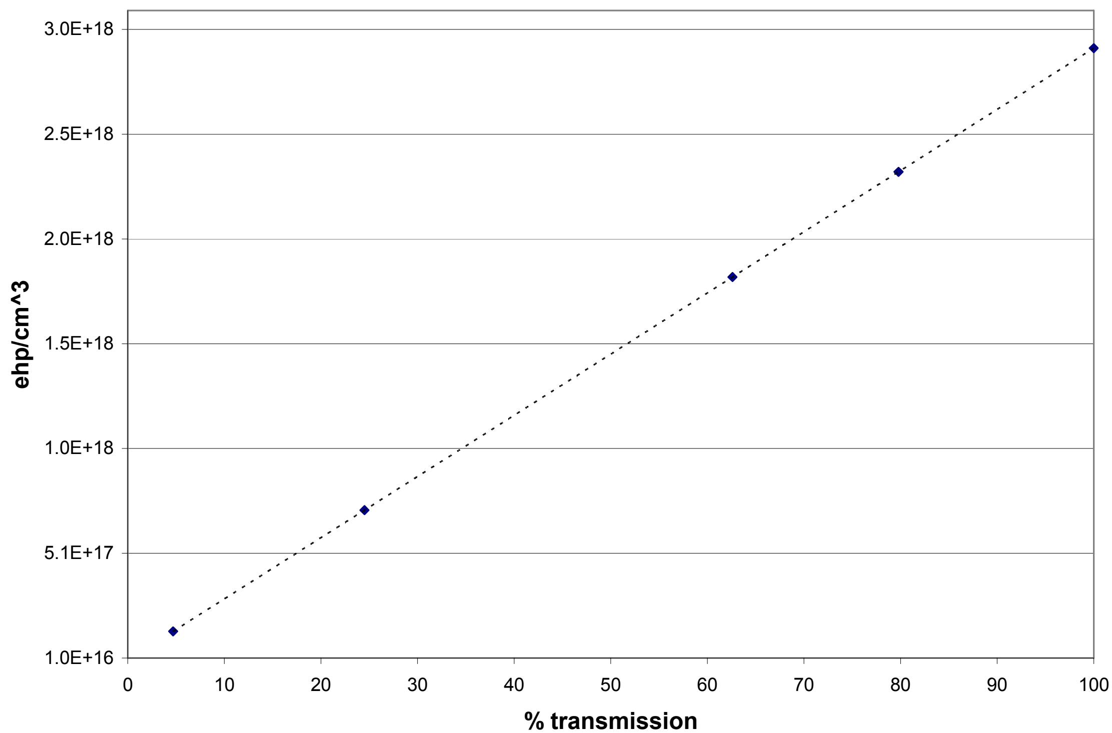


Figure 6.15 Calculated values of electron-hole pair concentration for a series of ND-filtered laser beams

The range of electron-hole pair concentrations estimated using this technique is ~$1.0 \times 10^{16}$ cm$^{-3}$ to $3 \times 10^{18}$ cm$^{-3}$ for 4.6% to 100% transmission.

A similar estimation can be made for electrical excitation. In this scenario, the ehp/cm$^{-3}$ value is obtained by multiplying the injection current by the electronic charge (to get electrons per second), dividing by device area, then multiplying by carrier lifetime. Device volume was assumed to be 16000 μm$^3$ (400 μm x 400 μm x 0.1 μm) and carrier lifetime was assumed to be 0.1 μsec.

Figure 6.16 gives the results of these calculations vs. injection current.

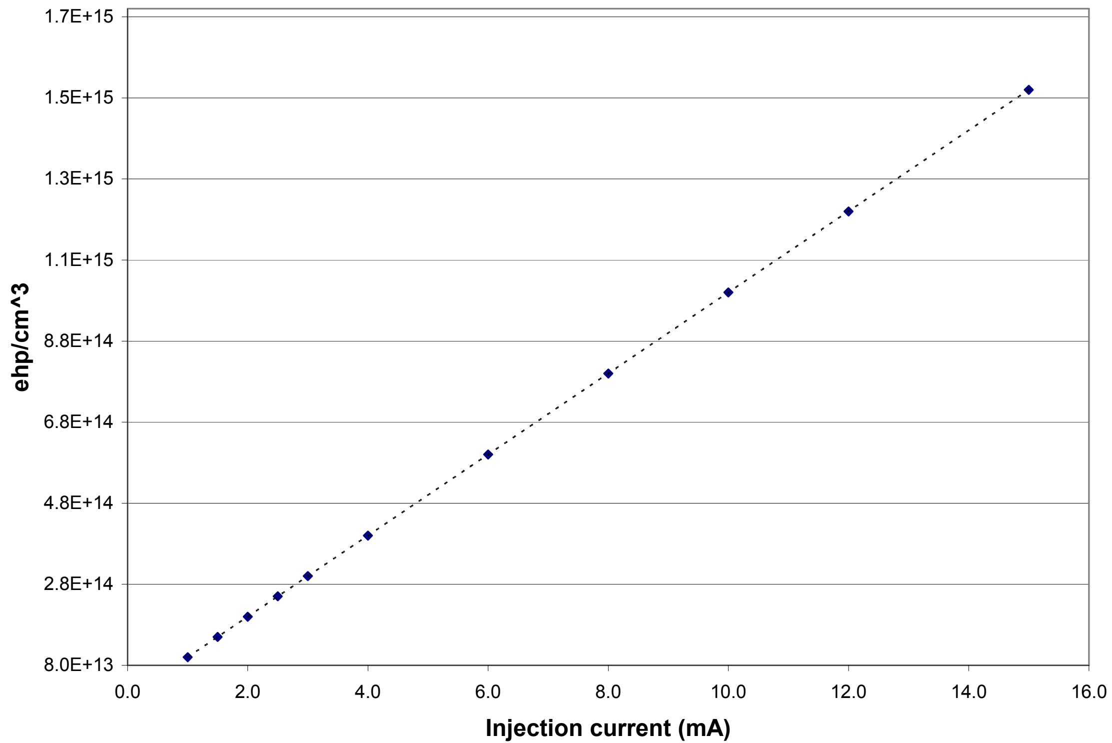


Figure 6.16 Calculated values of electron-hole pair concentration for a series of injection currents

These rough calculations show a much lower ehp concentration (~$10^{14}$-$10^{15}$ $cm^{-3}$) that was seen in Figure 6.15. The above estimated values strengthen the aforementioned argument that PL generates more ehp's than EL, and thus PL measurements will exhibit much more piezoelectric screening than EL measurements, even under relatively low excitation conditions (i.e., a very restrictive ND filter).

### *6.2.7 Electrical properties of green and yellow devices*

The IV characteristics of the green and yellow devices were measured and are given in Figure 6.17. Ideality factor was calculated as per the discussion in Section 6.3.1, and the resultant plot is presented in Figure 6.18. Shunt resistances were measured from 0-1 V, and series resistances were measured from 5-6 V (p-n junction) or 7-8 V (green

and yellow devices). All measured electrical values for the LED's, as well those for the p-n junction of Section 6.3.1, are given in Table 6.4.

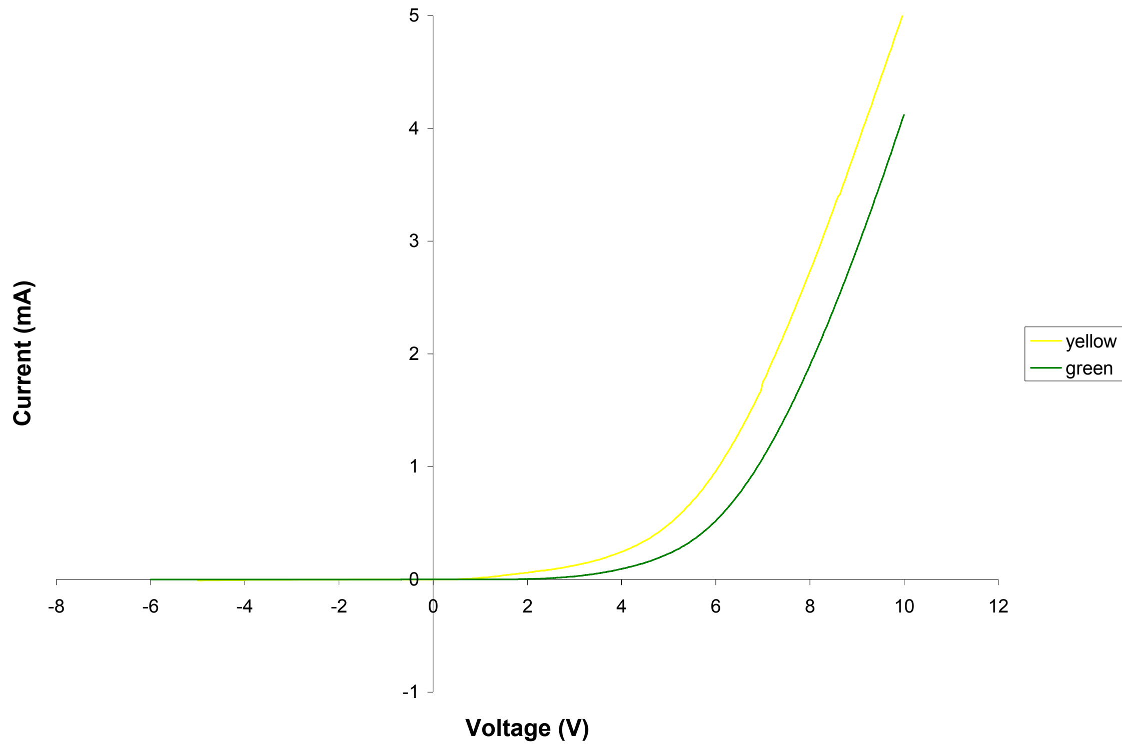


Figure 6.17 I-V Characteristics of yellow and green devices

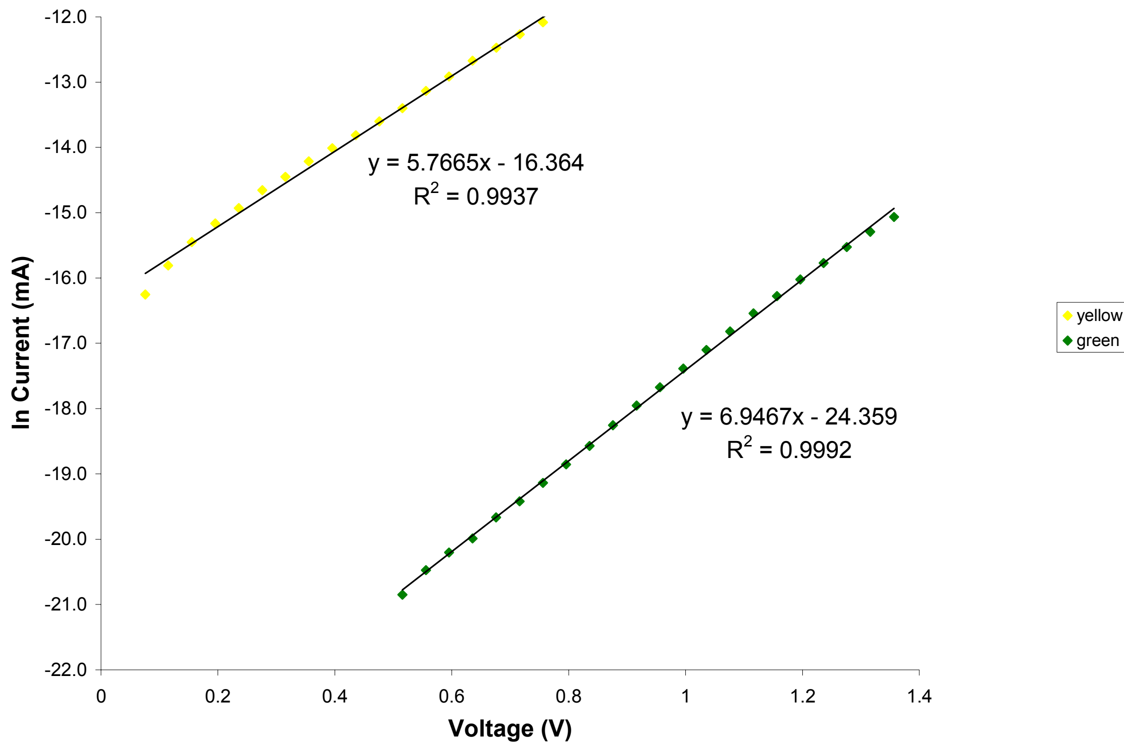


Figure 6.18 Ideality factor plots for yellow and green devices

Table 6.4 Electrical properties of fabricated devices

| Run number | Device | Leakage @ -5V (A) | Series resistance (Ω) | Shunt resistance (Ω) | Ideality factor |
|---|---|---|---|---|---|
| S052-06 | p-n junction | $-4.1\times10^{-9}$ | $1.0\times10^{2}$ | $1.9\times10^{9}$ | 6.16 |
| S069-06 tip | green | $-1.2\times10^{-8}$ | $1.2\times10^{3}$ | $3.6\times10^{7}$ | 5.53 |
| S069-06 center | yellow/amber | $-1.1\times10^{-5}$ | $1.8\times10^{3}$ | $7.5\times10^{4}$ | 6.67 |

Table 6.4 shows that the electrical characteristics of the green and yellow devices are less favorable than that of the p-n junction. The leakage values (shunt resistance and leakage current) indicate the presence of parallel conduction paths, particularly for the yellow device. All three samples exhibit a higher series resistance than typically seen in

GaN LED’s; the green and yellow devices particularly so.

The most likely explanation for the overall high series resistance is insufficient n-type doping. The homemade silane dilution manifold in the present MOCVD system has some reliability issues, and thus carrier concentration in n-type layers has been known to drift. Hall measurements made to control samples after-the-fact revealed n-type carrier concentrations of $5x10^{17}$ $cm^{-3}$ and $3x10^{17}$ $cm^{-3}$ for the p-n junction wafer and the green/yellow device wafer, respectively. This is much lower than the mid-to-high $10^{18}$ $cm^{-3}$ n-type carrier concentrations normally used in GaN-based LED’s.

There are several other possible reasons for the reduced electrical quality of the green and yellow LED’s as compared to the p-n junction. For example, the LED’s contain a thick (660Å) undoped active region as well as 200 Å undoped low-temperature cap. These regions will likely increase the series resistance of the diode. Also, because these regions were grown at low temperatures, and their material quality may be somewhat poor. Indeed, background carrier concentrations $\sim 10^{17} cm^{-3}$ were measured in bulk InGaN films. This may lead to leakage paths which would increase leakage current and lower shunt resistance.

Another factor to bear in mind is the surface upon which the p-type layer was grown. In the case of the p-n junction, the p-type material was deposited upon optimized n-type GaN with a surface roughness of <4Å RMS (see Section 3.6.1). In the LED’s, on the other hand, the p-type layer was grown on a low-temperature (LT) cap of unknown quality and roughness. Also, because of the long ramp times necessary to heat up to p-type growth temperature, some etching of the LT cap may have occurred. Such etching would not be uniform. Thus, the p-type material in the yellow and green LED’s was

grown on a non-optimized layer which also may have been partially etched. This means, perhaps, that the p-type layer of the LED wafer is of poorer quality than that of the p-n junction, which may explain its somewhat poorer electrical characteristics.

### 6.4 Demonstration of White Emission

With the successful demonstration of yellow LED's given in Section 6.3.4, the attention can now be focused on mixing yellow with blue to generate white emission, as discussed in Section 6.1.2.

A series of three runs was carried out on wedge-shaped substrates in order to establish a preliminary exploration of white LED's. Each of these runs was structured as follows: a standard n-type layer (n~$5x10^{17}$ $cm^{-3}$), an InGaN/GaN MQW structure grown at $T_{well}$ /$T_{barrier}$ = 770°C/770°C (for blue emission), an InGaN/GaN MQW structure grown at $T_{well}$ /$T_{barrier}$ = 725°C/760°C (for yellow emission), and standard p-type capping layers grown at 850°C and 950°C. The only difference between the three runs was the number of wells in each MQW structure: either two blue and two yellow QW's (2x2), three blue and three yellow QW's (3x3), or four blue and four yellow QW's (4x4) were used.

Photoluminescence measurements for each structure resulted in emission which looked white to the eye in the center and base. Emission at the tip looked blue, however; and spectra showed only one peak. PL spectra from the center of each wafer are given in Figures 6.19 – 6.21.

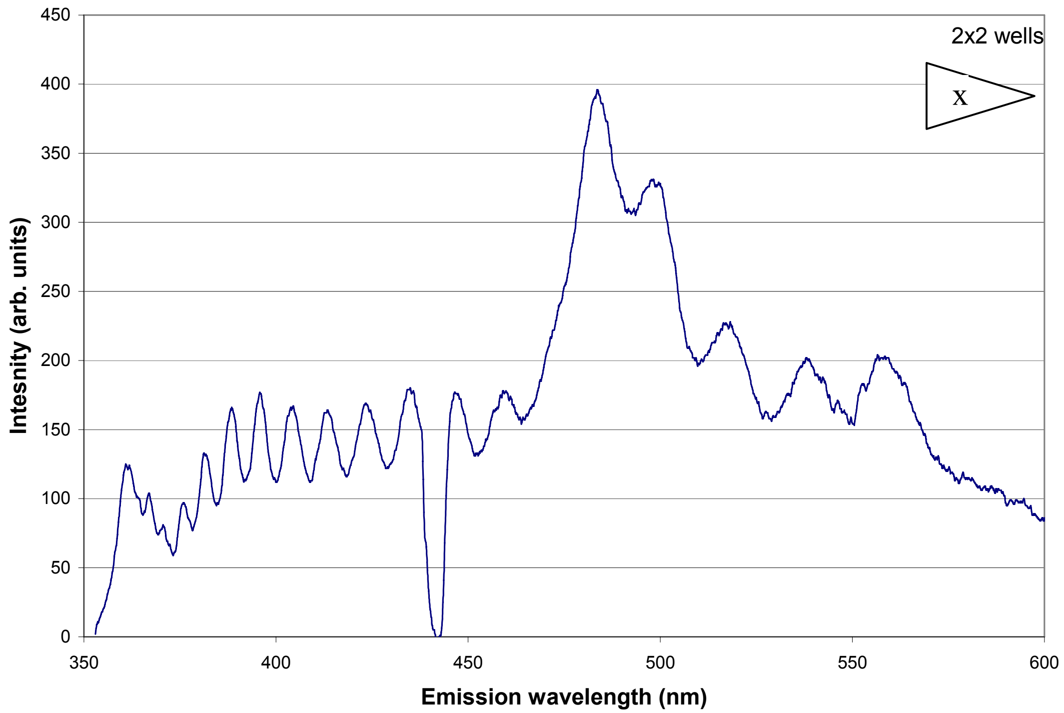


Figure 6.19  PL emission spectra of white-emitting devices composed of  2x2 QW's

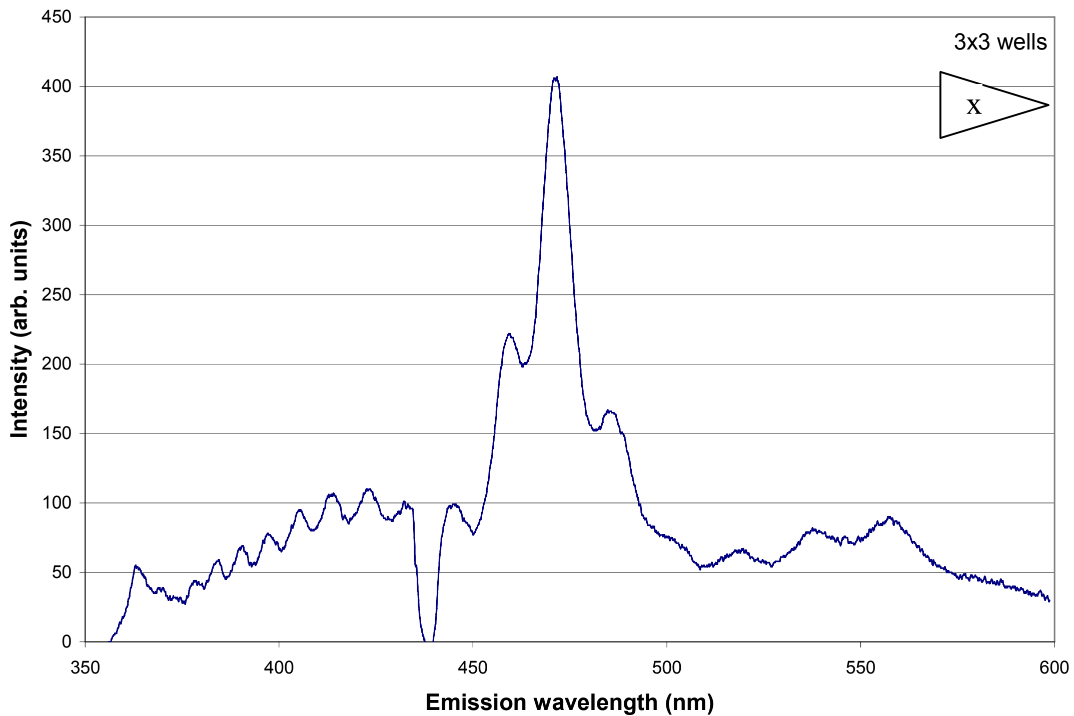


Figure 6.20  PL emission spectra of white-emitting devices composed of 3x3 QW's

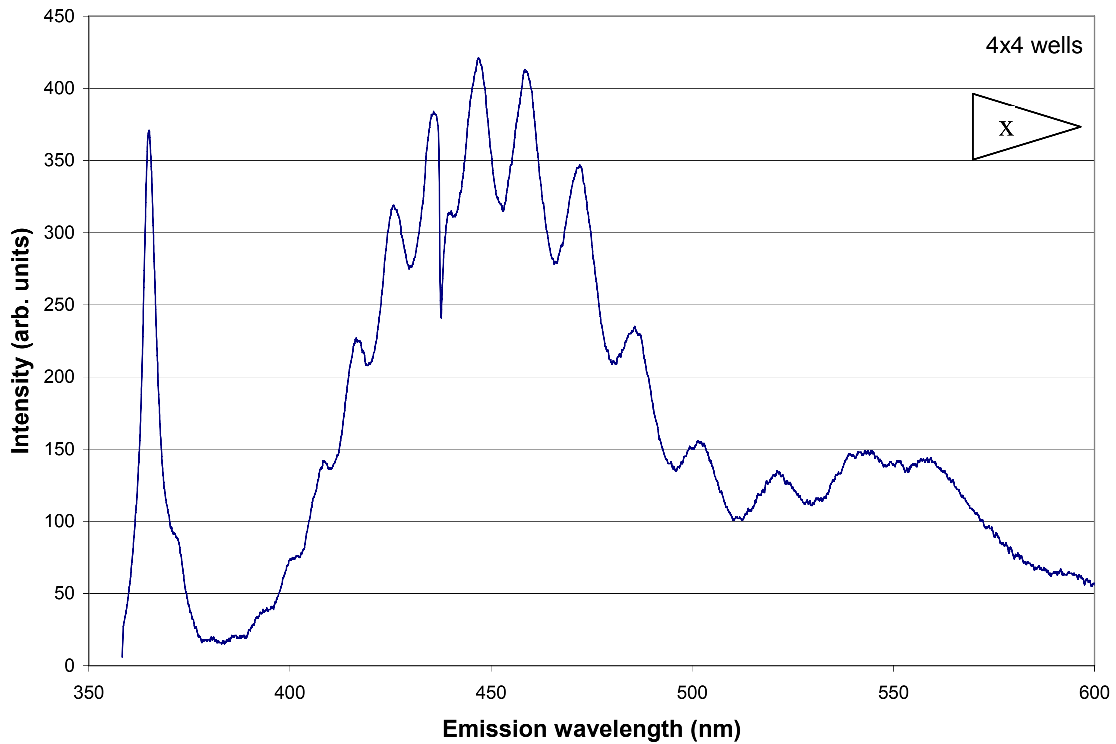


Figure 6.21 PL emission spectra of white-emitting devices composed of 4x4 QW's

In each case, emission from both a blue structure and a yellow structure is measured. The yellow peak, despite being closer to the surface (and therefore closer to the laser) is much weaker than the blue peak. This is to be expected because of the reduced electron and hole wavefunction overlap in the more strained higher-wavelength structure (see Section 5.5).

The results from these measurements are given in Table 6.5.

Table 6.5 PL results from white-emitting structures

| Run number | # blue wells x # yellow wells | Blue peak wavelength (nm) | Yellow peak wavelength (nm) | PL intensity ratio ($I_{yellow}/I_{blue}$) |
|---|---|---|---|---|
| S080-06 | 4x4 | 445 | 557 | 0.337 |
| S081-06 | 3x3 | 472 | 558 | 0.218 |
| S082-06 | 2x2 | 482 | 557 | 0.511 |

One particularly interesting trend in these data is the redshift of the blue peak that accompanies the decrease in the number of quantum wells. It is a somewhat odd phenomenon, because there is not a corresponding shift in the yellow emission peaks.

This observation can likely be explained with a strain argument. As the number of wells is increased from 2x2 to 4x4, the overall strain in the structure likely decreases due to relaxation. With this decrease in strain comes a subsequent decrease in piezoelectric band-bending, which leads to the observed blue shift in the blue quantum wells. The lack of corresponding shift in the yellow quantum wells is perhaps due to the fact that these wells contain a much higher indium content, and thus are likely to be relaxed even in the 2x2 case.

In addition to the emission wavelength values, Table 6.5 includes the peak intensity ratios measured from the PL spectra. Such information is important in optimizing the white emission obtained from complementary colors (see Table 6.2). However, using PL to obtain these values can be a bit misleading. Because the yellow QW's were nearer to the surface of the overall structure, they were excited by laser emission that was much less attenuated than the lower blue wells. Thus, the "real"

intensity ratios (i.e., that of operational devices) would be lower than the values listed in Table 6.5.

Figure 6.22 shows a chromaticity diagram which includes wavelength-to-wavelength tie lines corresponding to the emission peaks seen in this section's samples.

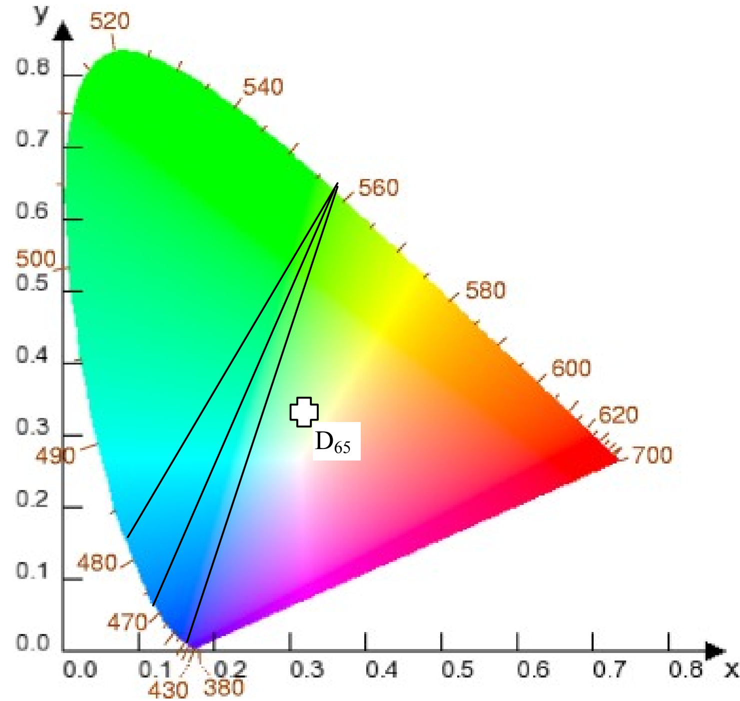


Figure 6.22 Chromaticity diagram showing the complementary white structures grown with the TSS-CCS

Of the three structures, the 4x4 sample yielded emission closest to Illuminant $D_{65}$. In the two 2x2 and 3x3 cases, in which blue MQW emission was indeed measured, the blue wavelength was to long (or the yellow too short) to achieve the chromaticity points at Illuminant $D_{65}$. However, in all four cases, emission which was white to the eye was clearly observed. Thus, this research project has concluded that using an InGaN/GaN-based dual-wavelength structure is a feasible approach to obtain white light. Achieving

the exact coordinates at Illuminant $D_{65}$ is merely a case of fine-tuning the individual blue and yellow peaks.

These three structures were fabricated into devices and white electroluminescence was achieved from the 3x3 and 2x2 structures. Details of this work explored further by the next generation of students in the laboratory.

6.5 **References**


1. S. Nakamura, T. Mukai, and M. Senoh. "Candela-class high-brightness InGaN/AlGaN double heterostructure blue-light-emitting diodes." *Appl. Phys. Lett.* **64**, 1687 (1994).

2. S. Nakamura. "Blue-green light-emitting diodes and violet laser diodes." *MRS Bull.* p. 29, February (1997).

3. D. Steigerwald, S. Rudaz, H. Liu, R.S. Kern, W. Götz, and R. Fletcher. "III-V nitride nemiconductors for high-performance blue and green light-lmitting devices." *J. of Mat.* **49**, 18 (1997).

4. S.J. Chang, W.C. Lai, Y.K. Su, J.F. Chen, C.H. Liu, and U.H. Liaw. "InGaN—GaN multiquantum-well blue and green light-emitting diodes." *IEEE J. on Sel. Top. in Quant. Elec.* **8**, 278 (2002).

5. Y.D. Qi, H. Liang, D. Wang, Z.D. Lu, W. Tang, and K.M. Lau. "Comparison of blue and green InGaN/GaN multiple-quantum-well light-emitting diodes grown by metalorganic vapor phase epitaxy." *Appl. Phys. Lett.* **86**, 101903.

6. E.F. Schubert. *Light-Emitting Diodes,* Chapter 11.2. Cambridge University Press, Cambridge (2003).

7. Wikipedia: The Free Encyclopedia. Found online at http://en.wikipedia.org

8. G. Wyszecki and W.S. Stiles. Color Science: Concepts and Methods, Quantitative Data and Formulae. 2$^{nd}$ edidtion. John Wiley and Suns, New York (1982).

9. S. Muthu. "Red, green, and blue LEDs for white light illumination." *IEEE J. on Sel. Top. in Quant. Elec.* **8**, 333 (2002).

10. B. Damilano, N. Grandjean, C. Pernot, J. Massies. "Monolithic white light emitting diodes based on InGaN/GaN multiple-quantum wells." *Jpn. J. Appl. Phys.* **40**, L918 (2001).

11. Y.-L. Li, Th. Gessman, E.F. Schubert, and J.K Sheu. "Carrier dynamics in nitride-based light-emitting p-n junction diodes with two active regions emitting at different wavelengths." *J. of Appl. Phys.* **94**, 2167 (2003).

12. T. Mukai, M. Yamada, and S. Nakamura. "Characteristics of InGaN-based UV/blue/green/amber/red light-emitting diodes." *Jpn. J. Appl. Phys.* **38**, 3976 (1999).

13. M. Yamada, Y. Narukawa, and T. Mukai. “Phosphor free high-luminous-efficiency white light-emitting diodes composed of InGaN multi-quantum well.” *Jpn. J. Appl. Phys.* **41**, L246 (2002).

14. J.S. Foresi and T.D. Moustakas. “Metal contacts to gallium nitride.” *Appl. Phys. Lett.* **62**, 2859 (1993).

15. C. Sah, R.N. Noyce, and W. Shockley. “Carrier generation and recombination in p-n junctions and p-n junction characteristics.” *Proc. IRE* **45,** 1228 (1957).

16. X.A. Cao, E.B. Stokes, P.M. Sandvik, S.F. LeBoeuf, J. Kretchmer, and D. Walker. “Diffusion and tunneling currents in GaN/InGaN multiple quantum well light-emitting diodes.” *IEEE Elec. Dev. Lett.* **23**, 535 (2002).

17. J.G. Pagan, E.B. Stokes, K. Patel, C.C. Burkhart, M.T. Ahrens, P. Barletta, and M. O’Steen. "Colloidal quantum dot active layers for light emitting diodes." *Solid-State Elec.* **50**, 1461 (2006).

18. J.M. Shah, Y.-L. Li, Th. Gessmann, and E.F. Schubert. “Experimental analysis and theoretical model for anomalously high ideality factors (n>>2) in AlGaN/GaN p-n junction diodes.” *J. Appl. Phys.* **94**, 2627 (2003).

# 7.0 Suggestions for Future Work

When thinking about the future research, I see each of my ideas falling into one of two categories: short term projects that can be accomplished in our lab; or longer-term efforts that the scientific community as whole can undertake in an effort to advance the study of GaN in general and GaN-based lighting in particular.

In our lab, the project is in a very promising state. Now that the basic parameters of the system are established, we are primed to start carrying some very exciting work. Obviously, one of our main goals will be emission wavelengths in the far yellow, amber, and perhaps red. The question, of course, is how? The research reported in this dissertation may provide some insight. For example, there was an observation that MQW structures that contain GaN barriers grown at temperatures less than 725˚C exhibit poor emission characteristics. This seems to indicate that the crystal quality of the barrier is critical in achieving good emission. Perhaps taking other steps to improve barrier quality, such as introducing hydrogen during barrier growth, may pay dividends in the form of brighter, longer-wavelength emission.

Also, the device aspect of this project is ready to take off. There are perhaps some p-type issues that need to be resolved (as reported in Chapter 6), but that is likely a minor obstacle toward growing and fabricating monochromatic LED's over a wide spectrum of the visible range. Next, the focus should turn to the two-color device depicted in Figure 6.4. One of the major challenges that I foresee with that particular structure is MQW growth on top of a p-type layer, the surfaces of which are usually rough. Some type of thin smoothing layer may be needed.

On a larger scale, I would be interested to see some more research into cubic GaN. C-GaN was discussed briefly in Chapter 3, where some of its more desirable properties (better mobility, improved p-type doping) were mentioned. Its potential as a long-wavelength emitter is quite low due to its lack of piezoelectricity, but I would still be curious to see perhaps some violet to blue devices fabricated from this material. Is it possible that c-GaN research may yield some clues as to the improvement of h-GaN? Also, how is spinodal composition different in c-GaN, if at all? Can higher concentrations of In be incorporated into its cubic phase? Such research could help us gain a better overall understanding of the GaN material system.

Lastly, further studies into novel substrates could revolutionize this field. For example, Cermet, Inc. has recently reported the growth of InGaN on ZnO. At first, this seems like an odd choice – ZnO is not a particularly good lattice match for GaN. However, it turns out that ZnO is actually a near perfect match for InGaN with 16% InN content. Granted, there are still some issues with this technology – ZnO reacts readily with $NH_3$ – but this is exactly the time of innovative research can bring GaN-based solid-state lighting technology to the next level.

I've certainly enjoyed working on this project, and the experience I've gained has been invaluable. As I continue on my career, I will always keep an eye on the newest advances in GaN-based solid-state lighting – and be proud that I was once part of that drive.